

# Neural Equilibria for Long-Term Prediction of Nonlinear Conservation Laws

Jose Antonio Lara Benitez<sup>\*1</sup>, Kareem Hegazy<sup>2</sup>, Junyi Guo<sup>2</sup>, Ivan Dokmanić<sup>3</sup>, Michael W. Mahoney<sup>4</sup>, and Maarten V. de Hoop<sup>1</sup>

<sup>1</sup>Rice University

<sup>2</sup>ICSI and University of California at Berkeley

<sup>3</sup>University of Basel

<sup>4</sup>ICSI, LBNL, and University of California at Berkeley

## Abstract

We introduce *Neural Discrete Equilibrium* (NeurDE), a machine learning framework for stable and accurate long-term forecasting of nonlinear conservation laws. NeurDE leverages a kinetic lifting that decomposes the dynamics into a fixed linear transport component and a local nonlinear relaxation to equilibrium. This structure provides a natural and principled interface between physics, numerical methods, and machine learning methodologies, enabling NeurDE to be viewed as a “neural twin” to Boltzmann-BGK. The transport step can be implemented efficiently in solvers such as lattice Boltzmann (LB), while the equilibrium is modeled by a neural network that maps macroscopic observables to a discrete equilibrium distribution. When integrated into a LB solver, the transport step becomes an efficient lattice streaming operation, and NeurDE yields a hybrid algorithm that robustly captures shock propagation and complex compressible dynamics over long time horizons. The NeurDE method is highly data-efficient: a small network trained on limited data generalizes far beyond the training regime, resolving shocks that evolve well outside the initial training distribution. Unlike traditional kinetic solvers, NeurDE achieves this accuracy without costly root-finding procedures or large velocity lattices. These results establish NeurDE as a scalable, efficient, and physics-informed paradigm for learning-based simulation of nonlinear conservation laws.

## 1 Introduction

Nonlinear conservation laws are central to mathematical physics, governing the transport of conserved quantities such as mass, momentum, energy, charge, and vorticity. They arise across diverse systems, including fluid and plasma dynamics, astrophysics, and geophysical flows. Canonical examples include the Euler, magnetohydrodynamics, and shallow-water equations. Although these systems admit a compact formulation, their solutions can exhibit intricate structure: nonlinear fluxes generically produce steep gradients and shocks in finite time, even from smooth initial data. These singular features coexist with smooth phenomena such as rarefactions, contacts, and vortex layers, producing multiscale dynamics that are both mathematically subtle and computationally demanding.

The accurate numerical approximation of such equations remains a long-standing challenge in physically relevant regimes. High-order methods must carefully balance accuracy and stability, while shock capturing typically requires nonlinear flux evaluations or Riemann solvers [50, 79]. These difficulties intensify in under-resolved and high-dimensional regimes, where nonlinear structures interact across scales.

Machine learning (ML)—more recently, scientific machine learning (SciML) [6, 55, 42, 30, 34, 10, 82, 17, 33]—has emerged as a promising tool to accelerate or augment numerical solvers. However, existing approaches face fundamental limitations. Physics-informed neural networks (PINNs) [12] enforce the governing partial

---

<sup>\*</sup>Corresponding author: [antonio.lara@rice.edu](mailto:antonio.lara@rice.edu)

differential equation (PDE) only weakly, through “soft” penalty terms, which are notoriously difficult to optimize [44]. Deep operator-learning models [41, 55], including Fourier Neural Operators (FNOs) [52], treat the PDE as a black box by learning the solution operator directly. Such methods lack intrinsic physical structure, often leading to weak conservation, instability, and poor long-term accuracy, particularly in shock-dominated and other challenging regimes [58, 70]. Moreover, these and other data-driven methods [34, 33] require large datasets from costly simulations.

In response to these limitations, we introduce the *Neural Discrete Equilibrium* (NeurDE) framework, a model grounded in fundamental physics that combines the stability and accuracy of numerical solvers with the flexibility and speed of modern ML architectures. Most SciML methods are highly data-driven: they offer flexibility and are fast, but they tend to be fragile, inaccurate, data-hungry, and prone to poor generalization. Conversely, traditional physics-based numerical solvers are data-efficient, accurate, and robust, but they are often too rigid to adapt across problem classes. NeurDE strikes a balance between these extremes by embedding one of the most universal physical principles—*conservation*—directly into the model architecture. This inductive bias yields a framework that is both data-efficient and physically faithful, while retaining the adaptability of modern ML.

Nonlinear conservation laws can be generally represented by a PDE known as the continuity equation:

$$\partial_t \mathbf{U}(t, \mathbf{x}) + \nabla_{\mathbf{x}} \cdot \mathbf{F}(\mathbf{U}(t, \mathbf{x})) = 0, \quad (1)$$

where  $\mathbf{x}$  is the spatial variable,  $t$  the time variable,  $\mathbf{U}$  are the conserved fields, and  $\mathbf{F}(\mathbf{U})$  the flux function. For example, in the compressible Euler equations,  $\mathbf{U} = (\rho, \rho\mathbf{u}, E)^\top$  represents density, momentum, and energy, and the flux function is  $\mathbf{F}(\mathbf{U}) = (\rho\mathbf{u}, \rho\mathbf{u}\mathbf{u}^\top + p\mathbf{I}, (E + p)\mathbf{u})^\top$ , with  $p = \rho RT$  where  $R$  is the gas constant and  $T$  is determined by an equation of state [57].

Directly working with Eq. (1) remains challenging due to its nonlinear, coupled structure. A conceptually elegant alternative to solving it directly is to *perform a lifting of the macroscopic conservation law* into a kinetic representation, and then *solve in the lifted representation*. Instead of tracking the nonlinear dynamics of  $\mathbf{U}$  directly, we employ the Boltzmann–BGK formulation [7], which evolves a single-particle distribution function  $f(t, \mathbf{x}, \mathbf{v})$ , where  $\mathbf{x}$  and  $\mathbf{v}$  are the (independent) microscopic (particle) position and velocity, respectively. Bouchut’s seminal work guarantees that any hyperbolic conservation law with convex entropy admits such a BGK surrogate [8], ensuring that *NeurDE’s lifting is universal*, rather than ad hoc.

This kinetic formulation provides a natural and principled interface between physics, numerical methods, and ML methodologies; effectively making NeurDE a “neural twin” of Boltzmann–BGK. Our neural twin formalism (Eq. (2) below) naturally separates the linear but non-local transport operator on the left-hand side from the local but nonlinear relaxation on the right. The resulting structural separation naturally lends itself to operator splitting schemes that transform the previously complicated conservation law Eq. (1) into a simple particle-based framework of streaming and collision [28, 35]. To further improve the computational efficiency and accuracy of NeurDE, we evaluate these operators on a lattice to leverage the accuracy and efficiency of previous lattice Boltzmann (LB) approaches. During collisions, the particle distribution relaxes toward the local equilibrium  $f^{\text{eq}}$ , which fully determines the macroscopic physics [19] if, and only if, the non-equilibrium contributions recover the correct transport coefficients [47, 72]. The streaming step, corresponding to linear advection, can be solved exactly on a lattice through trivial shifts between lattice points, eliminating numerical diffusion and cumulative transport errors—a principle underlying the LB method [46, 77]. Crucially, the governing PDE need *not* be specified *a priori*: the method operates at the mesoscopic level and the learned relaxation is a nonlinear local operator. The result is a transparent, physically interpretable neural architecture with conservation and thermodynamic structure built in by design.

NeurDE, as a neural twin to LB, provides a neural surrogate for the local equilibrium mapping used in the collision step. In this context, spatial variables are handled through the lattice, while temporal evolution proceeds step-by-step, simplifying the learning task compared with standard SciML approaches that often treat space and time identically [34]. Unlike PINNs and other related methods, which impose physical constraints in the loss function in a “soft” manner and which have well-known failure modes [44], NeurDE builds the physical constraints and dynamic framework into the model. Unlike neural operators, which try to learn the entire solution operator but which also come with challenges [58, 70, 43], NeurDE is learning an isolated task and relies on the Boltzmann framework to produce much of the physical dynamics. Moreover, by design, NeurDE naturally couples physical phenomena between length scales: NeurDE evolves dynamics

on the mesoscopic scale and predicts macroscopic observables. While we focus here on LB, this surrogate approach could, in principle, be adapted to other numerical schemes.

Recent neural BGK approaches fall broadly into two categories. Some embed neural correctors into a known BGK operator [85, 61], while others replace the collision operator entirely [86, 18]. These methods often struggle to maintain entropy dissipation, conservation, or positivity under discrete velocity discretizations [25]. In contrast, we learn the discrete equilibrium itself, guaranteeing that conservation and entropy structure are enforced intrinsically.

The NeurDE model exhibits strong extrapolative capabilities, accurately predicting shock propagation in transonic and supersonic regimes over hundreds of time steps and for initial conditions far beyond the training distribution. For example, a model trained on only 500 steps of a transonic Sod problem [74] faithfully reproduces nonlinear shock interactions at time steps beyond 2000, as shown in Fig. 5(f – i).

To summarize, this work introduces NeurDE, a universal, physically constrained SciML framework for nonlinear conservation laws. Our main contributions are the following.

- A physics-embedded architecture that parameterizes the equilibrium manifold directly, guaranteeing conservation and entropy consistency by construction.
- A hybrid lattice–neural algorithm in which transport is handled analytically and only the equilibrium closure is learned.
- A PDE-free formulation in which the governing equations do not need to be specified explicitly.
- Stable extrapolation properties, maintaining accuracy far beyond the training regime, by incorporating numerical methods into the architecture.

## 2 Results

### 2.1 Lattice Boltzmann Framework

The NeurDE framework is based on the single-particle distribution  $f$ , whose dynamics is governed by the Boltzmann–BGK<sup>1</sup> equation [7]; notation is presented in Sec. A, and further details are provided in Subsecs. B.1 to B.4:

$$(\partial_t + \mathbf{v} \cdot \nabla) f(t, \mathbf{x}, \mathbf{v}) = \frac{1}{\tau} (f^{\text{eq}}(\mathbf{U}(t, \mathbf{x}))(\mathbf{v}) - f(t, \mathbf{x}, \mathbf{v})), \quad (2)$$

where  $\mathbf{v} \in \mathbb{R}^d$  denotes the mesoscopic particle velocity (distinct from the macroscopic velocity  $\mathbf{u}$ ), and  $\mathbf{U}$  denotes the macroscopic observable. Fig. 1a illustrates this *lift* from macroscopic Eq. (1) to the kinetic formulation (Eq. (2)). The collision operator (right-hand side of Eq. (2)) encodes nonlinear interactions and is commonly approximated by relaxation toward a local equilibrium  $f^{\text{eq}}$  over a characteristic time  $\tau$  (Eq. (2)). The  $f^{\text{eq}}$  distribution encodes all the nonlinear physics: for gas dynamics, it is the Maxwell–Boltzmann distribution, characterized variationally as the minimizer of the kinetic entropy [51]. Details are provided in Subsec. B.2.

Macroscopic *conserved quantities*—density ( $\rho$ ), momentum ( $\rho\mathbf{u}$ ), and energy ( $E$ )—are obtained as velocity moments,

$$\langle (1, \mathbf{v}, \frac{1}{2}\mathbf{v} \cdot \mathbf{v})^\top f \rangle = (\rho, \rho\mathbf{u}, \rho E)^\top, \quad (3)$$

where  $\langle \cdot \rangle_\mu$  denotes integration over the velocity measure  $d\mu(\mathbf{v})$ . We omit the subscript when  $d\mu(\mathbf{v}) = d\mathbf{v}$  is the Lebesgue measure.

Evaluating macroscopic observables requires integrating  $f$  over the unbounded continuous velocity space, which is intractable to calculate numerically and must therefore be discretized [73]. Replacing  $d\mathbf{v}$  with a discrete measure  $d\mu$  supported on a finite set of particle velocities  $\{\mathbf{c}_i\}_{i=1}^Q$  (Subsec. B.4) yields the coupled system,

$$(\partial_t + \mathbf{c}_i \cdot \nabla) \mathbf{f}_i(t, \mathbf{x}) = \frac{1}{\tau} (\mathbf{f}_i^{\text{eq}}(\mathbf{U}(t, \mathbf{x})) - \mathbf{f}_i(t, \mathbf{x})) \quad i = 1, \dots, Q, \quad (4)$$

where  $\mathbf{f}_i \equiv f(t, \mathbf{x}, \mathbf{c}_i)$  are the discrete populations,  $\mathbf{f}_i^{\text{eq}}$  their equilibrium, and  $\mathbf{U}$  are macroscopic fields obtained as moments over  $d\mu$ .

---

<sup>1</sup>Bhatnagar–Gross–Krook

**Universal Kinetic Framework**  
adapts to any conservation law

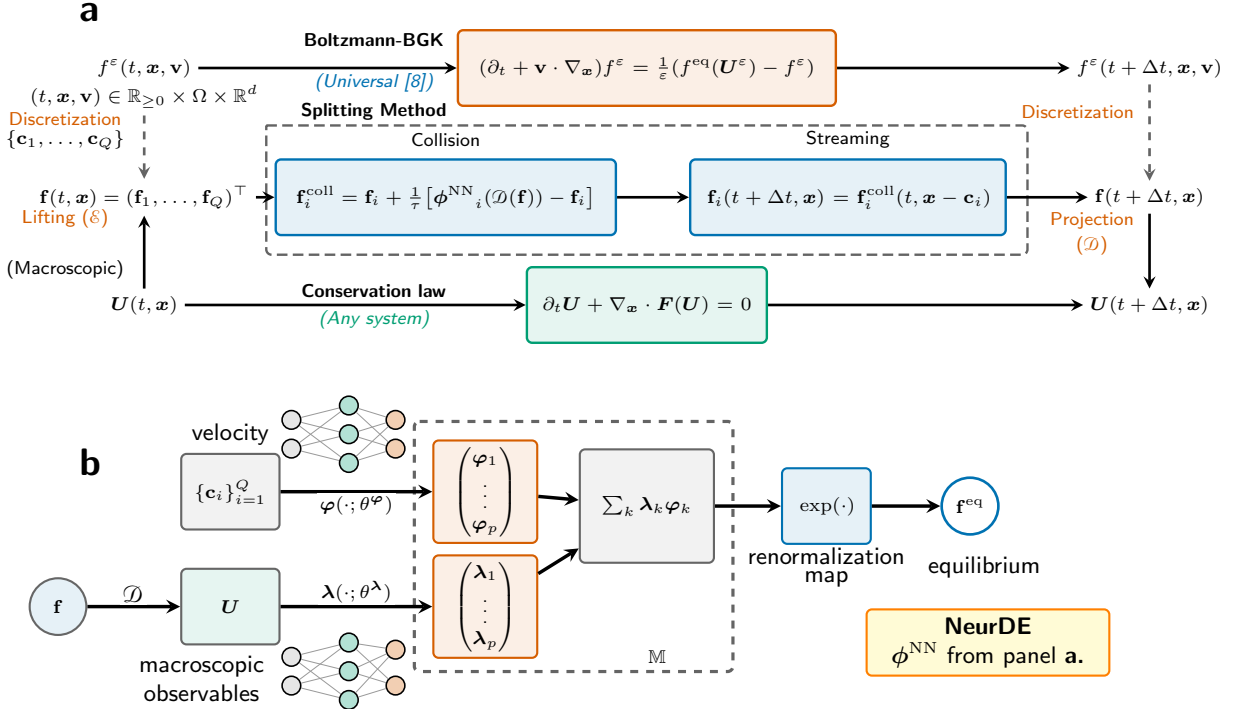


**Figure 1: Universal kinetic framework for conservation laws.** **a.** The LB+NeurDE lifts *any* system of nonlinear conservation laws into a universal kinetic framework. The Boltzmann-BGK equation [8] provides a universal kinetic representation valid for arbitrary conservation laws, making this approach a foundation model that adapts to different physical systems without architectural changes. The green region depicts macroscopic observables  $\mathbf{U}$  evolving from  $t$  to  $t + \Delta t$ . The pink region shows the universal continuum kinetic description. The blue region demonstrates discretization where NeurDE infers equilibrium states and macroscopic fields are recovered via moment projection. **b.** NeurDE architecture learns the system-specific equilibrium map  $\mathbf{f}^{\text{eq}} = \phi^{\text{NN}}(\mathbf{U}; \theta)$ . The dashed rectangle represents the moment space  $\mathbb{M} = \text{span}\{\varphi(\mathbf{c}_i)\}$ . The projection  $\mathcal{D}[\mathbf{f}] = \mathbf{U}$  and lifting  $\mathcal{E}$  operators connect macroscopic and kinetic levels. The exponential map ensures thermodynamic consistency by mapping from moment space back to the distribution space.

The lattice Boltzmann (LB) method provides a discrete realization of Eq. (4) by separating the dynamics into collision, where populations  $\mathbf{f}_i$  relax toward equilibrium (Eq. (5a)), and streaming, where they propagate along lattice directions  $\{\mathbf{c}_i\}_{i=1}^Q$  (Eq. (5b)). This procedure can be interpreted as a splitting of the kinetic dynamics [21], and the resulting dimensionless LB update reads,

$$\mathbf{f}_i^{\text{coll}}(t, \mathbf{x}) = \mathbf{f}_i(t, \mathbf{x}) + \frac{1}{\tau} [\mathbf{f}_i^{\text{eq}}(\mathbf{U}(t, \mathbf{x})) - \mathbf{f}_i(t, \mathbf{x})], \quad (5a)$$

$$\mathbf{f}_i(t + 1, \mathbf{x} + \mathbf{c}_i) = \mathbf{f}_i^{\text{coll}}(t, \mathbf{x}). \quad (5b)$$

A significant benefit of the lattice in LB methods is that streaming (Eq. (5b)) reduces to shifting lattice values (or a memory pointer). This procedure is highly computationally efficient, and it is easily scaled and parallelized [49]. Crucially, streaming exactly solves the discretized linear transport, yielding zero numerical dissipation. Fig. 1a illustrates the connections between the continuity, Boltzmann, and splitting LB equations.

Our method mitigates two well-known limitations of the lattice using a combination of numerical methods and ML. First, stability deteriorates as the relaxation time approaches its lower bound ( $\tau \rightarrow 1/2$  in lattice units), corresponding to vanishing viscosity. By dynamically increasing the viscosity at these regions, we maintain stability [47]. Second, a fundamental difficulty in all discrete-velocity kinetic models arises from the

fact that the continuous Maxwellian no longer minimizes the kinetic entropy on a finite velocity set. Standard formulations of the equilibrium distribution  $\mathbf{f}^{\text{eq}}$  are inherently low-Mach: their accuracy relies on low-order Hermite expansions and lattice isotropy, leading to errors that grow rapidly with Mach number [25]. Worse, improving these expansions requires solving a nonlinear constrained optimization problem in every cell at each time step—a prohibitively expensive task for large-scale simulations [47]. These issues make high-speed and/or turbulent flows particularly demanding, especially when small velocity sets are used (Subsec. B.9). With NeurDE, we target this exact regime by introducing a neural surrogate that directly learns the mapping  $\mathbf{U} \mapsto \mathbf{f}_i^{\text{eq}}$ , providing an efficient, scalable, and accurate approximation of the discrete equilibrium for any lattice-based kinetic model.

## 2.2 NeurDE and LB+NeurDE

NeurDE leverages ML methods to create a Boltzmann-BGK neural twin while addressing limitations from Boltzmann-BGK’s reliance on prescribed equilibrium distributions, which are no longer valid after discretizing velocity (a requirement to tractably calculate macroscopic variables). NeurDE’s architecture is motivated by entropy-based closures [40, 22, 51, 60], which express the local equilibrium in an exponential-family form

$$f(\boldsymbol{\lambda}, \mathbf{c}) = \exp(\boldsymbol{\lambda} \cdot \boldsymbol{\varphi}(\mathbf{c})).$$

Here,  $\boldsymbol{\varphi}(\mathbf{c})$  are basis functions (the sufficient statistics), and the parameters  $\boldsymbol{\lambda}$  are Lagrange multipliers that enforce prescribed moment constraints. In classical methods, recovering  $\boldsymbol{\lambda}$  requires solving a computationally prohibitive nonlinear system at each grid cell in space and time [25, 47].

The NeurDE framework amortizes this cost by learning a direct map from the macroscopic state to the equilibrium distribution. We parameterize both the sufficient statistics and the natural parameters with neural networks,

$$\phi_i^{\text{NN}}(t, \mathbf{x}) \stackrel{\text{def.}}{=} \exp\left(\boldsymbol{\lambda}(\mathbf{U}(t, \mathbf{x}); \theta^\lambda) \cdot \boldsymbol{\varphi}(\mathbf{c}_i; \theta^\varphi)\right) = \exp\left(\sum_{k=1}^p \boldsymbol{\lambda}_k(\mathbf{U}(t, \mathbf{x}); \theta^\lambda) \boldsymbol{\varphi}_k(\mathbf{c}_i; \theta^\varphi)\right), \quad (6)$$

where  $p$  is the number of learned bases. As illustrated in Fig. 1b, this two-part architecture uses separate networks— $\boldsymbol{\varphi}(\cdot; \theta^\varphi)$  and  $\boldsymbol{\lambda}(\cdot; \theta^\lambda)$ —to learn the basis and coefficients, respectively. This design preserves the crucial exponential-family structure while reducing the expensive inversion step to two fast forward passes, making high-order entropic closures feasible for large-scale simulations.

NeurDE induces higher-order, non-polynomial velocity moments that lie outside any fixed Taylor basis. To capture phenomena further from equilibrium,  $p$  must be chosen sufficiently large to span high-order observables (e.g. heat flux and pressure tensor). This learned and expanded moment set not only enhances expressivity far from equilibrium, but it also circumvents the polynomial-aliasing errors (Subsec. B.10) that plague classical low-order closures. Specifically, overcoming the lattice aliasing allows us to model these required high-order observables. Although NeurDE’s structure resembles other operator networks architectures [55], it is derived from our entropic closure and is tailored specifically to the physical constraints of kinetic theory.

To illustrate how NeurDE can be used in a realistic SciML application, we integrate NeurDE within the LB framework, yielding the LB+NeurDE Algorithm (Fig. 2 Algorithm b). LB+NeurDE applies ML to the unknown collision term while leveraging the LB framework to numerically evolve the discrete kinetic equations (Eq. (4)) using the lattice velocities  $\{\mathbf{c}_i\}_{i=1}^Q$ . A single time step of this hybrid propagation consists of two main subroutines. The first routine, NeurDE calculates the equilibrium distribution  $\mathbf{f}^{\text{eq}}$  from the macroscopic observables  $\mathbf{U}$  derived from  $\mathbf{f}^{\text{eq}}$  (Fig. 2 Algorithm c.1). The second routine, the `splitting` subroutine (Fig. 2 Algorithm c.2), performs the standard collide-stream update. During the collision (Eq. (5a)), the system relaxes toward the learned equilibrium, while the subsequent streaming step (Eq. (5b)) is realized as an efficient lattice shift (Fig. 2 Algorithm c.2, line 2) [49].

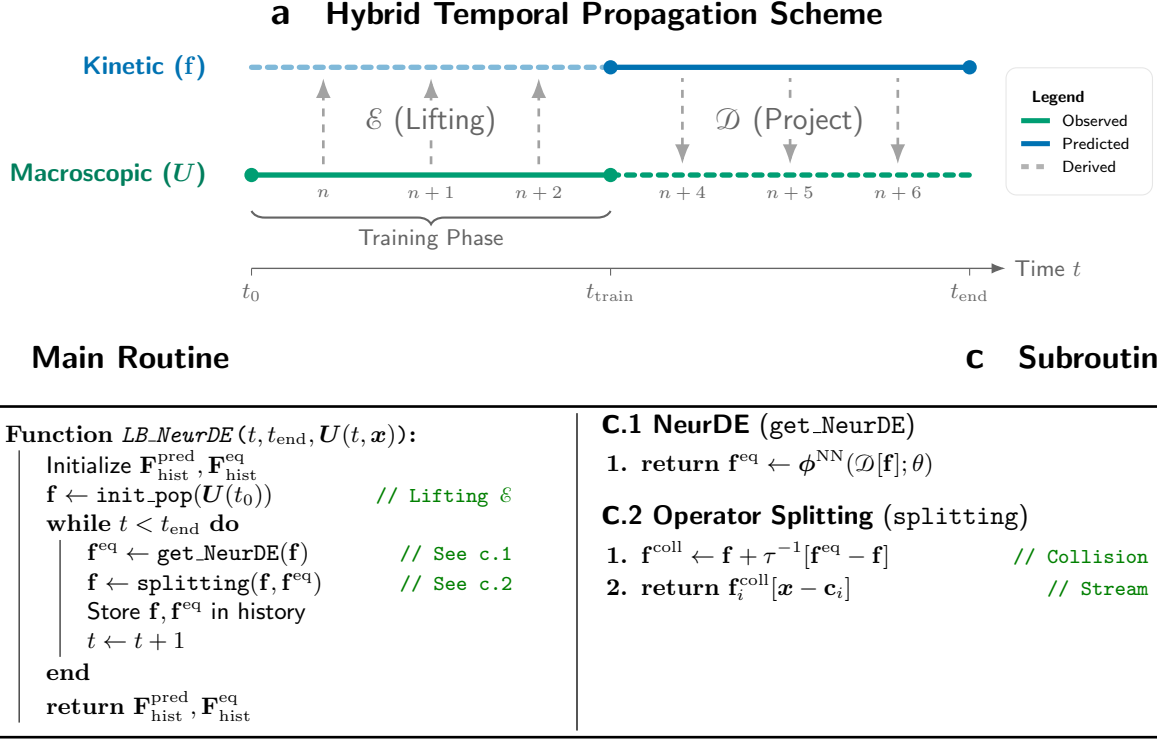


**Figure 2: Hybrid kinetic-macroscopic propagation.** (a) Kinetic distributions  $\mathbf{f}$  (blue) and macroscopic observables  $\mathbf{U}$  (green) evolve via lifting operator  $\mathcal{E}$  and projection  $\mathcal{D}$ . The model trains on observed data ( $t_0 \rightarrow t_{\text{train}}$ ) before predicting future states ( $t > t_{\text{train}}$ ). (b) The main routine alternates between Neural Network equilibrium prediction (Line 5) and operator splitting (Line 6). (c) Subroutines detailing the projection-learning step (`get_NeurDE`) and the collision-streaming step (`splitting`).

This hybrid formulation provides several critical advantages over traditional entropic schemes, which are hampered by the computational cost of a root-finding algorithm required at each point in space-time [47]. Instead, LB+NeurDE significantly accelerates the equilibrium computation by amortizing this inversion into a fast forward pass. Furthermore, the learned, non-polynomial basis functions decouple the model’s physical fidelity from the algebraic constraints of the discrete velocity set (Subsec. B.10). This effectively creates a quadrature-free approach, enabling the simulation of higher-order physics on small, efficient velocity lattices that are normally restricted to simpler dynamics.

LB+NeurDE leverages the lattice to numerically solve the NeurDE-adapted Boltzmann-BGK equation, however, other techniques can be employed. Varying numerical integration schemes will create different NeurDE variants: finite volume (FV+NeurDE); finite element (FE+NeurDE); finite difference (FD+NeurDE); and discontinuous Galerkin (DG+NeurDE). Still, in all of these approaches, velocity must be discretized to calculate the macroscopic variables (Eq. (3)). LB+NeurDE is the preferred method as the lattice exactly solves the streaming operation without error accumulation that can occur in other methods (e.g. flux calculation in FV+NeurDE). Moreover, the streaming computationally reduces to a memory (pointer) shift, making it extremely fast. By making the lattice learnable, one could formulate a fully neural architecture. In this case, the streaming step provides spatial propagation and can be represented as a fixed linear convolution shifting populations along discrete velocities (see Subsec. C.3), and the residual neural collision operator performs a local nonlinear transformation parameterized by NeurDE (Eq. (6)). Following the training protocols detailed in Sec. D, we focus on the subsonic shock tube case (Subsecs. 2.3.1 and E.1) to evaluate the streaming experiment described in Subsec. F.2. Here, we evaluate this fully neural structure by learning the streaming operator; and we find that it obtains strictly *worse* results, essentially since the lattice shift is an exact solution to Eq. (5b) (and thus this does not need to be learned via data).

## 2.3 Empirical Evaluation

We empirically validate LB+NeurDE (Fig. 2) across compressible flow regimes where conventional LB schemes with low-order polynomial equilibria typically lose stability or accuracy. We examine three representative regimes—subsonic, transonic, and supersonic—that expose the two main failure modes of classical LB formulations: (i) increasing closure error at elevated Mach numbers, where higher-order moments become under-resolved [25, 47]; and (ii) numerical stiffness at low viscosities [46, 21]. We further assess the stability and generalization of LB+NeurDE by evaluating it far beyond its training regime to determine whether it learns a physically consistent closure, rather than merely interpolating within the training manifold. Subsec. 4.2 details our specific implementation of LB+NeurDE for compressible fluids.

In the following tests, we train LB+NeurDE on the first 500 time steps of a single simulation. See Sec. 4 for details of our training procedure. We evaluate LB+NeurDE on a further 500 time steps and compute pressure from the ideal gas law  $p = R\rho T$  with  $R = 1$ .

### 2.3.1 1D Riemann’s Problem: Sod Shock Tube

The Sod shock tube [74] is a standard benchmark for compressible solvers, testing the ability to capture rarefaction waves, contact discontinuities, and shocks. We assess LB+NeurDE in two regimes: a simple *subsonic* case; and a demanding *transonic* case. For comparison with traditional LB schemes, we use a two-population baseline with a low-order Hermite expansion of  $\mathbf{g}^{\text{eq}}$  (cf. [38, 69], Eq. (53)). While accurate at low Mach numbers, this approximation fails in the transonic regime, underscoring the robustness of LB+NeurDE. Implementation details are in Sec. E.

We further benchmark LB+NeurDE against FNO [52] by applying FNO to the subsonic Sod experiment (Subsec. E.1.3). We selected configurations that maximize the number of Fourier modes that are feasible on our hardware (4 80 GB A100 GPUs), ensuring the baseline is limited by its inductive bias rather than by insufficient capacity. We find that FNO struggles significantly with shocks, even when predicting a single time step (Fig. 14).

LB+NeurDE accurately reconstructs the evolution far beyond the training window ( $t > 500$ ), reproducing the rarefaction fan, contact discontinuity, and shock without Gibbs oscillations (Fig. 3(a – d)). A minor localized deviation appears near the contact discontinuity at late times, but it does not grow.

The standard LB polynomial equilibrium scheme [38] generates spurious temperature spikes at the contact discontinuity for the subsonic case, and it quickly fails (after roughly 10 steps) in the transonic case. Shock-front oscillations occur in both methods, consistent with [24], but they are markedly smaller in LB+NeurDE. Under subsonic conditions (Subsec. E.1.1), the polynomial closure remains stable but less accurate: it overestimates the pre-shock velocity plateau and underestimates the post-shock plateau, while LB+NeurDE reproduces both plateau heights and shock position to within line-width precision of the high-fidelity reference (values obtained using the root-finding procedure of [47]).

The transonic regime pushes the LB scheme towards its stability limit, as classical polynomial closures fail to extremize entropy Eq. (19), leading to unphysical growth of high-order kinetic moments near shocks and steep gradients, and potentially negative distributions. The polynomial LB diverges after ten steps due to rapidly growing fourth-order moment errors (Subsec. E.2.5). In contrast, NeurDE remains entropy-consistent, preserving positivity and extremizing the H-function, Eq. (19) [51, 48, 47, 78]. LB+NeurDE reproduces the rarefaction, contact discontinuity, and shock up to  $t = 999$  (Fig. 3(e – h)). The remaining late-time discrepancies are small and localized, demonstrating the robustness of the learned closure at transonic Mach numbers.

### 2.3.2 2D Supersonic Flow

To assess the performance of LB+NeurDE in high-speed two-dimensional flows, we consider the canonical problem of supersonic flow past a cylinder, following [80, 47]. This benchmark probes the model’s ability to capture detached shocks, shear layers, and compressible recirculation regions—flow features that typically challenge low-order polynomial equilibria.

LB+NeurDE accurately reproduces the flow structure after 200 time steps, well beyond the training regime ( $t \leq 500$ ). Fig. 4(b) shows the detached bow shock, subsonic recirculation bubble, shear-layer separation, and

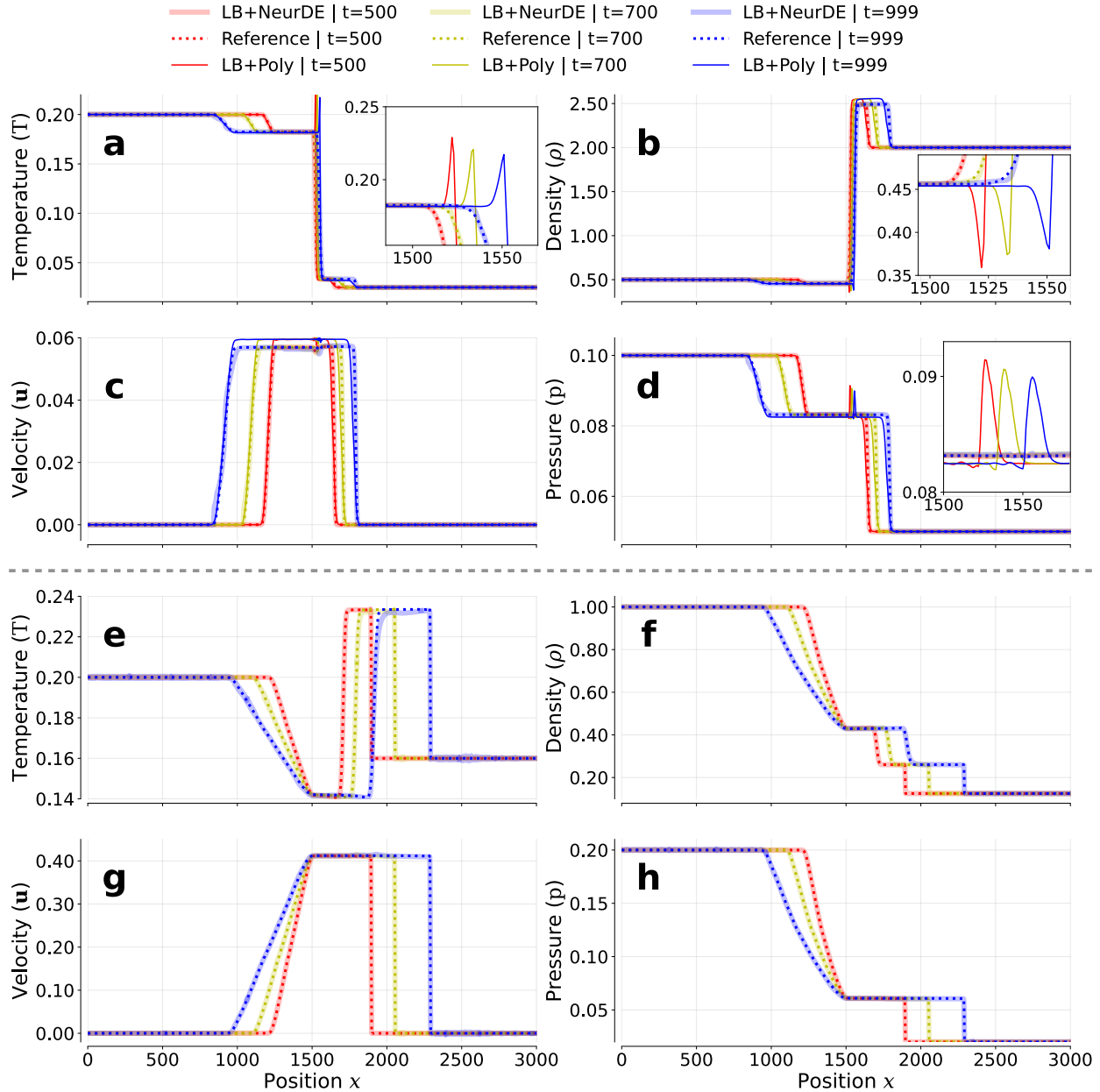


**Figure 3:** Inference results for the subsonic (case 1, Eq. (10)) and transonic (case 2, Eq. (11)) Sod shock tube at  $t = 500, 700, 999$  after training on  $t < 500$ . Panels a, b, c, and d, respectively, illustrate the temperature, density, velocity, and pressure evolution for the subsonic case. Panels e – h are the analogous plots for the transonic case. The small solid line represents the polynomial LB expansion of  $\mathbf{f}^{\text{eq}}$  and  $\mathbf{g}^{\text{eq}}$  (Eqs. (52) and (53), respectively), the large and transparent solid lines represent LB+NeurDE predictions, and the dotted lines show simulated ground truth. In the transonic case, the polynomial LB expansion diverges after 10 steps and is thus omitted.

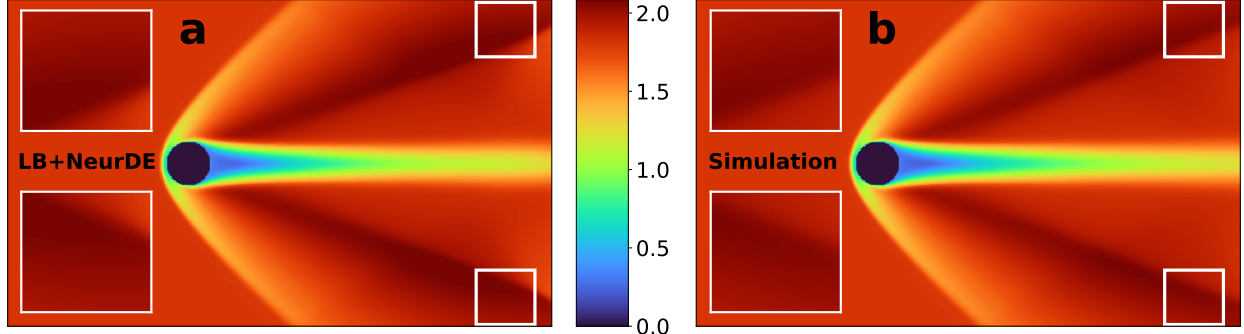


**Figure 4:** Prediction for the supersonic flow around a cylinder with  $Re = 300$  and  $Ma_\infty = 1.8$ . Panel a illustrates our 2D supersonic flow boundary conditions: free streaming condition on the top and bottom (blue line,  $\Gamma_3$ ), Dirichlet boundary conditions at the inlet (red line,  $\Gamma_1$ ), first-order Neumann conditions at the outlet (green line,  $\Gamma_2$ ), and no slip conditions on the circle (black circle,  $\Gamma_4$ ). Panels b and c depict the local Mach number obtained from the simulation at time-step 700 (in lattice units) for the hybrid model  $\Phi_S \Phi_C^{NN}$  and for the reference using  $g_i^{eq}$  as described in Eq. (54), respectively. The insets highlight regions with the largest deviation between LB+NeurDE and the simulated results.

downstream recompression shocks. The sonic line is sharply resolved, and the recompression region exhibits the correct topology [3]. At Reynolds number 300, the flow remains steady and laminar.

Classical polynomial equilibria diverge, consistent with their breakdown at transonic speeds, due to under-resolved higher-order moments [25, 47]. By contrast, LB+NeurDE stays stable, with deviations from the reference localized near the outlet (Fig. 4b–c). Although the closure does not strictly enforce boundaries, the discrepancies do not affect global flow or shock topology.

## 2.4 Performance at Long Times and Unseen Conditions

Hybrid frameworks provide structure that allows them to generalize, yet NeurDE can encounter states far outside the training distribution during long-time evolution or shifted initial conditions [68, 56, 76, 30, 44]. To evaluate LB+NeurDE’s robustness under such conditions, we reinitialize inference at times well beyond the training window and evolve the system, without retraining. Accurately predicting nonlinear flow evolution well beyond the training horizon is a stringent test for any data-driven model, particularly in regimes with shocks, contact discontinuities, and rarefaction waves, such as the Sod shock tube and supersonic cylinder flow. Standard evaluations ( $\lesssim 500$  steps for the shock tube,  $\lesssim 200$  for the cylinder) may overestimate reliability. To avoid this overoptimism [58], we design extrapolation experiments probing the limits of model generalization.

### 2.4.1 Sod Shock Tube

We use the same model trained in Subsec. 2.3.1 with 500 time points (blue in Fig. 5a), to predict 100 time steps starting from  $t = 2000$  (green in Fig. 5a) without retraining. This corresponds to skipping the first 1500 time steps (red and black in Fig. 5a), predicting three times beyond the length of the training data. During this period, we expect that the evolution of the discontinuities is vastly different than those seen by NeurDE during training—blue line. Fig. 5 shows the prediction result (blue) plotted against the earlier evaluated point (red and yellow) to highlight the large change in shape. In both the subsonic and transonic cases, LB+NeurDE closely matches the reference at  $t = 2099$ , well beyond the training window, demonstrating its robustness and ability to extrapolate accurately.

At later prediction times, LB+NeurDE begins to deviate (see Subsecs. E.1.2 and E.2.6 for details). For the subsonic case (Eq. (10)), deviations occur when initialized at  $t_0 = 3900$ , predicting the next 100 time steps. In the more challenging transonic case (Eq. (11)), LB+NeurDE starts oscillating at  $t_0 = 2500$  while predicting the following 100 steps.

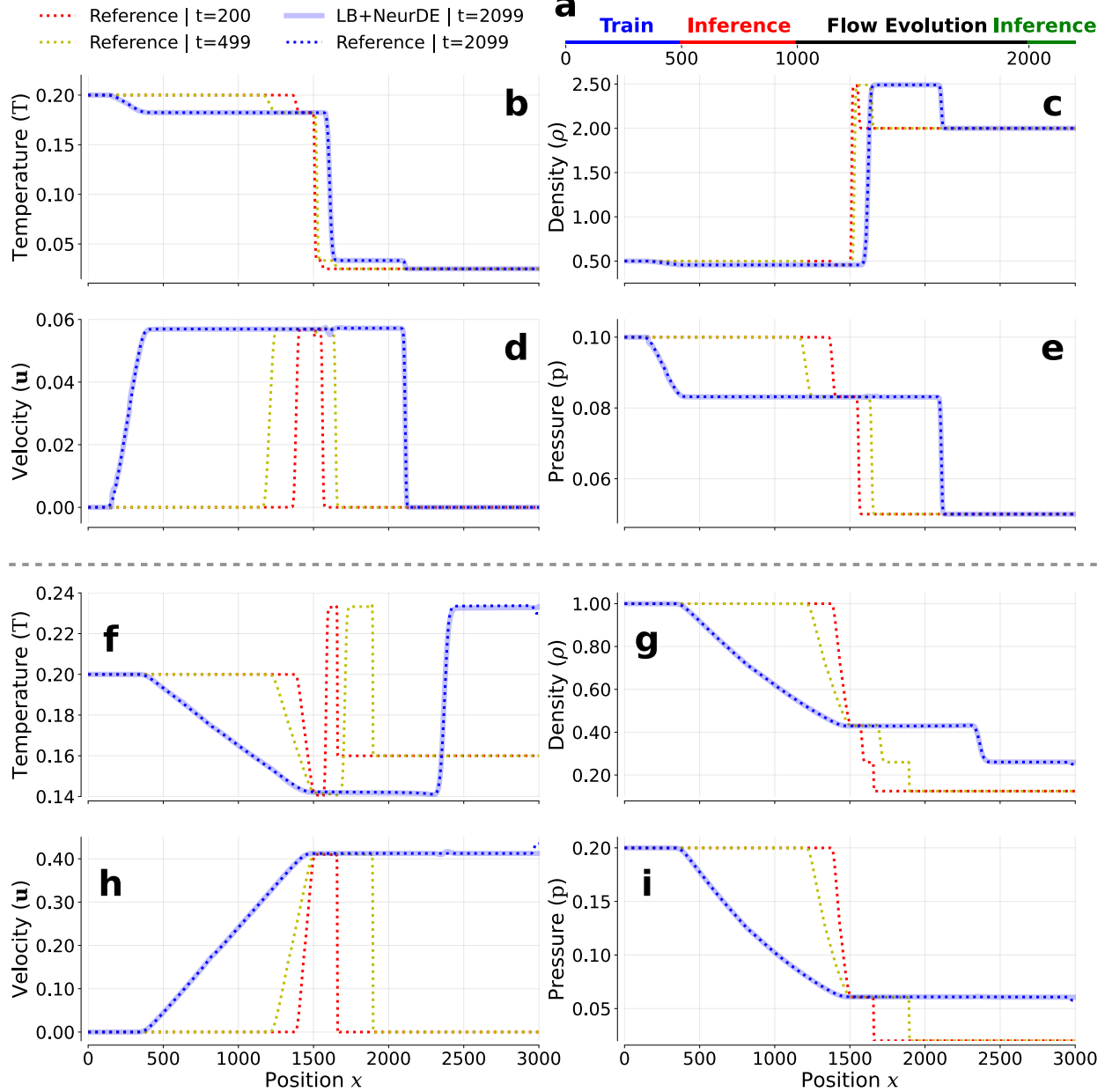


**Figure 5:** Long-term prediction for the (top) and transonic (bottom) Sod shock tube (Subsec. 2.3.1) at  $t = 2099$ , with initial condition  $t = 2000$ . The model is trained using the first 500 time steps of the dataset. The timeline of training, early inference, flow evolution, and long-time evolution presented here is shown in panel a. Panels b, c, d, and e show the temperature, density, velocity, and pressure profiles, respectively, for the subsonic case. Panels f – i show the analogous plots for the transonic case.

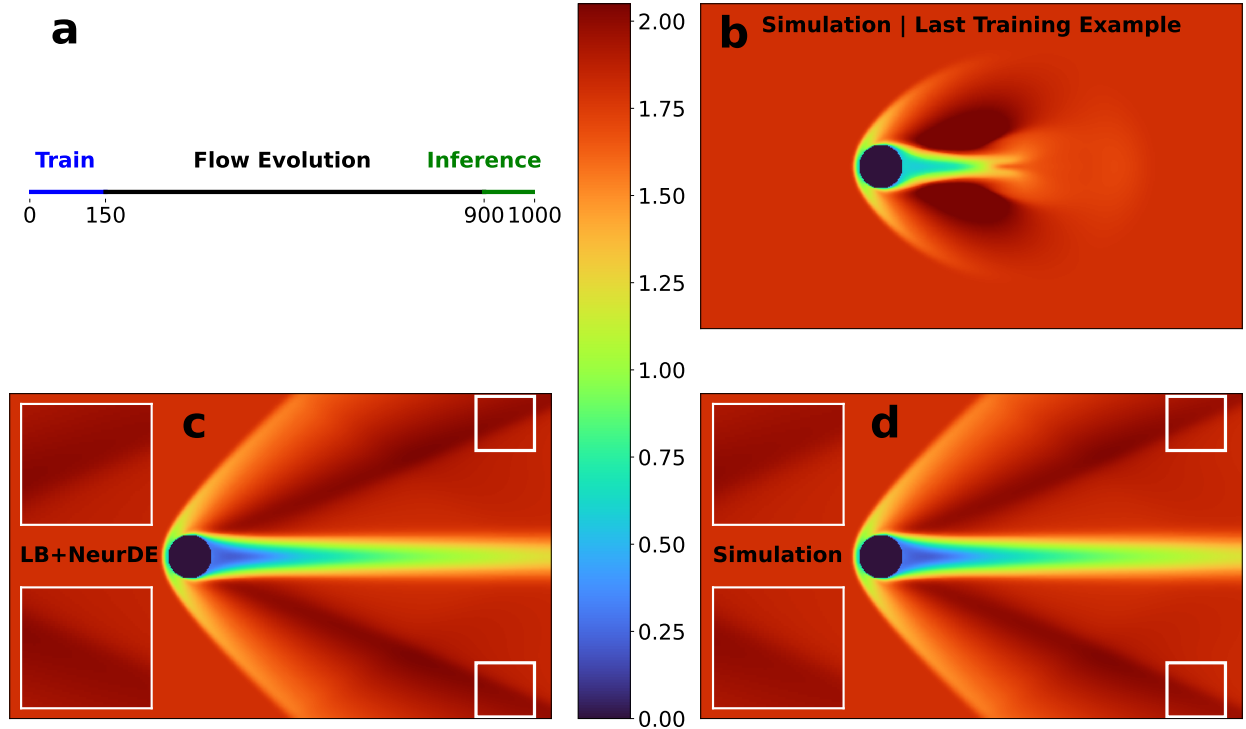


**Figure 6:** Comparison of LB+NeurDE’s performance on long-time predictions with a shortened training time and an initialization time of 900, depicted in panel a. Panels b, c, and d show the Mach number. Panel b shows the last training step seen by LB+NeurDE at  $t = 150$ . Panels c and d show the local Mach number at  $t = 999$  for LB+NeurDE (initialized at  $t_0 = 900$ ) and numerical results, respectively. Notably, there is a significant change in the evolution of the discontinuities, indicating that NeurDE, combined with the LB scheme, accurately captures these dynamics even at distances far from the training dataset.

#### 2.4.2 Supersonic Flow Around a Cylinder

The cylinder flow reaches a steady state quickly because of the low Reynolds number, limiting the information gained from long-time extrapolation. Here, we train a new model using the same architecture; see Table 2. The model is trained on only 150 time steps (blue in Fig. 6a)—before the appearance of bow, recompression, and separation shocks (shown in Fig. 6b)—and tested at  $t_0 = 900$ , when these structures are fully developed (black in Fig. 6a). We then predict the subsequent 100 time steps (green in Fig. 6a), testing whether it can reconstruct flow features it never encountered during training.

LB+NeurDE accurately recovers the shock structure and overall flow field at  $t = 999$  (Fig. 6c–d). The deviations remain localized near the outlet boundaries and do not compromise the overall solution. Since the steady state is reached by  $t \approx 600$ , the model effectively reconstructs the underlying physical structure from unseen states rather than relying on interpolation. Additional macroscopic variables are reported in Subsec. G.2.

### 3 Discussion

We have introduced a new operator network (NeurDE) and a surrogate kinetic solver (LB+NeurDE) that integrates a strong physics bias, stability from numerical methods, and flexibility from ML methods, to model conserved systems. NeurDE builds upon classical kinetic theory [8, 1, 36], while embedding a trainable operator networks within the equilibrium state. This design preserves the core structure of the kinetic scheme while extending its applicability through data-driven flexibility. LB+NeurDE offers several advantages over classical LB schemes. It overcomes the breakdown of low-order polynomial equilibria at high Mach

numbers caused by under-resolved higher-order moments; projects arbitrarily many moments without explicit quadrature, eliminating truncation errors; removes nonlinear root-finding in entropic closures [47, 80, 25]; and incorporates partially known physics by inferring missing equilibrium components from data.

A key difference from purely data-driven approaches lies in how physical structure is retained. Standard operator-learning models approximate the entire evolution operator [42, 52, 34, 12], an approach which limits stability and extrapolation to unseen regimes with shocks or stiff dynamics. In contrast, LB+NeurDE confines learning to the equilibrium operator, thereby yielding a compact four-layer network (fewer than 100 parameters per layer; Table 2) that preserves well-posedness and stability. This design enables accurate long-horizon forecasts and robust generalization to distant initial conditions (Subsec. 2.4).

The NeurDE architecture’s ability to learn equilibrium closures extends naturally to broader hyperbolic and multiphysics systems—such as rarefied gases, plasma flows, and geophysical or astrophysical fluids—where governing equations are partially known and/or multiscale. Embedding learning within a kinetic formulation offers a principled route to stable, interpretable, and data-adaptive solvers for such regimes.

## 4 Methods

### 4.1 Constructing the Neural Moment Space

The core of the NeurDE framework is the parameterization of the equilibrium manifold. We define the network’s expressivity through a learned moment space

$$\mathbb{M} \stackrel{\text{def.}}{=} \text{span} \{ \varphi_k(\mathbf{c}_i) : i = 1, \dots, Q, \text{ and } k = 1, \dots, p \}, \quad (7)$$

where  $\mathbf{c}_i$  represents the discrete lattice velocities. The design of this space is governed by two competing requirements: conservation and expressivity.

To guarantee the conservation of mass, momentum, and energy, we explicitly enforce that the standard Eulerian moments,  $\text{span}\{1, \mathbf{c}_i, \mathbf{c}_i \cdot \mathbf{c}_i\}$ , are contained in  $\mathbb{M}$  during training. Simultaneously, to capture non-equilibrium phenomena that escape classical low-order closures, we select the dimension  $p$  to be sufficiently large. This allows the network to learn a higher-order basis capable of representing complex flux and stress terms, enhancing physical fidelity at the expense of model complexity (see Subsec. B.6).

### 4.2 Realization in Compressible Fluid Dynamics

With the mathematical structure of the equilibrium defined, we now turn to its practical implementation within a numerical solver. To demonstrate the framework’s capability in challenging regimes (Subsecs. 2.3.1 and 2.3.2), we implement NeurDE within a compressible LB solver. We adopt a two-population thermal formulation to accommodate variable specific heat ratios ( $\gamma$ ) and Prandtl numbers (Pr) [80, 69, 25], which are restricted to fixed values in standard kinetic schemes.

The evolution of the system is split into two coupled relaxation processes, following the formulation of [38, Eq. 74–75]. The population  $\mathbf{f}_i$  transports mass and momentum, while a separate population  $\mathbf{g}_i$  transports energy. Their dynamics are governed by:

$$\mathbf{f}_i(t+1, \mathbf{x} + \mathbf{c}_i) - \mathbf{f}_i(t, \mathbf{x}) = \frac{1}{\tau_1}(\mathbf{f}_i^{\text{eq}} - \mathbf{f}_i), \quad (8a)$$

$$\mathbf{g}_i(t+1, \mathbf{x} + \mathbf{c}_i) - \mathbf{g}_i(t, \mathbf{x}) = \frac{1}{\tau_2}(\mathbf{g}_i^{\text{eq}} - \mathbf{g}_i) + \left(\frac{1}{\tau_2} - \frac{1}{\tau_1}\right)(\mathbf{g}_i^* - \mathbf{g}_i). \quad (8b)$$

This decoupling, mediated by the intermediate quasi-equilibrium  $\mathbf{g}^*$  (see Eq. (50)) allows us to independently set the viscosity ( $\mu \propto \tau_1$ ) and the thermal conductivity ( $\kappa \propto \tau_2$ ) [69]. The macroscopic quantities—density  $\rho$ , velocity  $\mathbf{u}$ , and temperature  $T$ —are recovered by taking moments over these populations

$$\rho = \langle \mathbf{f} \rangle, \quad \rho \mathbf{u} = \langle \mathbf{c} \mathbf{f} \rangle, \quad E = \frac{1}{2\rho} \langle \mathbf{g} \rangle, \quad T = \frac{1}{C_v} (E - \frac{1}{2} \mathbf{u} \cdot \mathbf{u}), \quad (9)$$

with  $C_v$  and  $C_p$  the specific heats and  $\gamma = C_p/C_v$ ,  $\text{Pr} = C_p\mu/\kappa$ . See Subsec. D.1.

### 4.3 Hybrid Closure and Training

Targeting the specific challenges of high-Mach flows, we implement a **Hybrid Closure Strategy** within the double-population formulation (Eq. (8)) that strictly delineates which physical components are learned. We utilize the analytic extended equilibrium (Eq. (52)) for the momentum distribution  $\mathbf{f}_i^{\text{eq}}$ , while delegating the complex energy closure  $\mathbf{g}_i^{\text{eq}}$  entirely to NeurDE. Where traditional high-Mach LB solvers require explicit correction terms and non-local operations to maintain stability [69], our approach avoids these costly interventions by learning the correct closure directly from data.

To enforce physical consistency across scales, the training procedure for NeurDE (Algorithm 1) proceeds in two stages, explicitly aligning the optimization with both the mesoscopic statistical description and the macroscopic continuum dynamics (see panel (a) in Fig. 2).

1. **Static Pre-training (Mesoscopic Prior):** First, we instill a robust physical prior by training NeurDE to map known macroscopic states  $\mathbf{U}$  to high-fidelity equilibrium distributions derived from static data. This ensures that, even before temporal dynamics are introduced, NeurDE resides on a physically plausible manifold.
2. **Dynamic Training (Macroscopic Consistency):** Second, we train the solver dynamics through temporal forecasting. We integrate the pre-trained NeurDE into the LB solver and perform multi-step rollouts, comparing the predicted macroscopic trajectories against high-fidelity simulations. By minimizing the cumulative error over time, we ensure that the locally accurate equilibria learned in stage one compose correctly to produce stable global dynamics, as in [47].

### 4.4 Experimental Configurations

Having established the solver architecture and training protocol, we validate the framework against three distinct flow regimes, each designed to probe specific failure modes of classical schemes.

#### 4.4.1 Subsonic Baseline

We first calibrate the method on a standard subsonic Sod shock tube to verify the accurate capture of rarefaction waves, contact discontinuities, and shocks. We employ a specific heat ratio  $\gamma = 2.0$  and Prandtl number  $\text{Pr} = 0.71$ . The flow is initialized with a density ratio of 5 : 1 and a temperature ratio of 8 : 1:

$$(\rho, \mathbf{u}_x, \mathbf{u}_y, T) = \begin{cases} (0.5, 0, 0, 0.2), & x/L_x \leq 1/2, \\ (2.5, 0, 0, 0.025), & x/L_x > 1/2 \end{cases} \quad (10)$$

with  $L_x = 3001$  [74]. To mitigate Galilean invariance errors inherent to discrete velocity lattices, we apply a small reference frame shift  $\mathbf{u}_{\text{shift}} = (\frac{3}{50}, 0)$  in LB+NeurDE, following [26].

**Benchmarking against Operator Learning:** To isolate the benefits of the hybrid kinetic architecture, we establish a comparative baseline using a Fourier Neural Operator (FNO) trained on this same configuration. This comparison highlights the distinction between the physics-embedded LB+NeurDE and purely data-driven operator learning, particularly regarding conservation and shock resolution. The FNO baseline employs a standard 2D architecture trained with a relative  $L_2$  loss. Capturing shock dynamics is challenging for Neural Operators [58, 70], and is known to be challenging for spectral methods like FNO. To ensure that our FNO benchmark is limited by the model’s inductive biases rather than its computational requirements, we prioritize large numbers of Fourier modes. We increase the model’s Fourier mode capacity until we are limited by our combined 320 GB memory limit on our (combined) 4 A100 80 GB accelerators. We explicitly set the spectral truncation to  $\mathbf{k}_{\text{max}} \in \{(128, 3), (256, 3), (512, 3)\}$ , the embedding dimension  $d_v \in \{128, 246\}$ , and the number layers  $l \in \{4, 8\}$ . Subsec. E.1.3 provides further details of our hyperparameter tuning.

While FNO is a data-driven architecture, its reliance on spectral convolutions to achieve a global receptive field introduces a specific inductive bias towards periodic continuous functions. To address the non-periodic boundaries of the Sod shock tube and mitigate spectral leakage, we implement a *Palindromic Edge-Padded Extension* (Fig. 11). This forces  $C^1$  continuity at the periodic wrap of the fast Fourier Transform (FFT) inputs. However, despite this rigorous pre-processing, the global support of the underlying Fourier basis

functions persists within the learned operator, resulting in characteristic Gibbs phenomenon oscillations near shock discontinuities (Figs. 12 to 14). This isolates the difficulty of capturing sharp hyperbolic features using global frequency-domain approximations. Comprehensive details regarding the boundary handling are provided in Subsec. E.1.3.

#### 4.4.2 Transonic Baseline

To probe stability limits, we simulate a transonic shock tube with low viscosity ( $\mu = 10^{-4}$ ), approaching the theoretical stability bound of the collision operator ( $\tau_1 \rightarrow 1/2$ , Eq. (49)). In this stiff regime, standard polynomial closures typically fail due to the under-resolution of high-order moments. We set  $\gamma = 1.4$  and initialize the flow with:

$$(\rho/\rho_0, \mathbf{u}_x/\sqrt{\mathbf{u}_0 \cdot \mathbf{u}_0}, \mathbf{u}_y/\sqrt{\mathbf{u}_0 \cdot \mathbf{u}_0}, p/p_0) = \begin{cases} (1.0, 0, 0, 1.0), & x/L_x \leq 1/2, \\ (0.125, 0, 0, 0.1), & x/L_x > 1/2. \end{cases} \quad (11)$$

and  $\gamma = 1.4$ ,  $\text{Pr} = 0.71$ , and  $L_x = 3001$ . To maintain stability in the presence of strong discontinuities, we apply a larger velocity shift of  $(\frac{2}{5}, 0)$  and regularize the training with a Total Variation Diminishing (TVD) penalty to suppress spurious Gibbs oscillations (see Subsec. E.2.2) [26]. Near Mach 1 (Fig. 16), the polynomial equilibria fail to capture high-order moments, leading to breakdowns unrelated to  $\tau \rightarrow 1/2$  but to closure errors at transonic speeds.

#### 4.4.3 2D Supersonic Interaction

Finally, we test geometric and supersonic flow using flow past a cylinder. The Reynolds number is  $\text{Re} = 300$  (based on cylinder diameter), the far-field Mach number  $\text{Ma}_\infty = 1.8$ , temperature  $T_\infty = 0.2$ , and  $\gamma = 1.4$ . The local Mach number is  $\text{Ma} = \mathbf{u} \cdot \mathbf{u}(\gamma RT)^{-1/2}$ , assuming an ideal gas with  $R = 1$ . We apply a lattice velocity shift  $\mathbf{u}_{\text{shift}} = \frac{3}{5}(\sqrt{\gamma T_\infty}, \text{Ma}_\infty, 0)$ , with the 3/5 coefficient chosen empirically to reduce spurious bow-shock oscillations.

Dirichlet conditions are imposed at the inlet for  $\rho$ ,  $\mathbf{u}$ , and  $T$ , first-order Neumann conditions at the outlet, free-streaming conditions along the top and bottom boundaries, and no-slip/no-penetration on the cylinder wall via bounce-back (Fig. 4a). The reference solution employs an exponential moment closure for  $\mathbf{g}_i^{\text{eq}}$  obtained via root finding [47], combined with the extended equilibrium  $\mathbf{f}_i^{\text{eq}}$  (Eq. (52)).

## Data availability

The source code used to produce the results presented in this study is openly available on GitHub at <https://github.com/JALB-epsilon/NeurDE>.

## Acknowledgments

J.A.L.B. extends sincere appreciation to Jesse Chan and Khemraj Shukla for their thought-provoking discussions, which have greatly contributed to the enhancement of this work. J.A.L.B. and K.H. acknowledge the computational support provided by the Lawrence Berkeley National Laboratory (LBNL). J.A.L.B and K.H. thank Yotam Yaniv for his assistance in the FNO experiments. M.V. de H. gratefully acknowledges support from the DOE under grant DE-SC0020345, the NSF under grant DMS-2108175, the Simons Foundation under the MATH+ X program (Award# 271853, Project “Simons Chair in Computational and Applied Mathematics and Earth Science at Rice University”), and Occidental Petroleum (Oxy). M.W.M. would like to acknowledge the DOE, NSF, and ONR for providing partial support of this work. I.D. acknowledges support by the European Research Council (ERC) Starting Grant 852821—SWING.

## References

- [1] Denise Aregba-Driollet and Roberto Natalini. Discrete kinetic schemes for multidimensional systems of conservation laws. *SIAM Journal on Numerical Analysis*, 37(6):1973–2004, 2000.
- [2] Vladimir Vladimirovich Aristov and Feliks Grigor’evich Cheremisin. Splitting of the inhomogeneous kinetic operator of the boltzmann equation. In *Akademii Nauk SSSR Doklady*, volume 231, pages 49–52, 1976.
- [3] M Awasthi, S McCreton, DJ Moreau, and CJ Doolan. Supersonic cylinder wake dynamics. *Journal of Fluid Mechanics*, 945, 2022.
- [4] Thomas Bellotti. Truncation errors and modified equations for the lattice boltzmann method via the corresponding finite difference schemes. *ESAIM: Mathematical Modelling and Numerical Analysis*, 57(3):1225–1255, 2023.
- [5] Thomas Bellotti, Benjamin Graille, and Marc Massot. Finite difference formulation of any lattice boltzmann scheme. *Numerische Mathematik*, 152(1):1–40, 2022.
- [6] Jose Antonio Lara Benitez, Takashi Furuya, Florian Faucher, Anastasis Kratsios, Xavier Tricoche, and Maarten V de Hoop. Out-of-distributional risk bounds for neural operators with applications to the helmholtz equation. *Journal of Computational Physics*, page 113168, 2024.
- [7] Prabhu Lal Bhatnagar, Eugene P Gross, and Max Krook. A model for collision processes in gases. i. small amplitude processes in charged and neutral one-component systems. *Physical review*, 94(3):511, 1954.
- [8] François Bouchut. Construction of bgk models with a family of kinetic entropies for a given system of conservation laws. *Journal of statistical physics*, 95:113–170, 1999.
- [9] Johannes Brandstetter, Daniel Worrall, and Max Welling. Message passing neural pde solvers. *arXiv preprint arXiv:2202.03376*, 2022.
- [10] Steven L Brunton and J Nathan Kutz. Promising directions of machine learning for partial differential equations. *Nature Computational Science*, 4(7):483–494, 2024.
- [11] Russel E Caflisch and Basil Nicolaenko. Shock profile solutions of the boltzmann equation. *Communications in Mathematical Physics*, 86(2):161–194, 1982.
- [12] Shengze Cai, Zhiping Mao, Zhicheng Wang, Minglang Yin, and George Em Karniadakis. Physics-informed neural networks (pinns) for fluid mechanics: A review. *Acta Mechanica Sinica*, 37(12):1727–1738, 2021.
- [13] Carlo Cercignani. The boltzmann equation. In *The Boltzmann equation and its applications*, pages 40–103. Springer, 1988.
- [14] Bo Chang, Lili Meng, Eldad Haber, Frederick Tung, and David Begert. Multi-level residual networks from dynamical systems view. *arXiv preprint arXiv:1710.10348*, 2017.
- [15] Ricky T. Q. Chen, Yulia Rubanova, Jesse Bettencourt, and David K Duvenaud. Neural ordinary differential equations. In S. Bengio, H. Wallach, H. Larochelle, K. Grauman, N. Cesa-Bianchi, and R. Garnett, editors, *Advances in Neural Information Processing Systems*, volume 31, 2018.
- [16] Shiyi Chen and Gary D Doolen. Lattice boltzmann method for fluid flows. *Annual review of fluid mechanics*, 30(1):329–364, 1998.
- [17] Xiaoli Chen, Beatrice W Soh, Zi-En Ooi, Eleonore Vissol-Gaudin, Haijun Yu, Kostya S Novoselov, Kedar Hippalgaonkar, and Qianxiao Li. Constructing custom thermodynamics using deep learning. *Nature Computational Science*, 4(1):66–85, 2024.

[18] Alessandro Corbetta, Alessandro Gabbana, Vitaliy Gyrya, Daniel Livescu, Joost Prins, and Federico Toschi. Toward learning lattice boltzmann collision operators. *The European Physical Journal E*, 46(3):10, 2023.

[19] Christophe Coreixas, Bastien Chopard, and Jonas Latt. Comprehensive comparison of collision models in the lattice boltzmann framework: Theoretical investigations. *Physical Review E*, 100(3):033305, 2019.

[20] Paul J Dellar. Lattice kinetic schemes for magnetohydrodynamics. *Journal of Computational Physics*, 179(1):95–126, 2002.

[21] Paul J Dellar. An interpretation and derivation of the lattice boltzmann method using strang splitting. *Computers & Mathematics with Applications*, 65(2):129–141, 2013.

[22] Wolfgang Dreyer. Maximisation of the entropy in non-equilibrium. *Journal of Physics A: Mathematical and General*, 20(18):6505, 1987.

[23] Xiantao Fan and Jian-Xun Wang. Differentiable hybrid neural modeling for fluid-structure interaction. *Journal of Computational Physics*, 496:112584, 2024.

[24] Yongliang Feng, Pierre Sagaut, and Wen-Quan Tao. A compressible lattice boltzmann finite volume model for high subsonic and transonic flows on regular lattices. *Computers & Fluids*, 131:45–55, 2016.

[25] Nicolò Frapolli, Shyam S Chikatamarla, and Iliya V Karlin. Entropic lattice boltzmann model for compressible flows. *Physical Review E*, 92(6):061301, 2015.

[26] Nicolò Frapolli, Shyam S Chikatamarla, and Iliya V Karlin. Lattice kinetic theory in a comoving galilean reference frame. *Physical review letters*, 117(1):010604, 2016.

[27] Harold Grad. On the kinetic theory of rarefied gases. *Communications on pure and applied mathematics*, 2(4):331–407, 1949.

[28] Harold Grad. Principles of the kinetic theory of gases. In *Thermodynamik der Gase/Thermodynamics of Gases*, pages 205–294. Springer, 1958.

[29] Farzaneh Hajabdollahi and Kannan N Premnath. Symmetrized operator split schemes for force and source modeling in cascaded lattice boltzmann methods for flow and scalar transport. *Physical Review E*, 97(6):063303, 2018.

[30] Derek Hansen, Danielle C Maddix, Shima Alizadeh, Gaurav Gupta, and Michael W Mahoney. Learning physical models that can respect conservation laws. In *International Conference on Machine Learning*, pages 12469–12510. PMLR, 2023.

[31] Ami Harten. High resolution schemes for hyperbolic conservation laws. *Journal of computational physics*, 135(2):260–278, 1997.

[32] Xiaoyi He, Xiaowen Shan, and Gary D Doolen. Discrete boltzmann equation model for nonideal gases. *Physical Review E*, 57(1):R13, 1998.

[33] Kareem Hegazy, Michael W. Mahoney, and N. Benjamin Erichson. Powerformer: A transformer with weighted causal attention for time-series forecasting, 2025. URL <https://arxiv.org/abs/2502.06151>.

[34] Maximilian Herde, Bogdan Raonic, Tobias Rohner, Roger Käppeli, Roberto Molinaro, Emmanuel de Bezenac, and Siddhartha Mishra. Poseidon: Efficient foundation models for PDEs. In *The Thirty-eighth Annual Conference on Neural Information Processing Systems*, 2024.

[35] Helge Holden. *Splitting methods for partial differential equations with rough solutions: Analysis and MATLAB programs*, volume 11. European Mathematical Society, 2010.

[36] Shi Jin and Zhouping Xin. The relaxation schemes for systems of conservation laws in arbitrary space dimensions. *Communications on pure and applied mathematics*, 48(3):235–276, 1995.

[37] Ilya Karlin and Pietro Asinari. Factorization symmetry in the lattice boltzmann method. *Physica A: Statistical Mechanics and its Applications*, 389(8):1530–1548, 2010.

[38] IV Karlin, D Sichau, and SS Chikatamarla. Consistent two-population lattice boltzmann model for thermal flows. *Physical Review E*, 88(6):063310, 2013.

[39] Dmitrii Kochkov, Jamie A Smith, Ayya Alieva, Qing Wang, Michael P Brenner, and Stephan Hoyer. Machine learning–accelerated computational fluid dynamics. *Proceedings of the National Academy of Sciences*, 118(21):e2101784118, 2021.

[40] AM Kogan. Derivation of grad’s type equations and study of their relaxation properties by the method of maximization of entropy. *Journal of Applied Mathematics and Mechanics*, 29(1):130–142, 1965.

[41] Nikola Kovachki, Zongyi Li, Burigede Liu, Kamyar Azizzadenesheli, Kaushik Bhattacharya, Andrew Stuart, and Anima Anandkumar. Neural operator: Learning maps between function spaces with applications to pdes. *Journal of Machine Learning Research*, 24(89):1–97, 2023.

[42] Nikola Kovachki, Zongyi Li, Burigede Liu, Kamyar Azizzadenesheli, Kaushik Bhattacharya, Andrew Stuart, and Anima Anandkumar. Neural operator: Learning maps between function spaces with applications to pdes. *Journal of Machine Learning Research*, 24(89):1–97, 2023.

[43] Anastasis Kratsios, Takashi Furuya, Jose Antonio Lara Benitez, Matti Lassas, and Maarten de Hoop. Mixture of experts soften the curse of dimensionality in operator learning. *arXiv preprint arXiv:2404.09101*, 2024.

[44] Aditi Krishnapriyan, Amir Gholami, Shandian Zhe, Robert Kirby, and Michael W Mahoney. Characterizing possible failure modes in physics-informed neural networks. In *Advances in Neural Information Processing Systems*, volume 34, pages 26548–26560, 2021.

[45] Aditi S Krishnapriyan, Alejandro F Queiruga, N Benjamin Erichson, and Michael W Mahoney. Learning continuous models for continuous physics. *Communications Physics*, 6(1):319, 2023.

[46] Timm Krüger, Halim Kusumaatmaja, Alexandr Kuzmin, Orest Shardt, Goncalo Silva, and Erlend Magnus Viggen. The lattice boltzmann method. *Springer International Publishing*, 10(978-3):4–15, 2017.

[47] Jonas Latt, Christophe Coreixas, Joël Beny, and Andrea Parmigiani. Efficient supersonic flow simulations using lattice boltzmann methods based on numerical equilibria. *Philosophical Transactions of the Royal Society A*, 378(2175):20190559, 2020.

[48] Patrick Le Tallec and Jean-Philippe Perlat. *Numerical analysis of Levermore’s moment system*. PhD thesis, Inria, 1997.

[49] Vadim Levchenko, Andrey Zakirov, and Anastasia Perepelkina. Lrnla lattice boltzmann method: a performance comparison of implementations on gpu and cpu. In *International Conference on Parallel Computational Technologies*, pages 139–151. Springer, 2019.

[50] RJ LeVeque. Finite volume methods for hyperbolic problems, 2002.

[51] C David Levermore. Moment closure hierarchies for kinetic theories. *Journal of statistical Physics*, 83: 1021–1065, 1996.

[52] Zongyi Li, Nikola Borislavov Kovachki, Kamyar Azizzadenesheli, Burigede liu, Kaushik Bhattacharya, Andrew Stuart, and Anima Anandkumar. Fourier neural operator for parametric partial differential equations. In *International Conference on Learning Representations*, 2021.

[53] Phillip Lippe, Bas Veeling, Paris Perdikaris, Richard Turner, and Johannes Brandstetter. Pde-refiner: Achieving accurate long rollouts with neural pde solvers. *Advances in Neural Information Processing Systems*, 36:67398–67433, 2023.

[54] Yong Liu, Tengge Hu, Haoran Zhang, Haixu Wu, Shiyu Wang, Lintao Ma, and Mingsheng Long. itransformer: Inverted transformers are effective for time series forecasting, 2024. URL <https://arxiv.org/abs/2310.06625>.

[55] Lu Lu, Pengzhan Jin, Guofei Pang, Zhongqiang Zhang, and George Em Karniadakis. Learning nonlinear operators via deeponet based on the universal approximation theorem of operators. *Nature machine intelligence*, 3(3):218–229, 2021.

[56] Dongwei Lyu, Rie Nakata, Pu Ren, Michael W Mahoney, Arben Pitarka, Nori Nakata, and N Benjamin Erichson. Wavecastnet: An ai-enabled wavefield forecasting framework for earthquake early warning. *arXiv preprint arXiv:2405.20516*, 2024.

[57] Andrew Majda. *Compressible fluid flow and systems of conservation laws in several space variables*, volume 53. Springer Science & Business Media, 2012.

[58] Nick McGreivy and Ammar Hakim. Weak baselines and reporting biases lead to overoptimism in machine learning for fluid-related partial differential equations. *arXiv preprint arXiv:2407.07218*, 2024.

[59] Luc Mieussens. Discrete velocity model and implicit scheme for the bgk equation of rarefied gas dynamics. *Mathematical Models and Methods in Applied Sciences*, 10(08):1121–1149, 2000.

[60] Luc Mieussens. A survey of deterministic solvers for rarefied flows. In *AIP Conference Proceedings*, volume 1628, pages 943–951. American Institute of Physics, 2014.

[61] Sean T Miller, Nathan V Roberts, Stephen D Bond, and Eric C Cyr. Neural-network based collision operators for the boltzmann equation. *Journal of Computational Physics*, 470:111541, 2022.

[62] Yuqi Nie, Nam H Nguyen, Phanwadee Sinthong, and Jayant Kalagnanam. A time series is worth 64 words: Long-term forecasting with transformers. In *The Eleventh International Conference on Learning Representations*, 2023.

[63] Taku Ohwada. Higher order approximation methods for the boltzmann equation. *Journal of Computational Physics*, 139(1):1–14, 1998.

[64] Ravi G Patel, Indu Manickam, Nathaniel A Trask, Mitchell A Wood, Myoungkyu Lee, Ignacio Tomas, and Eric C Cyr. Thermodynamically consistent physics-informed neural networks for hyperbolic systems. *Journal of Computational Physics*, 449:110754, 2022.

[65] Vincent Pavan. General entropic approximations for canonical systems described by kinetic equations. *Journal of Statistical Physics*, 142:792–827, 2011.

[66] Beno^it Perthame. Global existence to the bgk model of boltzmann equation. *Journal of Differential equations*, 82(1):191–205, 1989.

[67] Nikolaos I Prasianakis and Ilya V Karlin. Lattice boltzmann method for thermal flow simulation on standard lattices. *Physical Review E—Statistical, Nonlinear, and Soft Matter Physics*, 76(1):016702, 2007.

[68] Pu Ren, Rie Nakata, Maxime Lacour, Ilan Naiman, Nori Nakata, Jialin Song, Zhengfa Bi, Osman Asif Malik, Dmitriy Morozov, Omri Azencot, N. Benjamin Erichson, and Michael W. Mahoney. Learning physics for unveiling hidden earthquake ground motions via conditional generative modeling, 2024. URL <https://arxiv.org/abs/2407.15089>.

[69] Mohammad Hossein Saadat, Fabian Bösch, and Ilya V Karlin. Lattice boltzmann model for compressible flows on standard lattices: Variable prandtl number and adiabatic exponent. *Physical Review E*, 99(1):013306, 2019.

[70] M. Sakarvadia, K. Hegazy, A. Totounferoush, K. Chard, Y. Yang, I. Foster, and M. W. Mahoney. The false promise of zero-shot super-resolution in machine-learned operators. Technical Report Preprint: arXiv:2510.06646, 2025.

[71] Ulf D Schiller. A unified operator splitting approach for multi-scale fluid-particle coupling in the lattice boltzmann method. *Computer Physics Communications*, 185(10):2586–2597, 2014.

[72] Xiaowen Shan. Central-moment-based galilean-invariant multiple-relaxation-time collision model. *Physical Review E*, 100(4):043308, 2019.

[73] Xiaowen Shan and Xiaoyi He. Discretization of the velocity space in the solution of the boltzmann equation. *Physical Review Letters*, 80(1):65, 1998.

[74] Gary A Sod. A survey of several finite difference methods for systems of nonlinear hyperbolic conservation laws. *Journal of computational physics*, 27(1):1–31, 1978.

[75] Gilbert Strang. On the construction and comparison of difference schemes. *SIAM journal on numerical analysis*, 5(3):506–517, 1968.

[76] Shashank Subramanian, Peter Harrington, Kurt Keutzer, Wahid Bhimji, Dmitriy Morozov, Michael W Mahoney, and Amir Gholami. Towards foundation models for scientific machine learning: Characterizing scaling and transfer behavior. In *Advances in Neural Information Processing Systems*, volume 36, pages 71242–71262, 2023.

[77] Sauro Succi and S Succi. *The lattice Boltzmann equation: for complex states of flowing matter*. Oxford university press, 2018.

[78] Karthik Thyagarajan, Christophe Coreixas, and Jonas Latt. Exponential distribution functions for positivity-preserving lattice boltzmann schemes: Application to 2d compressible flow simulations. *Physics of Fluids*, 35(12), 2023.

[79] Eleuterio F Toro. *Riemann solvers and numerical methods for fluid dynamics: a practical introduction*. Springer Science & Business Media, 2013.

[80] Si Bui Quang Tran, Fong Yew Leong, Quang Tuyen Le, and Duc Vinh Le. Lattice boltzmann method for high reynolds number compressible flow. *Computers & Fluids*, 249:105701, 2022.

[81] Cédric Villani. A review of mathematical topics in collisional kinetic theory. *Handbook of mathematical fluid dynamics*, 1:71–74, 2002.

[82] Ricardo Vinuesa and Steven L Brunton. Enhancing computational fluid dynamics with machine learning. *Nature Computational Science*, 2(6):358–366, 2022.

[83] W Waluś. Computational methods for the boltzmann equation. *Lecture Notes on the Mathematical Theory of the Boltzmann equation*, N. Bellomo (ed.), World Sci., Singapore, pages 179–223, 1995.

[84] Haixu Wu, Jiehui Xu, Jianmin Wang, and Mingsheng Long. Autoformer: Decomposition transformers with auto-correlation for long-term series forecasting. In A. Beygelzimer, Y. Dauphin, P. Liang, and J. Wortman Vaughan, editors, *Advances in Neural Information Processing Systems*, 2021.

[85] Tianbai Xiao and Martin Frank. Using neural networks to accelerate the solution of the boltzmann equation. *Journal of Computational Physics*, 443:110521, 2021.

[86] Tianbai Xiao and Martin Frank. Relaxnet: A structure-preserving neural network to approximate the boltzmann collision operator. *Journal of Computational Physics*, 490:112317, 2023.

[87] Jingfeng Zhang, Bo Han, Laura Wynter, Kian Hsiang Low, and Mohan Kankanhalli. Towards robust resnet: A small step but a giant leap. *arXiv preprint arXiv:1902.10887*, 2019.

[88] Tian Zhou, Ziqing Ma, Qingsong Wen, Xue Wang, Liang Sun, and Rong Jin. FEDformer: Frequency enhanced decomposed transformer for long-term series forecasting. In *Proceedings of the 39th International Conference on Machine Learning*, volume 162 of *Proceedings of Machine Learning Research*, pages 27268–27286. PMLR, 17–23 Jul 2022.

# Supporting Information for “Neural equilibria for long-term prediction of nonlinear conservation laws”

## Contents

<b>1</b>	<b>Introduction</b>	<b>1</b>
<b>2</b>	<b>Results</b>	<b>3</b>
2.1	Lattice Boltzmann Framework	3
2.2	NeurDE and LB+NeurDE	5
2.3	Empirical Evaluation	7
2.3.1	1D Riemann’s Problem: Sod Shock Tube	7
2.3.2	2D Supersonic Flow	7
2.4	Performance at Long Times and Unseen Conditions	9
2.4.1	Sod Shock Tube	9
2.4.2	Supersonic Flow Around a Cylinder	11
<b>3</b>	<b>Discussion</b>	<b>11</b>
<b>4</b>	<b>Methods</b>	<b>12</b>
4.1	Constructing the Neural Moment Space	12
4.2	Realization in Compressible Fluid Dynamics	12
4.3	Hybrid Closure and Training	13
4.4	Experimental Configurations	13
4.4.1	Subsonic Baseline	13
4.4.2	Transonic Baseline	14
4.4.3	2D Supersonic Interaction	14
<b>A</b>	<b>Notation Glossary</b>	<b>22</b>
<b>B</b>	<b>Preliminaries</b>	<b>23</b>
B.1	The Boltzmann Transport Equation	23
B.2	Maxwellian Distribution—Equilibrium	24
B.3	BGK Collision	25
B.4	Discrete Velocities and Discrete Kinetic Equations	25
B.5	Moment System of the Boltzmann Equation	26
B.6	Structure of the Moment Space	26
B.7	Higher-order moments of the Maxwell-Boltzmann distribution	27
B.8	A splitting Method for Eq. (4)	27
B.9	Lattice Boltzmann Scheme	27
B.10	Closure Relations in Lattice Velocities	28
<b>C</b>	<b>NeurDE General Setting and Training Algorithm</b>	<b>29</b>
C.1	Operator Structure	29
C.2	General Formulation and Interpretation	29
C.3	Streaming as a Convolutional Neural Network	30
C.4	LB+NeurDE as an Architecture	31
C.5	Training Scheme	32
C.5.1	Pretraining Procedure	33
C.5.2	Training Algorithm	33

<b>D Empirical Evaluation</b>	<b>35</b>
D.1 Two-Population Thermal LB Scheme . . . . .	35
D.1.1 Polynomial Equilibrium for the $f$ Population . . . . .	35
D.1.2 Polynomial Equilibrium for the $g$ Population . . . . .	36
D.2 Datasets . . . . .	36
D.3 Architecture Parameters . . . . .	36
D.4 Optimization Algorithm . . . . .	37
D.5 Training and Computational Setup . . . . .	37
<b>E Shock Tube</b>	<b>38</b>
E.1 Subsonic Shock Tube Case (from Subsec. 2.3.1) . . . . .	38
E.1.1 Subsonic Nature of the Experiment . . . . .	38
E.1.2 Model Failure (from Subsec. 2.4.1) . . . . .	39
E.1.3 FNO Benchmark . . . . .	39
E.2 Transonic Shock Tube Case (from Subsec. 2.3.1) . . . . .	43
E.2.1 Training with Regularization by the Total Variation Diminishing Principle . . . . .	44
E.2.2 Total Variation Diminishing Principle . . . . .	44
E.2.3 Adding the TVD in the Training Algorithm . . . . .	45
E.2.4 Local Mach Number Transonic Case . . . . .	45
E.2.5 Errors of the Polynomial for the Transonic Case . . . . .	46
E.2.6 Model Failure (cf. Subsec. 2.4.1) . . . . .	46
<b>F Ablation Study: Surrogate Models for Collision and Streaming</b>	<b>48</b>
F.1 Surrogate Model for Collision ( $\Phi_e$ ) . . . . .	48
F.1.1 Enforcing Symmetry and Conservation as in Corbetta et al. [18] . . . . .	48
F.1.2 Training Details . . . . .	49
F.1.3 Comparison of Results between LB+NeurDE and the $MLP_{\text{cons}}^{\text{sym}+}$ Surrogate . . . . .	49
F.1.4 Without Algebraic Correction . . . . .	50
F.2 Surrogate Model for $\Phi_g$ . . . . .	50
F.2.1 Temporal Streaming through <i>ContinuousNet</i> . . . . .	51
F.2.2 Training Details . . . . .	52
F.2.3 Numerical Results . . . . .	52
<b>G 2D Supersonic Flow</b>	<b>53</b>
G.1 Prediction Results for Training on the First 500 Time-Steps . . . . .	53
G.2 Results for Long-Term Predictions . . . . .	56

## A Notation Glossary

A summary of the notation used in this paper is presented in Table 1.

Notation	Description	Reference
$\Omega, d$	Spatial domain and number of components of spatial domain $\Omega \subset \mathbb{R}^d$	
$f^{\text{MB}}$	Maxwellian distribution	Eq. (22)
$f^{\text{eq}} \text{ or } \mathbf{f}_i^{\text{eq}}$	Equilibrium distribution of $f$ or $\mathbf{f}_i$	
$\mathcal{C}(\cdot)$	Boltzmann collision operator	Eq. (12)
$\otimes, \otimes^{\text{sym}}$	Tensor product and symmetric tensor product	
<b>Discrete velocity model and LB</b>		
$\Omega_{\{\mathbf{f}_i, \mathbf{g}_i\}}$	BGK-type collision operator	Eq. (8)
$\mathbf{U} = (\rho, \mathbf{u}, E)^\top$	Macroscopic observables (density, fluid-velocity, temperature)	Eq. (9)
$\mathbf{q}^{\text{MB}}, \mathbf{P}^{\text{MB}}, \mathbf{R}^{\text{MB}}$	Maxwellian higher-order moments	Eq. (32)
$\mathbf{q}^{\text{eq}}, \mathbf{P}^{\text{eq}}, \mathbf{R}^{\text{eq}}$	Equilibrium higher-order moments	Subsec. D.1
$\{\mathbf{v}_i\}_{i=1}^Q$	Discrete velocities	Eq. (4)
$\{\mathbf{c}_i\}_{i=1}^Q$	Lattice velocities	Eq. (5)
$\{\mathbf{f}_i, \mathbf{g}_i\}$	Discrete velocity populations; $(t, \mathbf{x}, \mathbf{c}_i) \in \mathbb{R}_{\geq 0}^d \times \Omega \times \{\mathbf{v}_i\}_{i=1}^Q$	Eq. (4)
$\{W_i\}_{i=1}^Q$	Temperature related weights	Subsec. D.1
$\mathbf{g}_i^*$	Quasi-equilibrium	Eq. (50)
$\tau_1, \tau_2$	Relaxation related viscosity and thermal conductivity	Eq. (8)
<b>Splitting algorithm</b>		
$\Phi_C$	Solution operator of the collision problem	Eq. (5a)
$\Phi_S$	Solution operator of the streaming (free flow)	Eq. (5b)
$\Phi_S \Phi_C$	LB algorithm	Eq. (5)
<b>Surrogate model for the equilibrium</b>		
$\boldsymbol{\lambda}, \boldsymbol{\varphi}$	Neural networks	Eq. (6)
$\phi_i^{\text{NN}}(\cdot)$	Surrogate model for the equilibrium NeurDE $\phi_i^{\text{NN}}(\cdot) = \exp(\boldsymbol{\lambda} \cdot \boldsymbol{\varphi})(\mathbf{c}_i)$	Eq. (6)
$\Phi_C^{\text{NN}}$	Hybrid solution of the BGK-type collision with ML surrogate	Eq. (40)
$\mathbb{M}$	Moment space (span of $\boldsymbol{\varphi}$ )	Eq. (7)
$\Phi_S \Phi_C^{\text{NN}}$	Hybrid model LB+NeurDE	Fig. 2
$\mathcal{D}$	Operator mapping distributions to observables	Eq. (39)
<b>Experiments</b>		
$p = R\rho T$	Pressure calculated by the ideal gas law	
$\text{Ma}$	Local Mach number; $\text{Ma} = (\mathbf{u} \cdot \mathbf{u})^{1/2}(\gamma RT)^{-1/2}$	Subsec. 2.3.2
$\gamma$	Specific heat ratio	Subsec. 4.2
$\text{TV}(\cdot)$	Total variational principle	Eq. (57)
$\text{Re}$	Reynolds number	
$\text{Ma}_\infty$	Far-field Mach number	Subsec. 2.3.2
$\mathbf{u}_\infty$	Far-field (flow) velocity	Subsec. 2.3.2

**Table 1: Glossary of mathematical notation.** Symbols are organized by topic: kinetic theory and lattice Boltzmann fundamentals, numerical algorithms and splitting schemes, neural network surrogate models, and experimental parameters.

## B Preliminaries

This appendix provides supplementary details on the kinetic theory background introduced in the main text (Subsec. 2.1). We elaborate on the Boltzmann transport equation, discrete kinetic models, and the lattice Boltzmann (LB) formulation, which together form the foundation of our LB+NeurDE method.

The material is organized as follows. Subsec. B.1 summarizes the structure of the general Boltzmann collision operator. Subsec. B.2 defines the Maxwellian equilibrium distribution (introduced in Subsec. 2.1) in terms of its variational characterization as the entropy maximizer subject to conservation constraints. Once this abstract equilibrium is established, we introduce in Subsec. B.3 the BGK relaxation model as a practical surrogate for the general collision operator. Subsec. B.4 then discusses the discretization of the velocity space, leading to the so-called discrete velocity models for the Boltzmann equation. Subsec. B.5 explains how the Boltzmann equation yields local conservation laws and, through constitutive relations, leads to macroscopic fluid dynamics. Subsec. B.6 reviews classical moment closure hierarchies following Grad [27] and their systematic extension by Levermore [51]. Subsec. B.7 provides explicit expressions for higher-order moments of the Maxwell–Boltzmann distribution. Subsec. B.8 outlines the operator splitting technique used in the LBM; and Subsec. B.9 summarizes the fundamental principles of LBM. Finally, Subsec. B.10 discusses closure (aliasing) errors introduced by discrete velocity sets, a key challenge in LB formulations also noted in the main text (see below Eq. (7)).

### B.1 The Boltzmann Transport Equation

Here, we provide an overview of classical kinetic theory. We consider the Boltzmann transport equation, see [51, 11, 63] for references. Its dimensionless form is given by:

$$(\partial_t + \mathbf{v} \cdot \nabla_{\mathbf{x}}) f(t, \mathbf{x}, \mathbf{v}) = \frac{1}{\varepsilon} \mathcal{C}(f), \quad t > 0, (\mathbf{x}, \mathbf{v}) \in \Omega \times \mathbb{R}^d, \quad (12)$$

where  $f(t, \mathbf{x}, \mathbf{v})$  represents a probability density distribution function, modeling the probability of finding a (gas) particle at time  $t$ , with position  $\mathbf{x} \in \Omega$ , and velocity  $\mathbf{v} \in \mathbb{R}^d$ . The parameter  $\varepsilon$  is the Knudsen number, defined as the ratio of the mean free path over the length scale, which characterizes the degree of rarefaction of the gas. The collision operator is a quadratic integral operator over  $\mathbf{v}$ , whose domain  $\mathcal{D}(\mathcal{C})$  is contained in the cone of nonnegative functions  $f$ .

**Characterization of the Collision Operator.** The collision operator  $\mathcal{C}$  satisfies three properties, that relate with conservation laws, local dissipation, and symmetries. We recall from Subsec. 2.1 that we use the symbol  $\langle \cdot \rangle$  to represent integration over the velocity space; namely,  $\langle \psi(f) \rangle = \int_{\mathbb{R}^d} \psi(f) d\mathbf{v}$ . Let us briefly review these properties.

1. In the collision process, *mass, momentum, and energy are conserved*, i.e., for any distribution  $f$ , we have:

$$\left\langle \left( 1, \mathbf{v}, \frac{1}{2} \mathbf{v} \cdot \mathbf{v} \right)^\top \mathcal{C}(f) \right\rangle = (0, 0, 0)^\top, \quad \text{for every } f \in \mathcal{D}(\mathcal{C}). \quad (13)$$

Here,  $\rho = \langle f \rangle$  is the density,  $\rho \mathbf{u} = \langle \mathbf{v} f \rangle$  is the momentum, and  $\rho E = \langle \mathbf{v} \cdot \mathbf{v} f \rangle / 2$  is the energy density, with  $E$  as the total energy.

Consequently, as a result of Eq. (13), solutions  $f$  to the Boltzmann transport equation Eq. (12) satisfy (local) conservation laws. See Subsec. B.5 for the local conservation laws related to the solution of Eq. (12).

Furthermore,  $\langle \varphi(\mathbf{v}) \mathcal{C}(f) \rangle = 0$ , for all  $f \in \mathcal{D}(\mathcal{C})$  if, and only if,  $\varphi(\mathbf{v})$  belongs to  $\text{span}\{1, \mathbf{v}, \mathbf{v} \cdot \mathbf{v}\}$ . This implies that there are no additional conservation laws beyond those given in Eq. (13).

2. The collision,  $\mathcal{C}$ , satisfies the *local dissipation*

$$\langle \log f \mathcal{C}(f) \rangle \leq 0, \quad f \in \mathcal{D}(\mathcal{C}), \quad (14)$$

which implies Boltzmann's H-theorem,

$$\partial_t \langle f(\log f - 1) \rangle + \nabla_{\mathbf{x}} \cdot \langle \mathbf{v} f(\log f - 1) \rangle = \langle \log f \mathcal{C}(f) \rangle \leq 0, \quad (15)$$

where  $\langle f(\log f - 1) \rangle$  is the local entropy function, and  $\langle \mathbf{v} f(\log f - 1) \rangle$  the local entropy flux.

The total entropy is defined as

$$s = \int_{\Omega} \langle f(\log f - 1) \rangle d\mathbf{v},$$

and we then obtain the entropy inequality [48],

$$\partial_t s + \int_{\partial\Omega} \langle \mathbf{v} f(\log f - 1) \rangle \cdot \nu d\sigma(\mathbf{x}) \leq 0.$$

Eq. (14) vanishes only at the local equilibrium (see Subsec. B.2).

3. The collision operator commutes with *translation and orthogonal transformation*. Let  $\mathbf{v}' \in \mathbb{R}^d$ , and  $\mathbf{Q} \in \mathbb{R}^{D \times D}$  be an orthogonal matrix. Define  $L_{\mathbf{v}'} f(\mathbf{v}) = f(\mathbf{v} - \mathbf{v}')$  and  $L_{\mathbf{Q}} f(\mathbf{v}) = f(\mathbf{Q}^T \mathbf{v})$ . Then,

$$L_{\mathbf{v}'} \mathcal{C}(f) = \mathcal{C}(L_{\mathbf{v}'} f), \quad L_{\mathbf{Q}} \mathcal{C}(f) = \mathcal{C}(L_{\mathbf{Q}} f). \quad (16)$$

If  $\Omega = \mathbb{R}^d$ , then Eq. (16) implies the Galilean invariance.

This means that solutions  $f$  of Eq. (12) are invariant under space and time translation. Precisely, for any  $f$  satisfying Eq. (12),  $\mathbf{v}' \in \mathbb{R}^d$  and  $\mathbf{Q} \in \mathbb{R}^d \times \mathbb{R}^d$ , we have

$$\mathcal{A}_{\mathbf{v}'} f = f(t, \mathbf{x} - \mathbf{v}' t, \mathbf{v} - \mathbf{v}') \quad (17)$$

$$\mathcal{A}_{\mathbf{Q}} f = f(t, \mathbf{Q}^T t, \mathbf{Q}^T \mathbf{v}). \quad (18)$$

## B.2 Maxwellian Distribution—Equilibrium

The equilibrium distribution  $f^{\text{eq}}$  (also known as Maxwellian) is defined as the kernel (null space) of the collision operator  $\mathcal{C}$ , i.e., the state for which collisions are in detailed balance,

$$\mathcal{C}(f^{\text{eq}}) = 0.$$

Boltzmann's H-theorem links this kinetic notion of equilibrium to thermodynamics. Let the kinetic entropy (H-function) be

$$H(f) = \langle f \log f \rangle, \quad (19)$$

where  $\langle \cdot \rangle$  denotes integration over velocity space. The H-theorem states that  $H(f)$  is a Lyapunov functional for the collisional dynamics:

$$\frac{d}{dt} H(f) = \langle \log f \mathcal{C}(f) \rangle \leq 0,$$

with equality if and only if  $f$  is an equilibrium distribution (under the usual regularity and decay hypotheses) [13, 81]. Hence the collision operator's null space coincides with the set of entropy-critical states.

Equivalently, the local Maxwellian  $f^{\text{eq}}$  may be characterized *variationally* as the unique minimizer of  $H(f)$  subject to conservation of the collision invariants (mass, momentum, energy):

$$\langle (1, \mathbf{v}, \frac{1}{2}|\mathbf{v}|^2) f \rangle^T = (\rho, \rho \mathbf{u}, \rho E)^T. \quad (20)$$

Thus

$$f^{\text{eq}} = \arg \min_{f \geq 0} \{H(f) : \text{Eq. (20) holds}\}, \quad (21)$$

and solving this constrained minimization yields the classical Maxwell–Boltzmann form under standard hypotheses [66, 51]:

$$f^{\text{MB}}(t, \mathbf{x}, \mathbf{v}) = \frac{\rho(t, \mathbf{x})}{(2\pi R T(t, \mathbf{x}))^{d/2}} \exp \left( -\frac{(\mathbf{v} - \mathbf{u}(t, \mathbf{x})) \cdot (\mathbf{v} - \mathbf{u}(t, \mathbf{x}))}{2R T(t, \mathbf{x})} \right), \quad (22)$$

where  $R$  is the gas constant and  $d$  is the spatial dimension [66, 51].

The variational and dynamical characterizations are therefore consistent: the entropy minimizer subject to the collision-invariant constraints is exactly the null state of the collision operator (see [13, 81, 51] for rigorous statements and hypotheses).

**Discrete Velocities and Discrete Equilibrium.** In lattice Boltzmann and other discrete-velocity methods (see Subsec. B.4), the velocity space is replaced by a finite set  $\{\mathbf{v}_i\}_{i=1}^Q$  with an associated discrete measure. Sampling the continuous Maxwellian at these nodes,  $f^{\text{MB}}(\mathbf{v}_i)$ , does *not* generally produce the true minimizer of the discrete entropy under the discrete moment constraints. The discrete equilibrium must instead be obtained by solving the corresponding constrained minimization problem on the discrete velocity set, or by solving a nonlinear system enforcing moment consistency [66, 59]. This procedure is accurate but computationally expensive when performed at every space–time point. In this work, we replaced this inversion with a learned surrogate  $\phi^{\text{NN}} : \mathbf{U} \mapsto \mathbf{f}^{\text{eq}}$ , which approximates the discrete entropy minimizer with high fidelity and negligible runtime cost.

### B.3 BGK Collision

A widely used surrogate for the full Boltzmann collision operator is the Bhatnagar–Gross–Krook (BGK) relaxation model [7]. It replaces the nonlinear collision integral with a simple relaxation toward the equilibrium distribution  $f^{\text{eq}}$  over a characteristic time scale  $\tau$ :

$$\mathcal{C}(f) = \frac{1}{\tau} (f^{\text{eq}} - f). \quad (23)$$

The BGK operator preserves the fundamental conservation laws of mass, momentum, and energy, since the Maxwellian Eq. (22) satisfies

$$\langle f^{\text{eq}} \rangle = \langle f \rangle, \quad \langle \mathbf{v} f^{\text{eq}} \rangle = \langle \mathbf{v} f \rangle, \quad \langle \frac{1}{2} \mathbf{v} \cdot \mathbf{v} f^{\text{eq}} \rangle = \langle \frac{1}{2} \mathbf{v} \cdot \mathbf{v} f \rangle, \quad (24)$$

where  $\langle \cdot \rangle$  denotes integration over velocity space.

Moreover, the BGK model enforces local entropy dissipation. Using the entropy functional  $H[f] = \langle f \log f \rangle$ , one obtains

$$\begin{aligned} \langle \log f \tau^{-1} (f^{\text{eq}} - f) \rangle &= \tau^{-1} \langle \log \frac{f}{f^{\text{eq}}} (f^{\text{eq}} - f) \rangle + \tau^{-1} \langle \log f^{\text{eq}} (f^{\text{eq}} - f) \rangle \\ &= \tau^{-1} \langle \log \frac{f}{f^{\text{eq}}} (f^{\text{eq}} - f) \rangle = \tau^{-1} \langle \log \frac{f}{f^{\text{eq}}} (1 - \frac{f}{f^{\text{eq}}}) f^{\text{eq}} \rangle \leq 0, \end{aligned}$$

since  $\log(x)(1 - x) \leq 0$  for  $x > 0$ . This guarantees compliance with the  $H$ -theorem, and it ensures that  $f$  relaxes monotonically toward equilibrium.

The BGK model thus provides a minimal yet physically consistent closure that retains the essential conservation and dissipation structure of the full Boltzmann collision operator, while being far simpler to evaluate.

### B.4 Discrete Velocities and Discrete Kinetic Equations

To obtain a tractable kinetic scheme, the continuous velocity space is replaced by a finite set of discrete velocities  $\mathcal{V} \subset \mathbb{R}^d$ . This amounts to approximating integrals in the Boltzmann or Boltzmann–BGK equation by a finite quadrature rule. Concretely, we introduce a discrete measure

$$\mathcal{V} = \{\mathbf{v}_i\}_{i=1}^Q \subset \mathbb{R}^d, \quad d\mu(\mathbf{v}) = \sum_{i=1}^Q W_i \delta(\mathbf{v} - \mathbf{v}_i), \quad (25)$$

so that velocity integrals are approximated by

$$\int_{\mathbb{R}^d} \psi(\mathbf{v}) d\mathbf{v} \approx \sum_{i=1}^Q W_i \psi(\mathbf{v}_i),$$

where  $\{W_i\}_{i=1}^Q$  are quadrature weights.

The choice of  $\mathcal{V}$  and  $W_i$  determines the accuracy with which velocity moments are reproduced and is central to the stability of the discrete kinetic scheme. Classical constructions rely on Gauss–Hermite quadrature or related cubature rules, which ensure exactness up to a prescribed polynomial degree [73]. This discretization converts the continuous kinetic equation into a system of  $Q$  coupled transport–relaxation equation—as we have seen in Eq. (4)—one for each discrete velocity.

## B.5 Moment System of the Boltzmann Equation

Starting from the Boltzmann transport equation Eq. (12), we obtain macroscopic conservation laws by multiplying by collision invariants  $\varphi(\mathbf{v}) \in \text{span}\{1, \mathbf{v}, \mathbf{v} \cdot \mathbf{v}\}$  and integrating over velocity space. Using the local conservation property of the collision operator (Eq. (13)), we arrive at

$$\partial_t \langle \varphi(\mathbf{v}) f \rangle + \nabla_{\mathbf{x}} \cdot \langle \mathbf{v} \otimes^{\text{sym}} \varphi(\mathbf{v}) f \rangle = 0, \quad (26)$$

where  $\otimes^{\text{sym}}$  denotes the symmetric tensor product.

Choosing  $\varphi(\mathbf{v}) = 1, \mathbf{v}$ , and  $\frac{1}{2}\mathbf{v} \cdot \mathbf{v}$  yields the balance laws for mass, momentum, and energy:

$$\partial_t \langle f \rangle + \nabla_{\mathbf{x}} \cdot \langle \mathbf{v} f \rangle = 0, \quad (27a)$$

$$\partial_t \langle \mathbf{v} f \rangle + \nabla_{\mathbf{x}} \cdot \langle \mathbf{v} \otimes^{\text{sym}} \mathbf{v} f \rangle = 0, \quad (27b)$$

$$\partial_t \langle \frac{1}{2}\mathbf{v} \cdot \mathbf{v} f \rangle + \nabla_{\mathbf{x}} \cdot \langle \frac{1}{2}(\mathbf{v} \cdot \mathbf{v}) \mathbf{v} f \rangle = 0. \quad (27c)$$

Identifying the macroscopic observables

$$\langle f \rangle = \rho, \quad \langle \mathbf{v} f \rangle = \rho \mathbf{u}, \quad \langle \frac{1}{2}\mathbf{v} \cdot \mathbf{v} f \rangle = E = \frac{1}{2}\rho|\mathbf{u}|^2 + \frac{d}{2}\rho T,$$

and introducing the flux decompositions

$$\langle \mathbf{v} \otimes^{\text{sym}} \mathbf{v} f \rangle = \rho \mathbf{u} \otimes^{\text{sym}} \mathbf{u} + \mathbf{P}, \quad (28a)$$

$$\langle \frac{1}{2}(\mathbf{v} \cdot \mathbf{v}) \mathbf{v} f \rangle = E \mathbf{u} + \mathbf{P} \mathbf{u} + \mathbf{Q}, \quad (28b)$$

the moment equations can be written compactly as

$$\partial_t \begin{pmatrix} \rho \\ \rho \mathbf{u} \\ E \end{pmatrix} + \nabla_{\mathbf{x}} \cdot \begin{pmatrix} \rho \mathbf{u} \\ \rho \mathbf{u} \otimes^{\text{sym}} \mathbf{u} + \mathbf{P} \\ E \mathbf{u} + \mathbf{P} \mathbf{u} + \mathbf{Q} \end{pmatrix} = \begin{pmatrix} 0 \\ 0 \\ 0 \end{pmatrix}, \quad (29)$$

where  $\mathbf{P} = \langle (\mathbf{v} - \mathbf{u}) \otimes^{\text{sym}} (\mathbf{v} - \mathbf{u}) f \rangle$  and  $\mathbf{Q} = \frac{1}{2}\langle (\mathbf{v} - \mathbf{u})|\mathbf{v} - \mathbf{u}|^2 f \rangle$  are the stress tensor and heat flux, respectively. We may further decompose

$$\mathbf{P} = \rho T \mathbf{I} + \boldsymbol{\Sigma}, \quad (30a)$$

$$\mathbf{Q} = \rho T \mathbf{u} + \boldsymbol{\Sigma} \mathbf{u} + \mathbf{q}, \quad (30b)$$

where  $\boldsymbol{\Sigma}$  is the deviatoric stress tensor and  $\mathbf{q}$  the heat flux vector.

*Remark B.1* (Hydrodynamic Closures). To close Eq. (29), constitutive relations must be specified for  $\boldsymbol{\Sigma}$  and  $\mathbf{q}$ .

- For  $\boldsymbol{\Sigma} = 0$  and  $\mathbf{q} = 0$ , with  $p = \rho RT$ , the system reduces to the *compressible Euler equations*.
- For Newtonian viscous stress  $\mathbf{P} = (p - \zeta \nabla \cdot \mathbf{u}) \mathbf{I} - \mu(\nabla \mathbf{u} + \nabla \mathbf{u}^\top - \frac{2}{d}(\nabla \cdot \mathbf{u}) \mathbf{I})$  and Fourier heat flux  $\mathbf{q} = -\kappa \nabla T$ , one recovers the *Navier–Stokes–Fourier equations*, where  $\mu$ ,  $\zeta$ , and  $\kappa$  denote dynamic viscosity, bulk viscosity, and thermal conductivity, respectively.

## B.6 Structure of the Moment Space

Let  $\mathbb{M}$  be a finite-dimensional linear space of functions of  $\mathbf{v}$  (often polynomial). Taking the moments of Eq. (12) with respect to  $\mathbf{m}(\mathbf{v}) \in \mathbb{M}$  yields

$$\partial_t \langle \mathbf{m}(\mathbf{v}) f \rangle + \nabla_{\mathbf{x}} \cdot \langle \mathbf{v} \otimes^{\text{sym}} \mathbf{m}(\mathbf{v}) f \rangle = 0. \quad (31)$$

Eq. (26) is recovered by taking  $\mathbb{M} = \text{span}\{1, \mathbf{v}, \mathbf{v} \cdot \mathbf{v}\}$ .

The *moment closure problem* consists of expressing the flux terms in Eq. (31) in terms of finitely many moments determined by  $\mathbb{M}$ . When  $\mathbf{v}$  is discretized,  $\{\mathbf{v}_i\}_{i=1}^Q$ , common choices for  $\mathbb{M}$  include:

1. Degree  $\leq 2$ : *Eulerian basis*  $\mathbb{M} = \text{span}\{1, \mathbf{v}_i, \mathbf{v}_i \cdot \mathbf{v}_i\}$ , or *Gaussian basis*  $\mathbb{M} = \text{span}\{1, \mathbf{v}_i, \mathbf{v}_i \otimes^{\text{sym}} \mathbf{v}_i\}$ .
2. Degree  $\leq 4$ : *Grad basis* [27]:  $\mathbb{M} = \text{span}\{1, \mathbf{v}_i, \mathbf{v}_i \otimes^{\text{sym}} \mathbf{v}_i, (\mathbf{v}_i \cdot \mathbf{v}_i)\mathbf{v}_i\}$ , and *Levermore basis* [51]:  $\mathbb{M} = \text{span}\{1, \mathbf{v}_i, \mathbf{v}_i \otimes^{\text{sym}} \mathbf{v}_i, (\mathbf{v}_i \cdot \mathbf{v}_i)\mathbf{v}_i, (\mathbf{v}_i \cdot \mathbf{v}_i)^2\}$ .
3. Higher-order closures: tensorial bases involving cubic and quartic combinations of  $\mathbf{v}_i$ , e.g.,

$$\text{span}\{1, \mathbf{v}_i, \mathbf{v}_i^{\otimes 2}, \mathbf{v}_i^{\otimes 3}, \mathbf{v}_i^{\otimes 4}\}.$$

These moment spaces form the foundation for classical closure hierarchies such as Grad's and Levermore's, and they underpin modern discrete kinetic methods and entropic closures.

## B.7 Higher-order moments of the Maxwell-Boltzmann distribution

Some of the most commonly used higher-order moments of the Maxwellian Eq. (22) include the pressure tensor Eq. (32a), the heat flux vector Eq. (32b), and the contracted fourth-order tensor Eq. (32c). These moments are defined as follows:

$$\mathbf{P}_{\alpha,\beta}^{\text{MB}} = \rho \mathbf{u}_\alpha \mathbf{u}_\beta + \rho T \delta_{\alpha,\beta}, \quad (32a)$$

$$\mathbf{q}_\alpha^{\text{MB}} = 2\rho \mathbf{u}_\alpha (E + T), \quad (32b)$$

$$\mathbf{R}_{\alpha,\beta}^{\text{MB}} = 2\rho E (T \delta_{\alpha,\beta} + \mathbf{u}_\alpha \mathbf{u}_\beta) + 2\rho T (T \delta_{\alpha,\beta} + 2\mathbf{u}_\alpha \mathbf{u}_\beta). \quad (32c)$$

## B.8 A splitting Method for Eq. (4)

Here, we review the splitting approach for approximately solving kinetic equations. For a comprehensive introduction to splitting methods, see [35, 75]. Rewriting Eq. (4) as

$$\partial_t \mathbf{f}_i(t, \mathbf{x}) = \underbrace{-\mathbf{v}_i \cdot \nabla \mathbf{f}_i(t, \mathbf{x})}_{\mathcal{S}} + \underbrace{\frac{1}{\tau} (\mathbf{f}_i^{\text{eq}}(\mathbf{U}(t, \mathbf{x})) - \mathbf{f}_i(t, \mathbf{x}))}_{\mathcal{C}},$$

exposes a nonlinear collision and a linear transport (free-flow) parts of evolution. The splitting scheme can be represented by means of the following steps

$$\partial_t \tilde{\mathbf{f}}_i(t, \mathbf{x}) = \frac{1}{\tau} (\mathbf{f}_i^{\text{eq}}(\mathbf{U}(t, \mathbf{x})) - \tilde{\mathbf{f}}_i(t, \mathbf{x})), \quad \tilde{\mathbf{f}}_i(0, \mathbf{x}) = \mathbf{f}_i(0, \mathbf{x}) \quad (33a)$$

$$\partial_t \bar{\mathbf{f}}_i(t, \mathbf{x}) = -\mathbf{v}_i \cdot \nabla \bar{\mathbf{f}}_i(t, \mathbf{x}), \quad \bar{\mathbf{f}}_i(0, \mathbf{x}) = \tilde{\mathbf{f}}_i(\Delta t, \mathbf{x}), \quad (33b)$$

where  $\mathbf{f}(0, \mathbf{x})$  is the initial condition. Denoting the solutions operators to the collision subproblem (Eq. (33a)) by  $\Phi_{\mathcal{C}}$  and the streaming subproblem (Eq. (33b)) by  $\Phi_{\mathcal{S}}$ , we approximate the solution of Boltzmann-BGK equation (Eq. (4)) from time  $t$  to  $t + \Delta t$  as:  $\mathbf{f}_i(t + \Delta t, \mathbf{x}) \approx \Phi_{\mathcal{S}} \Phi_{\mathcal{C}} \mathbf{f}_i(t, \mathbf{x})$ .<sup>2</sup>

## B.9 Lattice Boltzmann Scheme

Lattice Boltzmann (LB) algorithms provide a practical and efficient framework for approximating the Boltzmann–BGK equation [4, 5], and consequently, the original conservation law system Eq. (1) (see also [21, 71, 29]). A key feature of LB methods is that the streaming step of the kinetic equation becomes an exact lattice shift, leading to a simple and highly efficient numerical scheme.

The spatial domain  $\Omega$  is discretized into a uniform lattice with spacing  $\Delta \mathbf{x}$ :

$$\mathbb{L}_{\mathbf{x}} = \Delta \mathbf{x} \mathbb{Z}^d \cap \Omega = \{n \Delta \mathbf{x} \in \Omega : n \in \mathbb{Z}^d\}.$$

For  $T > 0$  the time interval  $[0, T]$  is similarly discretized as  $\mathbb{L}_t = \Delta t \mathbb{N} \cap [0, T]$ . For a fixed pair  $(\Delta \mathbf{x}, \Delta t)$ , the lattice speed is defined as  $\Delta \mathbf{x} / \Delta t$ . The velocity set  $\{\mathbf{v}_i\}_{i=1}^Q = \mathcal{V} \subset \mathbb{R}^d$  (cf. Eq. (25)) is chosen as integer multiples of a reference speed  $c_s$ :

$$\mathbf{v}_i = c_s \mathbf{c}_i, \quad \{\mathbf{c}_i\}_{i=1}^Q \subset \mathbb{Z}^d,$$

where  $c_s$  is such that  $c_s \Delta t / \Delta \mathbf{x} = n_{\text{ref}} \in \mathbb{N}$ . This choice guarantees that after one time step  $\Delta t$ , particles land exactly on lattice nodes, making the streaming step a pure index shift.

---

<sup>2</sup>The first numerical application to kinetic equations is attributed to [2], building on Grad's idea [28, p. 246-247] (see [83]).

**Collision Step.** Following [21], the collision operator is discretized using a second-order trapezoidal quadrature, giving

$$\mathbf{f}_i^{\text{coll}}(t, \mathbf{x}) = \Phi_C \mathbf{f}_i(t, \mathbf{x}) = \left(1 - \frac{1}{\tau}\right) \mathbf{f}_i(t, \mathbf{x}) + \frac{1}{\tau} \mathbf{f}_i^{\text{eq}}(\mathbf{U}(t, \mathbf{x})), \quad (t, \mathbf{x}) \in \mathbb{L}_t \times \mathbb{L}_{\mathbf{x}}, \quad (34)$$

where  $\tau$  is the relaxation time,  $\mathbf{f}_i$  the  $i$ -th population, and  $\mathbf{f}_i^{\text{eq}}$  the corresponding discrete equilibrium.

**Streaming Step.** The discrete streaming operator reads [32, 20]

$$\mathbf{f}_i(t + \Delta t, \mathbf{x}) = \Phi_S \mathbf{f}_i(t, \mathbf{x}) = \mathbf{f}_i^{\text{coll}}(t, \mathbf{x} - \mathbf{v}_i \Delta t), \quad (t, \mathbf{x}) \in \mathbb{L}_t \times \mathbb{L}_{\mathbf{x}}. \quad (35)$$

Because  $\mathbf{x} - \mathbf{v}_i \Delta t = \mathbf{x} - c_s \mathbf{c}_i \Delta t = \mathbf{x} - n_{\text{ref}} \mathbf{c}_i \Delta \mathbf{x}$  lies on the lattice, this step reduces to a simple shift in memory, avoiding *costly interpolation*.

**Equilibrium Distribution.** The equilibrium  $\mathbf{f}_i^{\text{eq}}$  is commonly approximated by truncating the Hermite expansion of the Maxwell–Boltzmann distribution Eq. (22) at order  $N$  [27, 73, 46]:

$$f^{\text{MB}}(t, \mathbf{x}, \mathbf{v}_i) \approx f_N^{\text{MB}}(t, \mathbf{x}, \mathbf{v}_i) = \omega(\mathbf{v}_i) \sum_{k=0}^N \frac{1}{k!} \mathbf{a}^{\text{eq},k}(t, \mathbf{x}) : \text{H}^k(\mathbf{v}_i), \quad (36)$$

where  $\omega(\mathbf{v}) = \exp(-|\mathbf{v}|^2/2)(2\pi)^{-d/2}$  is the Gaussian weight and  $\mathbf{a}^{\text{eq},k}$  are the  $k$ -th order Hermite moments of the Maxwellian. The symbol  $:$  denotes full tensor contraction.

Although this polynomial equilibrium is simple and efficient, it is well known to be accurate only at low Mach numbers and prone to instabilities when the flow deviates significantly from the reference state  $(\mathbf{u}, T) = (0, T_0)$  (see [80, Fig. 1]). More robust alternatives, including exponential or entropic closures [47, 80], have been proposed to overcome these limitations, especially in high-speed flow regimes.

**LB Scheme.** The combined LB update is then

$$\mathbf{f}_i(t + \Delta t, \cdot) = \Phi_S \Phi_C \mathbf{f}_i(t, \cdot).$$

With  $n_{\text{ref}} = 1$ , unit lattice speed, and the dimensionless variables  $\mathbf{x} \leftarrow \mathbf{x}/\Delta \mathbf{x}$ ,  $t \leftarrow t/\Delta t$ , the scheme reduces to

$$\mathbf{f}_i(t + 1, \mathbf{x} + \mathbf{c}_i) - \mathbf{f}_i(t, \mathbf{x}) = \frac{1}{\tau} \left[ \mathbf{f}_i^{\text{eq}}(\mathbf{U}(t, \mathbf{x})) - \mathbf{f}_i(t, \mathbf{x}) \right], \quad (t, \mathbf{x}) \in \mathbb{N}_{\geq 0} \times \mathbb{Z}^d. \quad (37)$$

We adopted this dimensionless formulation throughout the main text, see Eq. (5).

## B.10 Closure Relations in Lattice Velocities

Lattice velocity sets  $\{\mathbf{c}_i\}$  always satisfy an algebraic *closure relation*. For simplicity, consider a one-dimensional velocity set  $\mathcal{V} = \{\mathbf{c}_i\}_{i=1}^Q$ . Because only  $Q$  monomials  $\{1, \mathbf{c}_i, \dots, \mathbf{c}_i^{Q-1}\}$  are linearly independent, the  $Q$ -th power can be expressed as a linear combination of lower-order powers:

$$\mathbf{c}_i^Q = \text{poly}(1, \mathbf{c}_i, \dots, \mathbf{c}_i^{Q-1}). \quad (38)$$

For instance, in the standard D1Q3 lattice (velocities  $\mathbf{c}_i \in \{0, \pm 1\}$ ), the closure relation is

$$\mathbf{c}_i^3 = \mathbf{c}_i.$$

Similar relations hold in higher dimensions ( $d > 1$ ), where velocity sets are Cartesian products of one-dimensional sets,  $\{0, \pm 1\}^{\otimes d}$  [37]. These closure properties play a crucial role in determining the order of exact moment recovery and, consequently, the accuracy of LB schemes.

## C NeurDE General Setting and Training Algorithm

This appendix provides additional details on the overall design and training of the LB+NeurDE framework, complementing the discussion in Subsec. 2.2 of the main text. We begin by introducing the general formulation of the operators in Subsec. C.1 and the interpretation of the model as a coupled macroscopic–mesoscopic system in Subsec. C.2. Next, Subsec. C.3 shows that the lattice Boltzmann streaming operator can be interpreted as a non-learnable convolutional network, providing the basis for viewing the entire lattice Boltzmann scheme in Subsec. C.4 as a *neural network* architecture. Finally, we describe the multi-stage training strategy employed for LB+NeurDE, including the pretraining and full model optimization phases; see Subsecs. C.5, C.5.1 and C.5.2.

**Remark.** In this work, we focus primarily on learning the equilibrium mapping within the collision operator, while keeping the streaming operator fixed. However, as explored in Subsec. F.2, it is also possible to extend the formulation to a fully learnable setting by introducing a neural surrogate for the streaming operator, although this approach proved less effective in practice.

### C.1 Operator Structure

Let  $\mathbf{f} = (f_1, \dots, f_Q)^\top$  denote the lattice populations and  $\mathbf{U}(t, \mathbf{x}) = \mathbf{M}[\mathbf{f}]$  the macroscopic observables (density, momentum, energy, temperature). We represent the equilibrium via the composite map

$$\mathbf{f} \xrightarrow{\mathbf{M}} \mathbf{U}(t, \mathbf{x}) \xrightarrow{\phi} \mathbf{f}^{\text{eq}}(t, \mathbf{x}), \quad (39)$$

where  $\phi : \mathbf{U} \mapsto \mathbf{f}^{\text{eq}}$  assigns lattice populations consistent with  $\mathbf{U}$ . In classical LB,  $\phi$  is a fixed, low-order polynomial Maxwellian; here, we replace  $\phi$  by a neural network  $\phi^{\text{NN}}$  and express the collision (Eq. (5a)) as

$$\Phi_{\mathcal{C}}^{\text{NN}} = \left(1 - \frac{1}{\tau}\right)\mathbf{I} + \frac{1}{\tau}(\phi^{\text{NN}} \circ \mathbf{M}), \quad (40)$$

a convex blend between the identity  $\mathbf{I}$  and the learned equilibrium. The streaming operator  $\Phi_{\mathcal{S}}$  (Eq. (5b)) is an exact lattice shift, introducing no trainable parameters or numerical dissipation. It remains fixed, and only  $\Phi_{\mathcal{C}}^{\text{NN}}$  is learned. The complete update is given by the composition  $\Phi_{\mathcal{S}} \Phi_{\mathcal{C}}^{\text{NN}}$  (Eq. (5)).

### C.2 General Formulation and Interpretation

The LB+NeurDE framework couples a macroscopic conservation law with its mesoscopic (kinetic) representation. At the macroscopic level, the system evolves in terms of conserved observables  $\mathbf{U}(t, \mathbf{x})$  that satisfy a nonlinear conservation law (cf. the green region in Fig. 1(a)). At the kinetic level, the dynamics are described by the discrete particle populations

$$\mathbf{f}(t, \mathbf{x}) = [f_i(t, \mathbf{x})]_{i=1}^Q,$$

which evolve according to a discrete Boltzmann–BGK process (cf. the blue region in Fig. 1(a)).

The bridge between these two levels is established by two fixed operators: a *lifting operator*, which maps macroscopic observables  $\mathbf{U}$  to a consistent kinetic state  $\mathbf{f}$ ; and a *projection operator*, which recovers  $\mathbf{U}$  as velocity moments of  $\mathbf{f}$ :

$$\mathbf{U}(t, \mathbf{x}) = \mathcal{D}[\mathbf{f}](t, \mathbf{x}), \quad (41)$$

where  $\mathcal{D}$  is the moment map. For instance,

$$\mathcal{D}[f](t, \mathbf{x}) = \left\langle \left(1, \frac{\mathbf{v}}{\rho(t, \mathbf{x})}, \frac{(\mathbf{v} - \mathbf{u}(t, \mathbf{x})) \cdot (\mathbf{v} - \mathbf{u}(t, \mathbf{x}))}{\rho(t, \mathbf{x})d}\right)^\top, f(t, \mathbf{x}, \mathbf{v}) \right\rangle. \quad (42)$$

During training and inference, LB+NeurDE evolves  $\mathbf{f}$  forward in time using the learned collision operator (NeurDE), embedded within the standard lattice Boltzmann streaming step. The updated state is then projected back to obtain  $\mathbf{U}$ , completing one lifting–evolution–projection cycle. In ML terms, this structure is analogous to an *encoder–decoder model*, with analytically known and fixed encoding (lifting) and decoding (projection) operators.

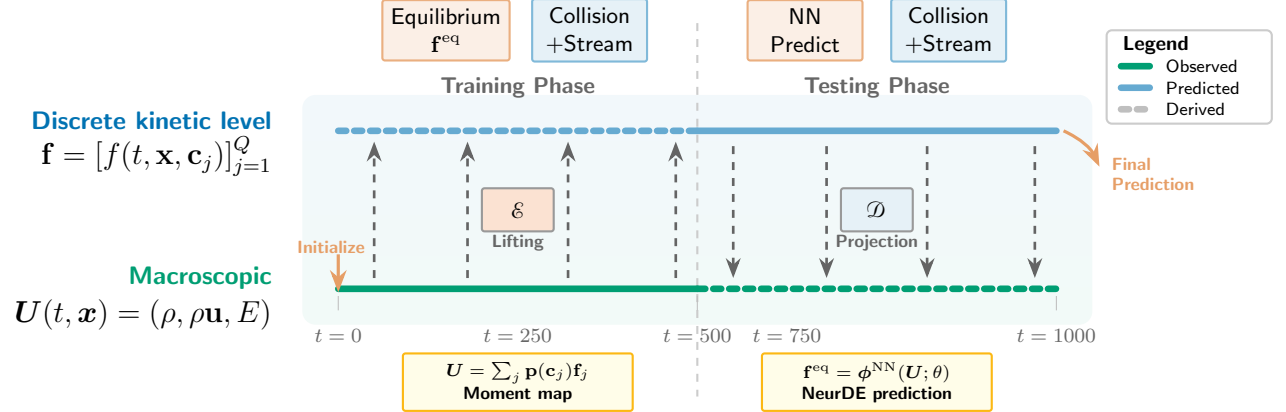


**Figure 7: Detailed interplay between macroscopic and kinetic representations.** The diagram illustrates the complete training and testing workflow (extension of panel a in Fig. 2). The bottom timeline shows macroscopic observables  $\mathbf{U}$  (density, momentum, energy), while the top timeline represents the kinetic distribution  $\mathbf{f} = [f(t, \mathbf{x}, \mathbf{c}_j)]_{j=1}^Q$ . **Training phase (left):** Macroscopic data (solid green) is lifted to the kinetic level via operator  $\mathcal{E}$ , where equilibrium distributions and collision-streaming operators evolve the system. **Testing phase (right):** The trained neural network predicts equilibrium states (solid blue), which are then projected back via  $\mathcal{D}$  to obtain macroscopic predictions. Dashed lines indicate derived quantities. Yellow boxes show key mathematical operations: moment projection maps kinetic to macroscopic variables, while the neural network learns the equilibrium mapping. The vertical dashed line separates observed training data from predictions.

This coupling between the kinetic and macroscopic levels is illustrated schematically in Fig. 7, where training occurs in the kinetic space while observables are recovered by projection at each step. If the governing macroscopic equation Eq. (1) is known exactly, the lifting step requires only the initial and boundary conditions. In more general cases—when the governing dynamics are partially known or approximate—multiple lifting procedures may be employed to ensure that the kinetic representation accurately captures the observed system behavior.

### C.3 Streaming as a Convolutional Neural Network

The lattice Boltzmann streaming step shifts each population  $\mathbf{f}_i$  along its discrete velocity  $\mathbf{c}_i$ . For a general discrete velocity set  $\mathcal{V} = \{\mathbf{c}_i\}_{i=1}^Q$ , the streaming operator—for a dimensionless LB scheme—acts as

$$\mathbf{f}_i(t+1, \mathbf{x}) = \mathbf{f}_i^{\text{coll}}(t, \mathbf{x} - \mathbf{c}_i), \quad i = 1, \dots, Q, \quad (43)$$

where  $\mathbf{f}_i^{\text{coll}}$  denotes the post-collision distribution (see Eq. (5a)). This operator is linear and translational, meaning it can be represented exactly as a *depthwise convolution* in a convolutional neural network (CNN).

**General Convolutional Form.** Let  $\mathbf{f}^{\text{coll}}(t, \mathbf{x}) = (\mathbf{f}_1^{\text{coll}}, \dots, \mathbf{f}_Q^{\text{coll}})^\top$  be the  $Q$ -channel tensor of post-collision distributions. For each discrete velocity direction  $i$ , we define a fixed convolution kernel  $K^{(i)}$  such that

$$K^{(i)}(\ell) = \begin{cases} 1, & \text{if } \ell = -\mathbf{c}_i, \\ 0, & \text{otherwise,} \end{cases} \quad \ell \in \{-L_{\max}, \dots, L_{\max}\}^d, \quad (44)$$

where  $L_{\max}$  is the largest lattice velocity magnitude in any spatial direction (for D2Q9,  $L_{\max} = 1$ ; for higher-order or thermal lattices,  $L_{\max} = 2$  or 3). The streaming operator Eq. (43) is then equivalent to a discrete convolution:

$$\mathbf{f}_i(t+1, \mathbf{x}) = (K^{(i)} * \mathbf{f}_i^{\text{coll}})(t, \mathbf{x}) = \sum_{\ell \in \{-L_{\max}, \dots, L_{\max}\}^d} K^{(i)}(\ell) \mathbf{f}_i^{\text{coll}}(t, \mathbf{x} - \ell), \quad (45)$$

which corresponds to a *depthwise convolution* with  $Q$  input and  $Q$  output channels, where each kernel acts independently on one population channel. All kernel coefficients are fixed (*non-trainable*) and contain a single nonzero entry located according to the discrete velocity  $\mathbf{c}_i$ .

**Example: D2Q9 Lattice.** For the D2Q9 model ( $Q = 9$ ), the discrete velocities are

$$\mathcal{V} = \{(0, 0), (1, 0), (-1, 0), (0, 1), (0, -1), (1, 1), (-1, 1), (-1, -1), (1, -1)\}.$$

Here,  $L_{\max} = 1$ , so the convolution kernels  $K^{(i)}$  are defined on a  $3 \times 3$  stencil. Each kernel has a single one-hot entry at the location  $(-\mathbf{c}_i)$ , and zero elsewhere. Explicitly, the nine kernels correspond to center, right, left, up, down, and the four diagonal shifts.

For example, for the population moving rightward ( $\mathbf{c}_2 = (1, 0)$ ), the kernel is

$$K^{(2)} = \begin{bmatrix} 0 & 0 & 0 \\ 1 & 0 & 0 \\ 0 & 0 & 0 \end{bmatrix},$$

while for the stationary population ( $\mathbf{c}_1 = (0, 0)$ ), the kernel is simply the identity:

$$K^{(1)} = \begin{bmatrix} 0 & 0 & 0 \\ 0 & 1 & 0 \\ 0 & 0 & 0 \end{bmatrix}.$$

All other kernels follow analogously by shifting the single nonzero entry according to  $-\mathbf{c}_i$ .

The streaming operation for all populations can then be expressed compactly as

$$\mathbf{f}(t + 1, \cdot) = \text{DWConv}\left(\mathbf{f}^{\text{coll}}(t, \cdot); \{K^{(i)}\}_{i=1}^9\right), \quad (46)$$

where DWConv denotes a *depthwise convolution* layer with 9 input and output channels, kernel size  $3 \times 3$ , stride 1, and  $\text{groups} = 9$ . Boundary conditions (e.g., periodic, bounce-back, or open) are applied through the convolution padding rule.

**Generalization to Higher-Order Lattices.** For higher-dimensional or multi-speed lattices, the same structure applies with a larger kernel size. If the discrete velocity components satisfy  $\mathbf{c}_{i,\alpha} \in \{-L_{\max}, \dots, L_{\max}\}$  for  $\alpha = 1, \dots, d$ , then the corresponding kernel  $K^{(i)}$  occupies a  $(2L_{\max} + 1)^d$  stencil. For instance:

- **D3Q27:**  $L_{\max} = 1$ , kernel size  $3 \times 3 \times 3$ ;
- **D2Q37 or thermal models:**  $L_{\max} = 3$ , kernel size  $7 \times 7$ ;
- **Generalized high-speed lattices:** kernel size  $(2L_{\max} + 1)^d$ .

Each kernel remains one-hot, representing a deterministic lattice shift.

Thus, for any discrete velocity model, the LBM streaming step can be written as a parameter-free, depthwise convolutional layer:

$$\mathbf{f}(t + 1) = \text{DWConv}\left(\mathbf{f}^{\text{coll}}(t); \{K^{(i)}\}_{i=1}^Q\right), \quad (47)$$

where the kernels  $\{K^{(i)}\}$  encode the discrete velocity set  $\mathcal{V}$ . This establishes a direct correspondence between the streaming operation in kinetic theory and a fixed, sparse convolutional mapping, while the collision operator provides the nonlinear local transformation that may be learned or modeled.

## C.4 LB+NeurDE as an Architecture

The decomposition in panel a of Fig. 8 highlights the equivalence between the lattice Boltzmann update and an autoregressive neural architecture: the streaming operator performs a linear shift (non-learnable convolution), and the collision operator performs a nonlinear local transformation that can be replaced or augmented by a neural network. In our formulation, the equilibrium mapping within the collision operator (Fig. 8b) is parameterized by a neural network, while the streaming operation remains fixed. This modular view implies that, in principle, both operators can be learned end-to-end: replacing the streaming step by learnable convolutional kernels  $K_\ell$  (as explored in Subsec. F.2) yields a fully neural LBM. However, our results indicate that learning the collision operator alone suffices to capture non-equilibrium dynamics, while maintaining the physical stability ensured by the fixed streaming stencil.

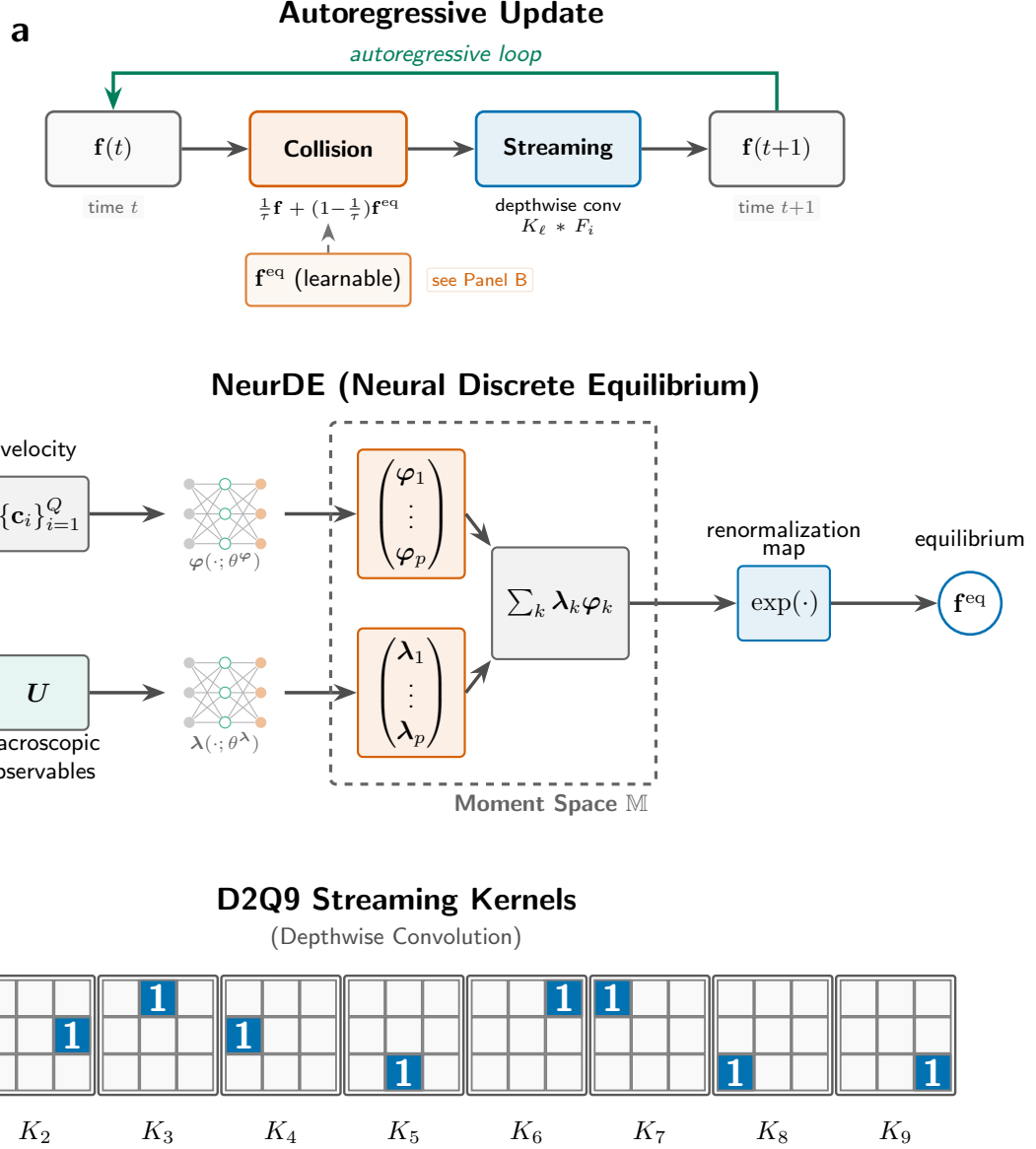


**Figure 8: Neural lattice Boltzmann architecture.** **a.** The lattice Boltzmann update as an *autoregressive neural network*. Collision and streaming act as sequential layers. The output  $\mathbf{f}(t+1)$  recursively serves as the next input. **b.** The learnable equilibrium  $\mathbf{f}^{\text{eq}}$ . Small neural networks (gray/green/red icons) map macroscopic observables  $\mathbf{U}$  and lattice velocities onto the moment space  $\mathbb{M}$ . The inner product of these features followed by an exponential renormalization ensures thermodynamic consistency. **c.** The streaming operator as fixed, sparse depthwise convolution kernels  $\{K_\ell\}$ .

## C.5 Training Scheme

As we described in the main text, Subsec. 2.2, the training of LB+NeurDE consists of two consecutive stages: (1) a *pretraining stage*, where NeurDE is learned independently to predict equilibria from macroscopic observables, and (2) a *joint training stage*, where NeurDE is integrated into the kinetic solver ( $\Phi_S \Phi_C$ )—forming what we called LB+NeurDE—and optimized through multi-step trajectory prediction. This hierarchical procedure ensures both local physical consistency (through pretraining) and global dynamical accuracy (through joint training).

### C.5.1 Pretraining Procedure

Pretraining provides a robust initialization for NeurDE by ensuring that the learned equilibrium distributions satisfy basic physical constraints before being embedded into the kinetic dynamics. A randomly initialized model often leads to unstable behavior during joint training; pretraining alleviates this issue.

Given a dataset of macroscopic-equilibrium pairs  $\{(\mathbf{U}_n, \mathbf{f}_n^{\text{eq}})\}_{n=1}^N$ , we train NeurDE using supervised regression:

$$\min_{\theta} \sum_{n=1}^N \ell(\phi^{\text{NN}}(\mathbf{U}_n; \theta), \mathbf{f}_n^{\text{eq}}), \quad (48)$$

where  $\ell$  denotes an appropriate loss function (e.g., an  $L^2$  norm). The targets  $\mathbf{f}_n^{\text{eq}}$  may be obtained either from high-resolution kinetic simulations or by solving Levermore's exponential closure problem [51, 47].

Alternatively, synthetic training data can be generated from the exponential ansatz

$$\mathbf{f}_n = \left[ \exp \left( \sum_{k=1}^p \lambda_{n,k} \varphi_k(\mathbf{c}_i) \right) \right]_{i=1}^Q,$$

where  $\varphi_k$  are chosen moment basis functions (e.g., Eulerian or Levermore bases; cf. Subsec. B.6),  $\alpha_{n,k} \sim \mathbb{P}$  are sampled coefficients, and the associated observables are computed as  $\mathbf{U}_n = \mathcal{D}[\mathbf{f}_n]$ .

### C.5.2 Training Algorithm

In the second stage, the pretrained NeurDE is embedded into the kinetic update operator  $\Phi_S \Phi_C$ —yielding the full LB+NeurDE scheme—and optimized end-to-end by comparing predicted trajectories against high-fidelity reference simulations. The training objective minimizes discrepancies in both the predicted populations  $\mathbf{f}$  and their corresponding equilibria  $\mathbf{f}^{\text{eq}}$  over prediction horizons of length  $N_r$ :

$$L = \sum_{r=t}^{t+N_r} \alpha \ell(\mathbf{f}(r), \mathbf{f}^{\text{pred}}(r)) + (1 - \alpha) \ell(\mathbf{f}^{\text{eq}}(r), \mathbf{f}^{\text{eqpred}}(r)),$$

where  $\alpha \in [0, 1]$  controls the trade-off between mesoscopic and equilibrium-level losses.

The complete algorithm is outlined below (see Algorithm 1).

---

**Algorithm 1:** Training LB+NeurDE ( $\Phi_S \Phi_C^{\text{NN}}$ )

---

```

Data:  $\tau, \{\mathbf{c}_i\}_{i=1}^Q, \{W_i\}_{i=1}^Q, \alpha \in [0, 1], \eta, N_r, \alpha' = 1 - \alpha$ ;           // Set parameters, boundary conditions
{1}  $\theta \leftarrow \text{pretraining}(\theta \sim \text{random})$ ;                                         // Perform pre-training as previously described
{2}  $\{\{\mathbf{f}(0, \mathbf{x}), \mathbf{f}^{\text{eq}}(0, \mathbf{x})\}, \dots, \{\mathbf{f}(t_{N_{\text{train}}}, \mathbf{x}), \mathbf{f}^{\text{eq}}(t_{N_{\text{train}}}, \mathbf{x})\}\}$ ;           // Load training data
{3} for  $0 \leq \text{epoch} \leq N$  do
{4}   for  $0 \leq t \leq t_{N_{\text{train}}}$  do
{5}      $t_{\text{end}} = \min(t_{N_{\text{train}}}, t + N_r)$ ;
{6}      $\mathbf{F}_{\text{hist}}^{\text{pred}}, \mathbf{F}_{\text{hist}}^{\text{eq}} = \text{LB\_NeurDE}(t, t_{\text{end}}, \mathcal{D}[\mathbf{f}](t, \mathbf{x}))$ ;           // Make temporal prediction
{7}      $L \leftarrow \sum_{r=t}^{t_{\text{end}}} \alpha \ell(\mathbf{f}(r, \mathbf{x}), \mathbf{F}_{\text{hist}}^{\text{pred}}[r, \mathbf{x}]) + \alpha' \ell(\mathbf{f}^{\text{eq}}(r, \mathbf{x}), \mathbf{F}_{\text{hist}}^{\text{eq}}[r, \mathbf{x}])$ ;           // Accumulate loss
{8}      $\theta \leftarrow (\theta - \eta \partial_{\theta} L)$ ;                                         // Update the parameters
{9}      $t \leftarrow t + 1$ ;
{10}   end
{11}    $\text{epoch} \leftarrow \text{epoch} + 1$ ;
{12} end
Output:  $\phi^{\text{NN}}(\cdot; \theta)$ 

```

---

**Training and optimization.** The gradient-based optimization of LB+NeurDE proceeds through *back-propagation through time* (BPTT) applied to the unrolled kinetic solver. Each training trajectory of length  $N_r$  corresponds to an unrolled sequence of discrete-time operators  $(\Phi_s \Phi_c)$ , with the neural closure  $\phi^{\text{NN}}$  (NeurDE) embedded within the collision step. The loss in line 7 of Algorithm 1 is differentiated through this sequence using automatic differentiation, propagating gradients across both streaming and collision operations. This structure enables the model to learn stable long-term dependencies of the kinetic evolution while preserving the physical symmetries and lattice topology.

Similar unrolled training strategies have been employed in differentiable flow simulations [39, 23] and more general differentiable PDE solvers [9, 53]. The hyperparameter  $N_r$  determines the prediction horizon (i.e., the number of unrolled steps in BPTT). Its choice depends on both the dataset characteristics and the initialization of the network parameters  $\theta$  in NeurDE. In our empirical evaluation (Subsec. 2.3),  $N_r$  ranged from 10 to 25, beyond which improvements became marginal while computational cost increased substantially.

The loss weighting parameter  $\alpha \in [0, 1]$  controls the balance between kinetic and equilibrium-level objectives. For the tests in Subsec. 2.3, setting  $\alpha = 0$  already yielded stable and accurate training. Regularization can further improve generalization: for instance, by imposing soft constraints on the conservation of moments in  $\mathbf{f}_i^{\text{eq,pred}}$ . When higher-order moment closures are introduced [47], relaxing them via inequality-based penalties (e.g.,  $\text{relu}(\langle \varphi(\mathbf{c}_i) \phi^{\text{NN}} \rangle_\mu - \langle \varphi(\mathbf{v}) f^{\text{MB}} \rangle))$ ) can alleviate non-existence issues for feasible equilibrium solutions [65]. Further implementation and optimization details are provided in Subsecs. 2.3 and D.4.

## D Empirical Evaluation

This appendix provides supplementary details for the empirical evaluation presented in the main text (Subsec. 2.3). It focuses on methods and parameters applicable to all test cases; experiment-specific configurations for the Sod shock tube and the flow over a cylinder are given in Sec. E and Sec. G, respectively.

We first elaborate on the underlying physics model: the two-population thermal lattice Boltzmann formulation (Subsec. D.1) and the polynomial expansion of the  $\mathbf{f}$  and  $\mathbf{g}$  population equilibria (Subsecs. D.1.1 and D.1.2). The  $\mathbf{g}$  equilibrium is used in the subsonic Sod (Subsec. 2.3.1) as a benchmark following [38, 69]. As discussed in the main text, the polynomial approximation deteriorates at high Mach numbers, becoming numerically unstable in transonic and supersonic regimes. We then describe the neural network implementation and training details, including the architecture (Subsec. 4.2), optimization parameters (Subsecs. D.3 and D.4), and dataset composition and computational setup (Subsec. D.5).

### D.1 Two-Population Thermal LB Scheme

This subsection expands on the consistent two-population model introduced in Subsec. 4.2 (see [38, 69]). In particular, we specify the temperature-dependent weights  $W_i$ , the quasi-equilibrium state defined in Eq. (8b), and in Subsecs. D.1.1 and D.1.2 we describe the polynomial expansion of the  $\mathbf{f}$  and  $\mathbf{g}$  populations.

We recall from the main text that the relaxation parameters  $\tau_1$  and  $\tau_2$  in Eq. (8) correspond to the dynamic viscosity  $\mu$  and thermal conductivity  $\kappa$ , which are defined as,

$$\mu = (\tau_1 - \frac{1}{2})\rho T, \quad (49)$$

and

$$\kappa = C_p (\tau_2 - \frac{1}{2})\rho T,$$

where  $C_v$  and  $C_p$  are the specific heats at constant volume and pressure (Subsec. 4.2), respectively, and all quantities are expressed in lattice units. The Prandtl number is then  $\text{Pr} = C_p \mu / \kappa$ .

As a consequence of the variable Prandtl number, the intermediate quasi-equilibrium state  $\mathbf{g}_i^*$  is introduced in Eq. (8b) (cf. [38]) and is defined as

$$\mathbf{g}_i^* \stackrel{\text{def.}}{=} \mathbf{g}_i^{\text{eq}} + \frac{2}{T} W_i \mathbf{u}_\beta \left( \mathbf{P}_{\alpha,\beta} - \mathbf{P}_{\alpha,\beta}^{\text{eq}} \right) \mathbf{c}_{i,\alpha}, \quad (50)$$

where the  $W_i$  are temperature-dependent weights [69], given by:

$$W_i = \prod_{\alpha} W_{i,\alpha}, \quad W_{\pm 1} = \frac{1}{2} T, \quad W_0 = 1 - T \quad \alpha \in \{x, y\} \text{ or } \alpha \in \{x, y, z\}. \quad (51)$$

The pressure tensors  $\mathbf{P}$  and  $\mathbf{P}^{\text{eq}}$  in Eq. (50) are higher-order moments, defined as  $\mathbf{P} = \langle \mathbf{c} \otimes^{\text{sym}} \mathbf{c} \mathbf{f} \rangle$  and  $\mathbf{P}^{\text{eq}} = \langle \mathbf{c} \otimes^{\text{sym}} \mathbf{c} \mathbf{f}^{\text{eq}} \rangle$ .<sup>3</sup>

Other relevant higher-order moments include: the heat flux vector, defined as  $\mathbf{q} = \langle \mathbf{c} \mathbf{g} \rangle$ , and its equilibrium counterpart  $\mathbf{q}^{\text{eq}} = \langle \mathbf{c} \mathbf{g}^{\text{eq}} \rangle$ ; and the contracted fourth-order moment tensor  $\mathbf{R} = \langle \mathbf{c} \otimes^{\text{sym}} \mathbf{c} \mathbf{g} \rangle$ , with its equilibrium form being  $\mathbf{R}^{\text{eq}} = \langle \mathbf{c} \otimes^{\text{sym}} \mathbf{c} \mathbf{g}^{\text{eq}} \rangle$ . See, e.g., Subsec. B.7.

#### D.1.1 Polynomial Equilibrium for the $\mathbf{f}$ Population

For the equilibrium of the first population—in the experiments of the main text—we employ the extended equilibrium distribution [37],

$$\mathbf{f}^{\text{eq}} = \rho \Psi \otimes \Psi, \quad (52)$$

where  $\Psi = (\Psi_0, \Psi_1, \Psi_{-1})^\top$ ,<sup>4</sup> with

$$\Psi_{\pm 1} = \frac{1}{2} [\pm (\mathbf{c}_\alpha - \mathbf{u}_\alpha) + (\mathbf{c}_\alpha - \mathbf{u}_\alpha)^2 + T], \quad \Psi_0 = 1 - [(\mathbf{c}_\alpha - \mathbf{u}_\alpha)^2 + T],$$

for  $\alpha = x, y$ . This formulation is derived and discussed in [67, 37].

<sup>3</sup>Following previous work [16], Greek indices are used for vector components, while Roman indices are used to label discrete lattice vector. The Einstein's convention summation is applied to Greek indices (e.g., Eq. (50)).

<sup>4</sup>The order may vary based on the chosen enumeration of the lattice velocities.

### D.1.2 Polynomial Equilibrium for the $\mathbf{g}$ Population

In [38], the equilibrium distribution for the  $\mathbf{g}$  population is formulated as a polynomial expansion of the energy. The expansion originates from the Maxwellian form

$$\mathbf{g}^{\text{eq}} \sim (\mathbf{v} \cdot \mathbf{v}) \exp\left[-\frac{(\mathbf{v}-\mathbf{u}) \cdot (\mathbf{v}-\mathbf{u})}{2T}\right] = (\mathbf{v} \cdot \mathbf{v}) \mathbf{g}^{\text{MB}},$$

where  $\mathbf{g}^{\text{MB}}$  denotes the Maxwellian distribution given in Eq. (22). This can be expressed as

$$\mathbf{g}_{i,\text{poly}}^{\text{eq}} = W_i \left( 2\rho E + \frac{\mathbf{q}_\alpha^{\text{MB}} \mathbf{c}_{i,\alpha}}{T} + \frac{(\mathbf{R}_{\alpha,\beta}^{\text{MB}} - 2\rho ET\delta_{\alpha,\beta})(\mathbf{c}_{i,\alpha} \mathbf{c}_{i,\beta} - T\delta_{\alpha,\beta})}{2T^2} \right), \quad (53)$$

where  $W_i$  is defined in Eq. (51),  $\mathbf{q}^{\text{MB}}$  is the Maxwellian heat flux, and  $\mathbf{R}^{\text{MB}}$  the contracted fourth-order moment of the Maxwellian distribution (see Subsec. B.7).

## D.2 Datasets

All datasets considered in Subsec. 2.3 are generated using the kinetic scheme in Eq. (8). For  $\mathbf{g}_i^{\text{eq}}$ , we employ Levermore's model:

$$\mathbf{g}_i^{\text{eq}} = \rho W_i \exp(\alpha_1 + \alpha_{\mathbf{c}_i} \cdot \mathbf{c}_i), \quad (54)$$

where  $W_i$  is a temperature-related weight (see Eq. (51) in Subsec. D.1) and  $\rho$  is the local density. The parameters  $\boldsymbol{\lambda} = (\alpha_1, \alpha_{\mathbf{c}_{i,x}}, \alpha_{\mathbf{c}_{i,y}})$  are determined using the Newton–Raphson method at each spatio-temporal point, as detailed in [47]. The iteration terminates when either the maximum absolute difference between consecutive  $\boldsymbol{\lambda}$  values is below  $10^{-6}$ , or after 20 iterations if convergence is not achieved.<sup>5</sup>

For the equilibrium of the first population, we employ the extended equilibrium distribution defined in Subsec. D.1.1. While computing the numerical equilibrium for both populations could yield slightly more accurate results, the computational cost of applying Newton's method twice per time step renders this approach impractical. The extended equilibrium (Eq. (52)) is already fourth-order accurate with respect to the Mach number and does not significantly affect overall accuracy.

This configuration offers two main advantages: (1) it simplifies dataset generation by requiring Newton's method for only one population, and (2) it mitigates errors associated with the equilibrium of the second population, as analyzed in [69, Eq. 26] through a correction term. Instead of introducing such corrections explicitly, we rely on the learned surrogate NeurDE to approximate them implicitly.

## D.3 Architecture Parameters

Table 2 summarizes the neural network architectures used in the experiments of Subsec. 2.3.

Experiment	Network	Activation	Layer size	Input	Renormalization map $\beta(\cdot)$
SOD case 1 (Eq. (10))	$\boldsymbol{\lambda}$ $\varphi$	GELU	4x32, 32x32, 32x32, 32x32 9x32, 32x32, 32x32, 32x32	$\mathbf{U} = (\rho, \mathbf{u}, T)^\top$ $\{\mathbf{c}_i : i = 1, \dots, 9\}$	$\exp(\cdot)$
SOD case 2 (Eq. (11))	$\boldsymbol{\lambda}$ $\varphi$	GELU	4x64, 64x64, 64x64, 64x64 9x64, 64x64, 64x64, 64x64	$\mathbf{U} = (\rho, \mathbf{u}, T)^\top$ $\{\mathbf{c}_i : i = 1, \dots, 9\}$	$\exp(\cdot)$
Cylinder (Subsec. 2.3.2)	$\boldsymbol{\lambda}$ $\varphi$	GELU	4x32, 32x32, 32x32, 32x32 9x32, 32x32, 32x32, 32x32	$\mathbf{U} = (\rho, \mathbf{u}, T)^\top$ $\{\mathbf{c}_i : i = 1, \dots, 9\}$	$\exp(\cdot)$

**Table 2:** Neural network architectures used in Subsecs. 2.3.1 and 2.3.2.

<sup>5</sup>All experiments are performed in single precision for computational efficiency.

## D.4 Optimization Algorithm

All experiments employ the AdamW optimizer. During the first (pre-training) stage, the learning rate is initialized at  $10^{-3}$  and reduced by a factor of  $\frac{1}{2}$  every 100 epochs over a total of 500 epochs. In the second training stage, where LB+NeurDE learns from problem-specific trajectories (Algorithm 1), the learning rate is fixed at  $10^{-4}$  with the same linear scheduler and  $N_r = 25$ . Empirically, the results show minimal sensitivity to the parameter  $\alpha \in [0, 1]$  in Algorithm 1; hence, we set  $\alpha = 0$  for simplicity. The  $L^2$ -norm is used as the loss  $\ell$  in all experiments.

For both the Sod shock tube (Subsec. 2.3.1) and the 2D supersonic flow (Subsec. 2.3.2), the trajectory dataset is defined as

$$\mathcal{D} \stackrel{\text{def.}}{=} \left\{ \{\mathbf{f}_i(t, \mathbf{x}), \mathbf{g}_i(t, \mathbf{x}), \mathbf{g}_i^{\text{eq}}(t, \mathbf{x})\}_{i=1}^9 : t = 0, \dots, t_N, N > 500, \mathbf{x} \text{ in the computational domain} \right\}. \quad (55)$$

We use the first 500 time steps from  $\mathcal{D}$  for training. In Subsec. 2.4.2, training is limited to the first 150 temporal points.

## D.5 Training and Computational Setup

All LB experiments (assuming a known equilibrium) were implemented as standalone Python codes. The pre-training and main training phases both utilize the dataset defined in Eq. (55). During pre-training, samples are used independently of their temporal order. In contrast, the second stage explicitly incorporates temporal evolution, as described in Algorithm 1.

The randomly generated parameters  $\lambda$  introduced in Subsec. 2.2 were not required for the main experiments (Subsecs. 2.3.1 and 2.3.2), as the existing trajectory data were sufficient. Each experiment uses a single trajectory representing the evolution of Eq. (1) under given initial and boundary conditions. Typically, the first 500 time steps are used for training, except in the case of Subsec. 2.4.2, where only 150 samples are available. To augment this smaller dataset during pre-training, an additional 350 randomly generated  $\alpha_n$  values are used to construct the pairs

$$\{\mathbf{U}_n, [W_i \exp(\alpha_{n,1} + \alpha_{n,\mathbf{c}_i} \cdot \mathbf{c}_i)]_{i=1}^9\},$$

while reserving the original 150 samples of Eq. (55) for the second training phase.

Training was performed on a Tesla V100-DGXS-32GB GPU. Typical total training times were under one day per model, with most of the time spent in the second-stage trajectory-based training (Algorithm 1). Pre-training typically completed within a few hours.

## E Shock Tube

This appendix details the numerical setup for the Sod shock tube experiments (Subsecs. E.1 and E.2). For both the subsonic and transonic configurations, the *computational domain* consists of a grid of  $3001 \times 5$ . The model is trained over the first 500 time steps and subsequently evaluated in an autoregressive manner for the next 500 steps.

We present analyses common to both flow regimes. We first examine the local Mach number distributions (Subsecs. E.1.1 and E.2.4) to confirm the subsonic and transonic character of the respective compressible flows discussed in the main text (Subsec. 2.3.1). We then extend the long-horizon evaluation of Subsec. 2.4, specifically Subsec. 2.4.1, by initializing the simulation at progressively later time points—without retraining NeurDE—to assess its extrapolation capabilities beyond the training window (Subsecs. E.1.2 and E.2.6). In both cases, the model eventually fails when initialized more than 2500 time steps away from the training data (3900 for the subsonic and 2500 for the transonic case). Notably, this degradation is gradual and stable, indicating *graceful degradation* rather than catastrophic divergence. For completeness, and to complement our comparison with FNO, additional details for the subsonic case are provided in Subsec. E.1.3.

For the transonic case, we further detail the modified training protocol, which differs from Algorithm 1 through the inclusion of a total variation diminishing (TVD) regularizer. In Subsec. E.2.1, we describe this TVD regularization procedure and demonstrate its effectiveness in suppressing oscillations and improving the smoothness of the predicted solutions. Finally, Algorithm 2 shows the extension of the baseline training algorithm to incorporate the TVD regularization term. For completeness, Subsec. E.2.5 reports the equilibrium errors observed in the transonic regime when using the  $g$ -population polynomial equilibrium described in Eq. (53).

### E.1 Subsonic Shock Tube Case (from Subsec. 2.3.1)

This subsection provides supplementary information regarding subsonic Sod shock tube case (as introduced in Subsec. 2.3.1). Subsec. E.1.1 illustrates the local Mach number distribution within the shock tube at time  $t = 700$ ; and Subsec. E.1.2 presents the model failure of this case at different initial conditions, expanding on the analysis presented in Subsec. 2.4.1 for the subsonic case.

#### E.1.1 Subsonic Nature of the Experiment

Fig. 9 visually confirms the subsonic nature of the case, a characteristic we have emphasized throughout the primary portion of this work. For the local Mach number we use

$$Ma = (\mathbf{u} \cdot \mathbf{u})^{1/2} (\gamma RT)^{-1/2}.$$

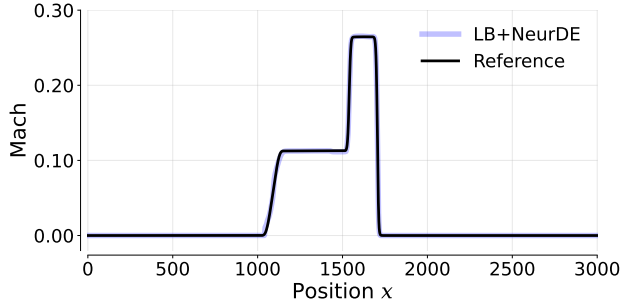


**Figure 9:** Comparison of the local *Mach* number for the subsonic Sod shock tube (case 1 Eq. (10)) between LB+NeurDE and simulation results. The black line represents the numerical reference, while the blue line depicts the flow predicted by LB+NeurDE. This snapshot is taken at time-step 700.

### E.1.2 Model Failure (from Subsec. 2.4.1)

Here, we explore the limits of the model when initialized with very long time-steps, a strategy presented in Subsec. 2.4.1. We recall that the architecture was previously trained in Subsec. 2.3.1 using only the first 500 time-steps of its dataset. In Subsec. 2.4.1, we demonstrated that the model could predict the next 100 time-steps of the flow evolution starting at time  $t = 2000$ . Here, we consider a more extreme case by using time  $t = 3900$  as an initial condition and utilizing our LB+NeurDE to predict the subsequent 100 time-steps. In Fig. 10, we observe that the model *gracefully deviates* from the reference solution.

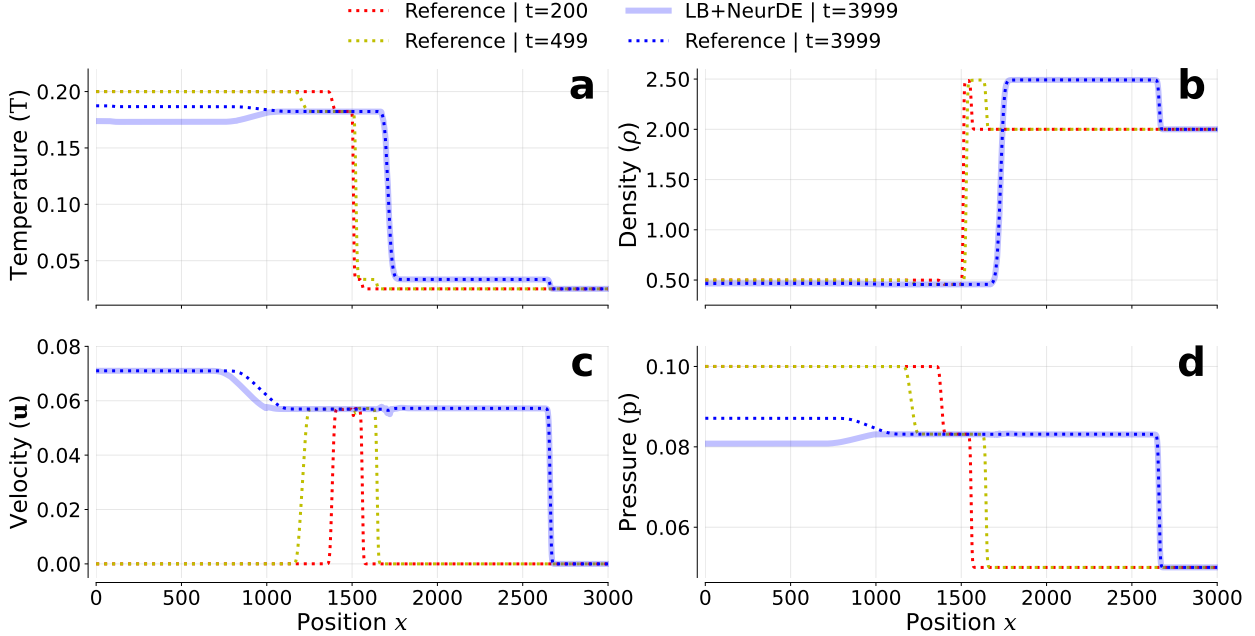


**Figure 10:** LB+NeurDE’s failure on the subsonic Sod shock tube when predicting  $t = 3999$  after being initialized at  $t_0 = 3900$ . The solid blue line represents the LB+NeurDE prediction and the dotted lines represent simulated results at different times. We show the *temperature*, *density*, *velocity*, and *pressure* variables in panels a, b, c, and d, respectively.

### E.1.3 FNO Benchmark

To establish a rigorous baseline, we trained and evaluated the Fourier Neural Operator (FNO) [52] on the subsonic Sod shock tube problem. We note that resolving sharp features (particularly shock discontinuities) is very challenging for any spectral method, including FNO [58, 70]. To address this, we target large numbers of Fourier modes to the point where the model’s size makes its utility unfeasible. The hyperparameter space was designed to maximize spectral resolution while respecting the memory bandwidth limits of high-performance accelerators. Training was conducted on compute nodes equipped with 4× NVIDIA A100 GPUs (40 and 80,GB HBM2e).

We explored the following configuration grid:

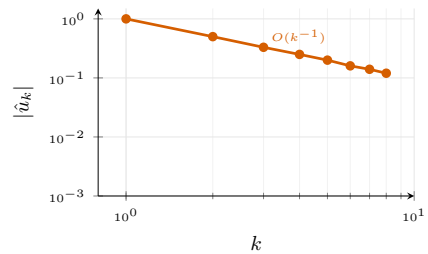
- **Lifting Dimension ( $d_v$ ):** {128, 256}
- **Fourier Modes ( $\mathbf{k}_{\max}$ ):** {(128, 3), (256, 3), (512, 3)}
- **Network Depth ( $L$ ):** {4, 8} layers

The computational scaling of the FNO is dominated by the spectral layers, where the memory overhead of the fast Fourier transform (FFT) operations limits the achievable modal size. The number of FFT modes also limits FNO’s ability to resolve sharp features like shocks. To strictly maximize the baseline’s representational



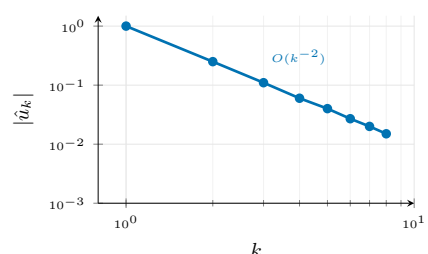
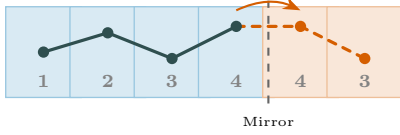
### a Periodic Extension

Standard FNO: Spectral leakage at non-periodic boundaries



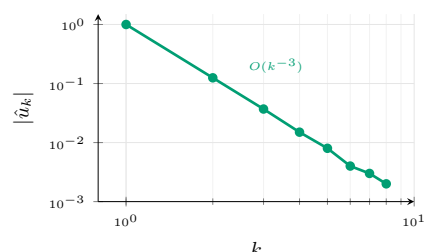
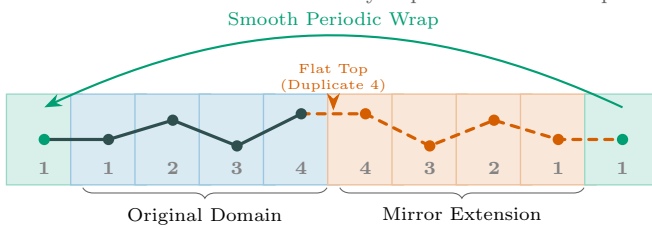
### b Symmetric (Reflective)

Preserves  $C^0$  continuity but introduces derivative kinks



### c Palindromic Edge-Padded Extension

True  $C^1$  smoothness achieved by duplication at mirror point



**Mechanism:** Palindromic mirror + edge duplication forces matching value *and* near-zero gradient at the periodic wrap (effective  $C^1$  continuity), dramatically reducing spectral leakage.

**Figure 11: Impact of boundary extension strategies on spectral convergence.** (a) Standard periodic extension of non-periodic data induces a jump discontinuity, resulting in slow  $O(k^{-1})$  spectral decay (Gibbs phenomenon). (b) Symmetric reflection ensures  $C^0$  continuity but introduces derivative discontinuities (“kinks”), limiting decay to  $O(k^{-2})$ . (c) The proposed **Palindromic Edge-Padded Extension** mirrors the domain and duplicates edge values, forcing a zero-gradient condition at the periodic wrap. This enforces effective  $C^1$  continuity, accelerating spectral decay to  $O(k^{-3})$  and significantly reducing aliasing artifacts in the FNO baseline.

capacity, we prioritized spectral bandwidth over training throughput. Specifically, targeting  $\mathbf{k}_{\max} = 512$  Fourier modes with a lifting dimension of  $d_v = 256$  required saturating the combined 320 GB memory envelope of the 4 A100 (320 GB) accelerators. Consequently, we reduced the effective batch size (from 32 to 4 per GPU) to accommodate the dense optimizer states and intermediate activations. This configuration represents the maximal parameter density feasible on this hardware, ensuring the baseline is limited by its inductive bias rather than insufficient capacity.

**Boundary Conditions.** FNOs assume periodicity due to their use of spectral convolutions, which conflicts with the non-periodic Neumann boundaries of the Sod shock tube. A naïve periodic wrap introduces a jump discontinuity and associated  $O(k^{-1})$  spectral decay. To mitigate this artifact, we apply a *Palindromic Edge-Padded Extension*, which mirrors the domain and duplicates the boundary values. This enforces an approximately zero-gradient condition at the periodic interface, yielding an effectively  $C^1$  periodic extension. The resulting spectral decay improves to  $O(k^{-3})$ , substantially reducing leakage and aliasing (Fig. 11).

Configuration			Model Stats		Error Metrics (MSE)			
$d_v$	$\mathbf{k}_{\max}(x, y)$	$L$	Params	Epoch	Val Loss	$\rho$	$\mathbf{u}$	$T$
128	(128, 3)	4	33.7M	499	<b>3.20e-4</b>	<b>2.69e-4</b>	3.75e-5	1.35e-5
128	(128, 3)	8	67.3M	131	1.42e-3	1.30e-3	8.78e-5	3.96e-5
256	(128, 3)	4	134.6M	499	4.23e-4	3.83e-4	3.08e-5	9.00e-6
256	(128, 3)	8	269.1M	155	4.48e-1	4.37e-1	4.77e-3	6.61e-3
128	(256, 3)	4	67.2M	182	4.52e-4	3.52e-4	7.48e-5	2.50e-5
128	(256, 3)	8	134.4M	147	1.11e-3	9.87e-4	8.28e-5	3.86e-5
256	(256, 3)	4	268.8M	168	5.15e-4	4.29e-4	6.38e-5	2.29e-5
256	(256, 3)	8	537.5M	141	1.12e-3	1.02e-3	7.75e-5	2.28e-5
128	(512, 3)	4	134.4M	147	6.41e-4	6.00e-4	3.28e-5	8.05e-6
128	(512, 3)	8	268.6M	147	8.16e-4	7.46e-4	5.77e-5	1.16e-5
256	(512, 3)	4	537.3M	139	1.16e-3	1.10e-3	3.98e-5	1.44e-5
256	(512, 3)	8	1.07B	131	1.05e-3	9.63e-4	6.61e-5	2.02e-5

**Table 3: Performance of Fourier Neural Operator variants.** We compare models with varying hidden channel width ( $h$ ), Fourier modes ( $\mathbf{k}_{\max}$ ), and depth ( $L$ ). We also report the number of parameters and the epoch at which the best validation loss was achieved. Training utilized early stopping with a patience of 100 epochs, causing larger models to terminate earlier than the maximum 500 epochs once validation loss plateaued. The best result for each metric is highlighted in bold.

**FNO Architecture and Training Protocol.** To evaluate the limits of the spectral approach, we deployed a high-capacity FNO architecture consisting of 8 Fourier layers with a hidden channel width of 256. We utilized a 2D spectral convolution retaining the top 512 modes in the spatial dimension to maximize the capture of high-frequency shock content. As detailed in the previous section, we applied reflective (palindromic) boundary padding to mitigate spectral leakage at the non-periodic boundaries.

The model was trained to map the primitive variables  $(\rho, u, T)$  at step  $t$  to step  $t + 1$  using a dataset derived from the kinetic simulation (Compressible regime,  $\Pr = 0.71$ ,  $\nu = 0.025$  as specified in Eq. (10), see Subsec. 4.4). The data was split 50/20/30 (train/validation/test) with a batch size of 4. We minimized the Mean Squared Error (MSE) using the AdamW optimizer ( $\beta_1 = 0.9$ ,  $\beta_2 = 0.999$ , weight decay  $1 \times 10^{-4}$ ) over 500 epochs. To ensure stable convergence, we employed a OneCycle learning rate scheduler, linearly warming up to a maximum learning rate of  $1 \times 10^{-3}$  for the first 30% of training before annealing down to  $1 \times 10^{-6}$ . Gradients were clipped at a norm of 1.0 to prevent divergence during the initial training phase.

**FNO Experimental Results.** Our empirical results show that FNO struggles to accurately predict the next time step ( $\Delta t = 1$ ) for all our models. Table 3 shows the validation results for our hyperparameter tuning. We observe that the models with fewer frequency components (128) generally outperform models with more frequency modes. Figures 12 and 13 show best two FNO temporal forecasting models with 128 Fourier modes, and 128 and 256 embedding dimensions, respectively, and 4 layers. Figure 14 shows the results from our largest model with 512 Fourier modes, 256 embedding dimensions, and 8 layers. In stark

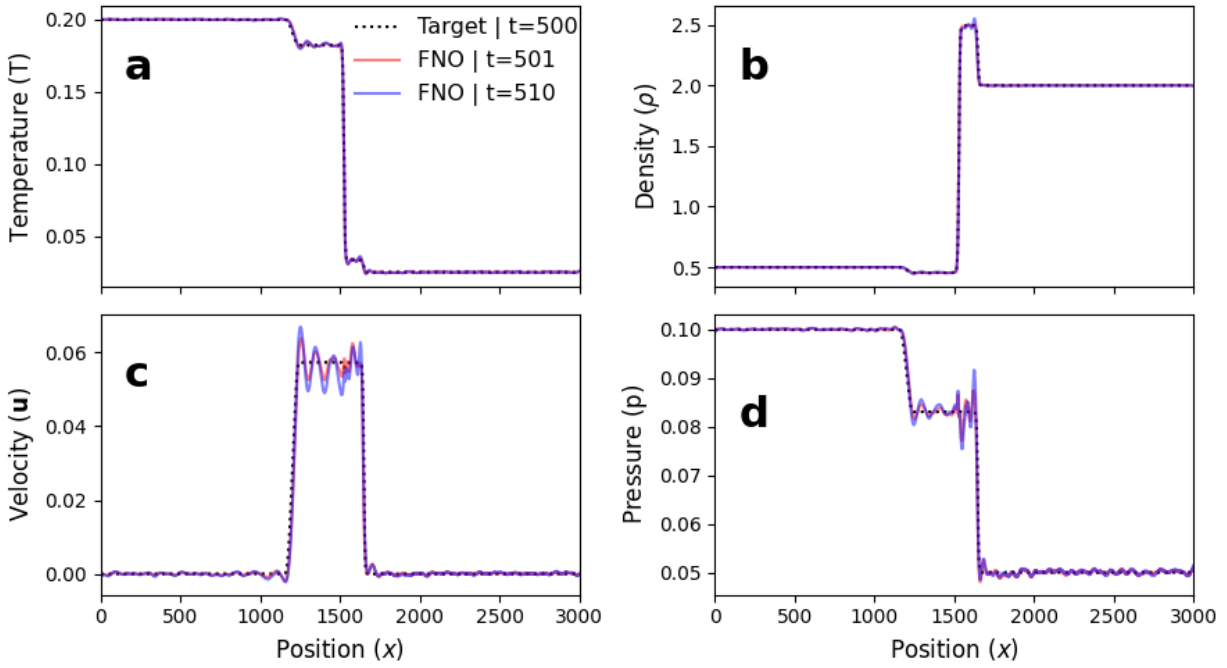


**Figure 12:** We train and evaluate the FNO model on the subsonic Sod shock tube with 128 Fourier modes, 128 embedding dimensions, and 4 layers. We evaluate (a) Temperature, (b) Density, (c) Velocity, and (d) Pressure for only 1 and 10 time steps.

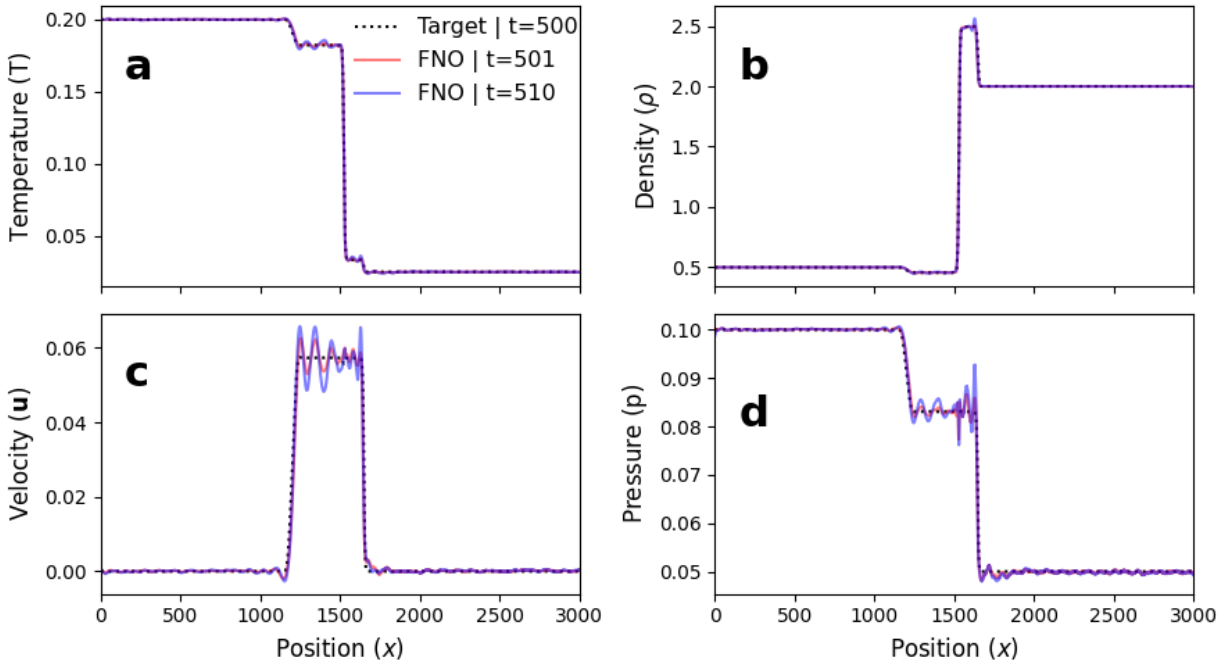


**Figure 13:** We train and evaluate the FNO model on the subsonic Sod shock tube with 128 Fourier modes, 256 embedding dimensions, and 4 layers. We evaluate (a) Temperature, (b) Density, (c) Velocity, and (d) Pressure for only 1 and 10 time steps.

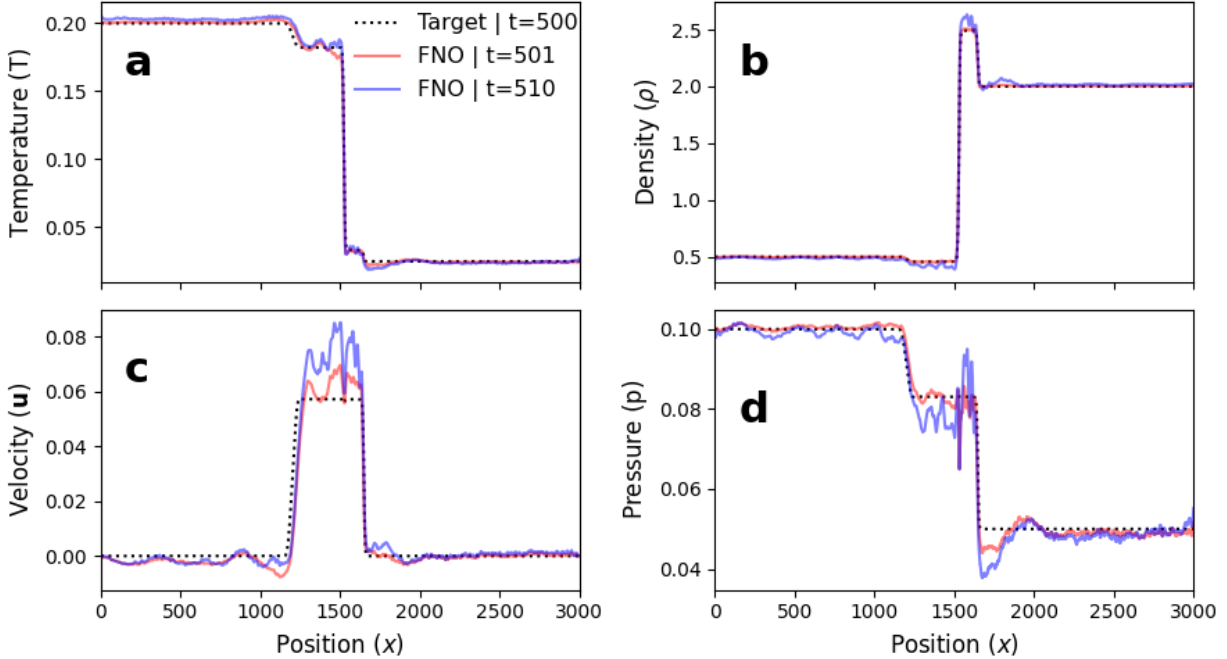


**Figure 14:** We train and evaluate the FNO model on the subsonic Sod shock tube with 512 Fourier modes, 256 embedding dimensions, and 8 layers. We evaluate (a) Temperature, (b) Density, (c) Velocity, and (d) Pressure for only 1 and 10 time steps.

contrast to LB+NeurDE’s ability to accurately resolve the discontinuity for 500 time steps (Fig (a-d) 3), FNO shows significant deviations after a single time step. This is expected as shocks are very challenging for any model, often requiring special methods to address them.

We provide the MSE on the test dataset for all of our trained models in Table 3. As expected—and visualized in Figs. 12 to 14—we observe improved accuracy as the number of Fourier modes increases. Unfortunately, the model’s memory scaling as a function of the number of Fourier modes inhibits us from exploring further. Regardless, the model’s size with 512 Fourier modes limits its practicality given this level of accuracy.

## E.2 Transonic Shock Tube Case (from Subsec. 2.3.1)

This subsection provides additional details for the transonic Sod shock tube case (Eq. (11)). Unlike the subsonic configuration, the transonic Sod shock tube exhibits pronounced oscillatory behavior, highlighting the increased numerical difficulty of this regime. These oscillations are shown in Fig. 15a. As discussed in the main text, this case poses a greater challenge than Eq. (10) and therefore requires additional regularization to suppress the oscillations.

To address the artifacts observed in Fig. 15a, we incorporate a total variation diminishing (TVD) regularization term, detailed in Subsec. E.2.1, with the corresponding modified algorithm presented in Algorithm 2, see Subsec. E.2.3. To confirm the near-sonic nature of this setup, Subsec. E.2.4 visualizes the local Mach number at lattice time  $t = 700$ . Subsec. E.2.5 provides an error analysis of the polynomial equilibrium approximation in this flow regime, motivating the exclusion of the LB+NeurDE baseline in Fig. 3(e – h). Finally, Subsec. E.2.6 illustrates model degradation under different initialization times, complementing the long-horizon stability analysis discussed in Subsec. 2.4.1.

### E.2.1 Training with Regularization by the Total Variation Diminishing Principle

To mitigate numerical oscillations, particularly in regions with steep gradients, we incorporate a TVD into the training. This is a highly desirable property, as scalar conservation laws in one dimension inherently satisfy a total variation bound, thus fulfilling the TVD condition [31]. To enforce the TVD constraint (see Eq. (57)) for any observable  $\mathbf{U}$  of interest, we utilize the  $\text{relu}(\cdot)$  function, leading to the following regularizer:

$$\text{relu}(\text{TV}(\mathbf{U}(t+1, \cdot)) - \text{TV}(\mathbf{U}(t, \cdot))). \quad (56)$$

In Subsec. E.2.2, we briefly review key concepts of the TVD principle, following Harten [31]. The training algorithm is modified to incorporate this regularizer, as detailed in Subsec. E.2.3. Finally, in Fig. 15, see Subsec. E.2.3, we demonstrate the impact of the TVD regularization on the temperature profile at time  $t = 700$ .

### E.2.2 Total Variation Diminishing Principle

Consider a function  $w(t, x)$ , and an operator  $L$  tied to a numerical scheme such that  $w(t_{n+1}, x) = Lw(t_n, x)$  (e.g.,  $L$  could be a point finite-difference scheme). The specific nature of the domain, the operator  $L$ , and associated conditions play a negligible role in what follows, and so they will remain unspecified.

A scheme is considered TVD, if for any function  $w(t, x)$  of bounded total variation, the following inequality holds:

$$\text{TV}(Lw) \leq \text{TV}(w), \quad (57)$$

where,

$$\text{TV}(w(t_n, \cdot)) = \sum_{j=-\infty}^{\infty} |w(t_n, x_{j+1}) - w(t_n, x_j)|.$$

TVD is a highly desirable property because scalar conservation laws in one dimension inherently satisfy a total variation bound, thereby fulfilling the TVD condition as expressed in Eq. (57), see [31, theorem 2.1].

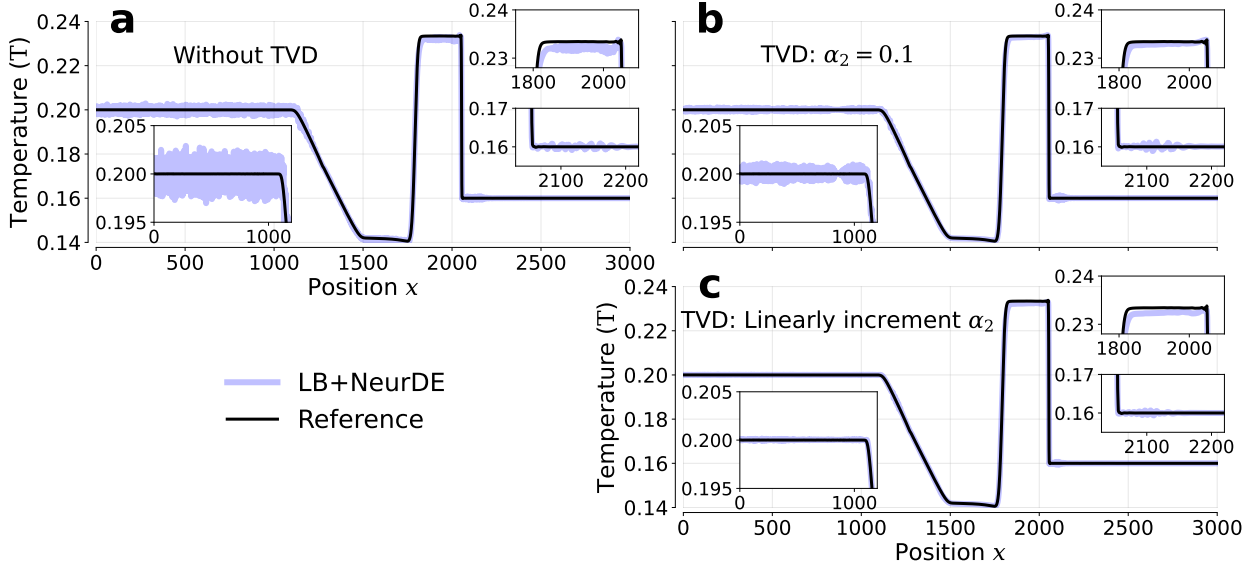


**Figure 15:** Improvements in LB+NeurDE temperature profile predictions through the inclusion of TVD regularization during training. Panel a shows the LB+NeurDE performance without TVD regularization. Panel b shows the LB+NeurDE performance when TVD regularization is included and weighted by a constant  $\alpha_2$ , see Algorithm 2. Panel c shows the LB+NeurDE performance when TVD regularization is included with a linearly incremented weight for  $\alpha_2$ . The black line represents the numerical simulation, and the blue line represents the LB+NeurDE prediction. These snapshots are taken at  $t = 700$ .

### E.2.3 Adding the TVD in the Training Algorithm

Here, for the sake of completeness, we present the modification of Algorithm 1 to incorporate TV regularization. For simplicity, we demonstrate the algorithm for a single population  $\mathbf{h}_i \in \{\mathbf{f}_i, \mathbf{g}_i\}$ .

---

**Algorithm 2:** Second stage of training  $\Phi_S \Phi_C^{\text{NN}}$  with TV regularizer.

---

```

Data:  $\tau, \{\mathbf{c}_i\}_{i=1}^Q, \{W_i\}_{i=1}^Q, \alpha \in [0, 1], \alpha_2, \eta, N_r$ 
{1}  $\theta \leftarrow \text{pretraining}(\theta \sim \text{random});$  // Perform pre-training
{2}  $\{\{\mathbf{h}(0, \mathbf{x}), \mathbf{h}^{\text{eq}}(0, \mathbf{x})\}, \dots, \{\mathbf{h}(t_{N_{\text{train}}}, \mathbf{x}), \mathbf{h}^{\text{eq}}(t_{N_{\text{train}}}, \mathbf{x})\}\};$  // Load trajectories
{3} for  $0 \leq \text{epoch} \leq N$  do
{4}   for  $0 \leq t \leq t_{N_{\text{train}}}$  do
{5}      $t_{\text{end}} = \min(t_{N_{\text{train}}}, t + N_r);$ 
{6}      $\mathbf{H}_{\text{hist}}^{\text{pred}}, \mathbf{H}_{\text{hist}}^{\text{eq}} = LB\_NDEQ(t, t_{\text{end}}, \mathbf{M}[\mathbf{h}](t, \mathbf{x}));$  // Make temporal prediction
{7}      $L \leftarrow \sum_{r=t}^{t_{\text{end}}} \alpha \ell(\mathbf{h}(r, \mathbf{x}), \mathbf{H}_{\text{hist}}^{\text{pred}}[r, \mathbf{x}]) + \alpha' \ell(\mathbf{h}^{\text{eq}}(r, \mathbf{x}), \mathbf{H}_{\text{hist}}^{\text{eq}}[r, \mathbf{x}]);$  // Accumulate loss
{8}      $L \leftarrow \sum_{r=t+1}^{t_{\text{end}}} \alpha_2 \text{relu}(\text{TV}(\mathbf{M}[\mathbf{H}_{\text{hist}}^{\text{eq}}[r, \mathbf{x}]] - \text{TV}(\mathbf{M}[\mathbf{H}_{\text{hist}}^{\text{eq}}[r-1, \mathbf{x}]]));$  // regularizer
{9}      $\theta \leftarrow (\theta - \eta \partial_{\theta} L);$  // Update the parameters
{10}     $t \leftarrow t + 1;$ 
{11}  end
{12}   $\text{epoch} \leftarrow \text{epoch} + 1;$ 
{13} end
Output:  $\phi^{\text{NN}}(\cdot; \theta)$ 

```

---

We see that Algorithm 2 is similar to Algorithm 1, with the main differences in Line 8 of Algorithm 2, where the TVD condition is added. Specifically, for our applications, the condition in Eq. (57) becomes:

$$\text{TV}(\mathbf{U}(t, \mathbf{x})) \leq \text{TV}(\mathbf{U}(t-1, \mathbf{x})).$$

The inequality is soft-enforced by using the `relu` function, as shown in Eq. (56). We note that while [64, eq. 11] suggests using  $(\text{relu}(\text{TV}(Lw) - \text{TV}(w)))^2$  as the regularizer, we found that this did not significantly improve the results in our numerical experiments. Indeed, the results obtained with this alternative regularization were found to be indistinguishable from those obtained with Eq. (56) in terms of solution accuracy and model performance. More generally, any regularizer of the form:

$$\|\text{relu}(\text{TV}(Lw) - \text{TV}(w))\|,$$

could potentially be explored, although our preliminary investigations did not reveal significant gains with this more general class of regularizers.

**Effects of TVD on shock tube case 2.** After incorporating TVD regularization, we observe in Fig. 15b and Fig. 15c that the oscillations present in Fig. 15a are dampened or eliminated. Our results indicate that the application of TVD is beneficial, but the scaling of the regularization parameter is crucial to fully mitigate the oscillations that are observed in the absence of regularization. Specifically, we found that a linear TVD schedule successfully suppresses these oscillations. An adaptive approach allows the model to explore a broader solution space initially, before progressively imposing stricter constraints, thus achieving a balance between flexibility and stability.

### E.2.4 Local Mach Number Transonic Case

In Fig. 16, we present a comparison between the predicted local Mach number,  $\text{Ma}$  (blue), and the reference value (in black). This analysis is based on LB+NeurDE trained with TVD. Assuming an ideal gas, the local Mach number is calculated using  $\text{Ma} = (\mathbf{u} \cdot \mathbf{u})^{1/2} (\gamma RT)^{-1/2}$  (see, Subsec. 2.3.2), consistent with the method used in the previous case. We observed that the flow in the tube approaches  $\text{Ma} = 1$ . This near-sonic condition is particularly challenging for D2Q9 lattices, highlighting the robustness of our model. Compare this with the simpler subsonic case presented in Subsec. E.1.1.

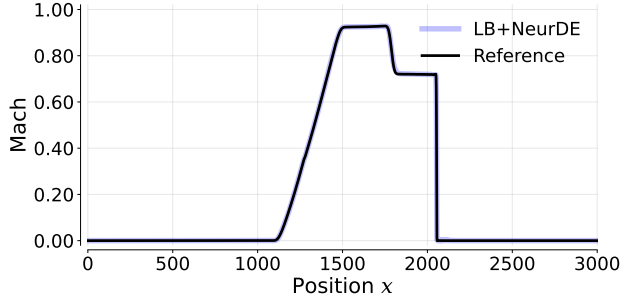


**Figure 16:** Comparison of the local *Mach* number for the near-sonic Sod shock tube (case 2 Eq. (11)) between LB+NeurDE and simulation results. The black line represents the numerical reference, while the blue line depicts the flow predicted by LB+NeurDE trained with TVD. This snapshot is taken at time-step 700. We observe that the local Mach number of the tube is close to  $\text{Ma} = 1$  at around  $x = 1500$ .

### E.2.5 Errors of the Polynomial for the Transonic Case

Quantitatively, after just seven time steps, we observed:  $\|\mathbf{R}_{\alpha,\alpha}^{\text{eq,poly}} - \mathbf{R}_{\alpha,\alpha}^{\text{MB}}\|_{\text{L}^2} \geq \mathcal{O}(10^2)$  for  $\alpha \in \{x, y\}$ ; see Table 4. This large discrepancy in the higher-order moments rendered a meaningful comparison between our model and the polynomial equilibrium approach infeasible, highlighting the challenges in maintaining stability for high-speed flows using polynomial's equilibrium. Moreover, it shows that the operator network in Eq. (6) plays a crucial role in the simulation.

Iteration:	1	2	3	4	5	6	7
$\ \mathbf{R}_{x,x}^{\text{eq,poly}} - \mathbf{R}_{x,x}^{\text{MB}}\ _{\text{L}^2}$	0.09163	0.1284	0.1508	0.1667	0.1790	6.554	24354.799
$\ \mathbf{R}_{y,y}^{\text{eq,poly}} - \mathbf{R}_{y,y}^{\text{MB}}\ _{\text{L}^2}$	0.0063	0.0048	0.0025	0.0005	0.0007	0.095	473.0
$\ \mathbf{R}_{x,x}^{\text{eq,NN}} - \mathbf{R}_{x,x}^{\text{MB}}\ _{\text{L}^2}$	$(1.458)10^{-4}$	$(1.454)10^{-4}$	$(1.447)10^{-4}$	$(1.454)10^{-4}$	$(1.450)10^{-4}$	$(1.453)10^{-4}$	$(1.452)10^{-4}$
$\ \mathbf{R}_{y,y}^{\text{eq,NN}} - \mathbf{R}_{x,x}^{\text{MB}}\ _{\text{L}^2}$	$(2.823)10^{-3}$	$(2.8277)10^{-3}$	$(2.822)10^{-3}$	$(2.8249)10^{-3}$	$(2.8219)10^{-3}$	$(8.228)10^{-3}$	$(2.821)10^{-3}$

**Table 4:** The  $\text{L}^2$ -norm errors between the polynomial equilibrium (Eq. (53)) and the Maxwellian higher-order moments (Eq. (32)) for the Sod case 2 (Eq. (11)). The use of polynomial equilibrium in both populations exhibits significant errors that lead to simulation instability after just seven time-steps. Compared the results with Levermore's moment system and LB+NeurDE the hybrid model Fig. 3(e – h).

The comparison in Table 4 is based on the initial snapshot of the simulation, indicating the model's ability to represent the correct distribution rather than its generalization capabilities. Unfortunately, an assessment at time-step 700 (in lattice units) is not possible due to the instability of the polynomial LB scheme.

### E.2.6 Model Failure (cf. Subsec. 2.4.1)

In the transonic shock tube case (Eq. (11)), which is more challenging than case 1, LB+NeurDE fails when initialized at  $t_0 = 2500$  and propagated for 100 time-steps. The failure manifests as large oscillations in all macroscopic variables, particularly at the right-hand side of the domain. This is shown in Fig. 17. These oscillations begin to appear around 75 time-steps ahead of the initialization ( $t_0 = 2500$ ), as shown in Fig. 18, increasing abruptly after 2575, as indicated in Fig. 17.

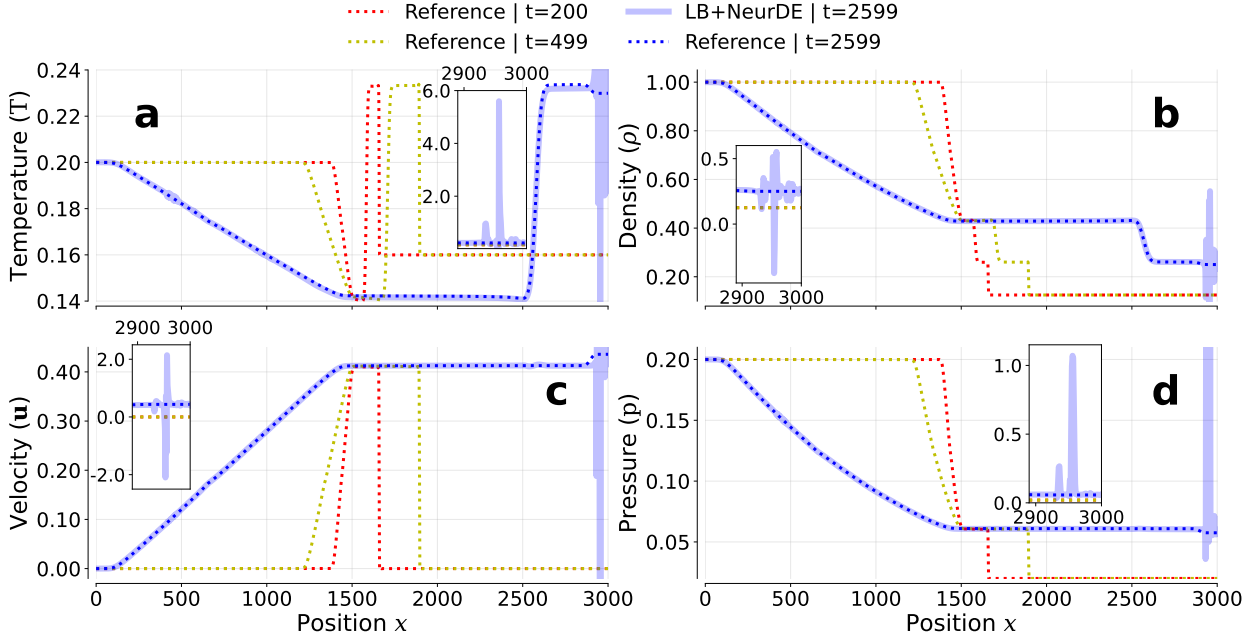


**Figure 17:** LB+NeurDE’s failure on the near-sonic Sod shock tube when predicting the  $t = 2599$  time-step after being initialized at  $t_0 = 2500$ . The solid blue line represents the LB+NeurDE prediction and the dotted lines represent simulated results at different times. We show the *temperature*, *density*, *velocity*, and *pressure* variables in panels a, b, c, and d, respectively.

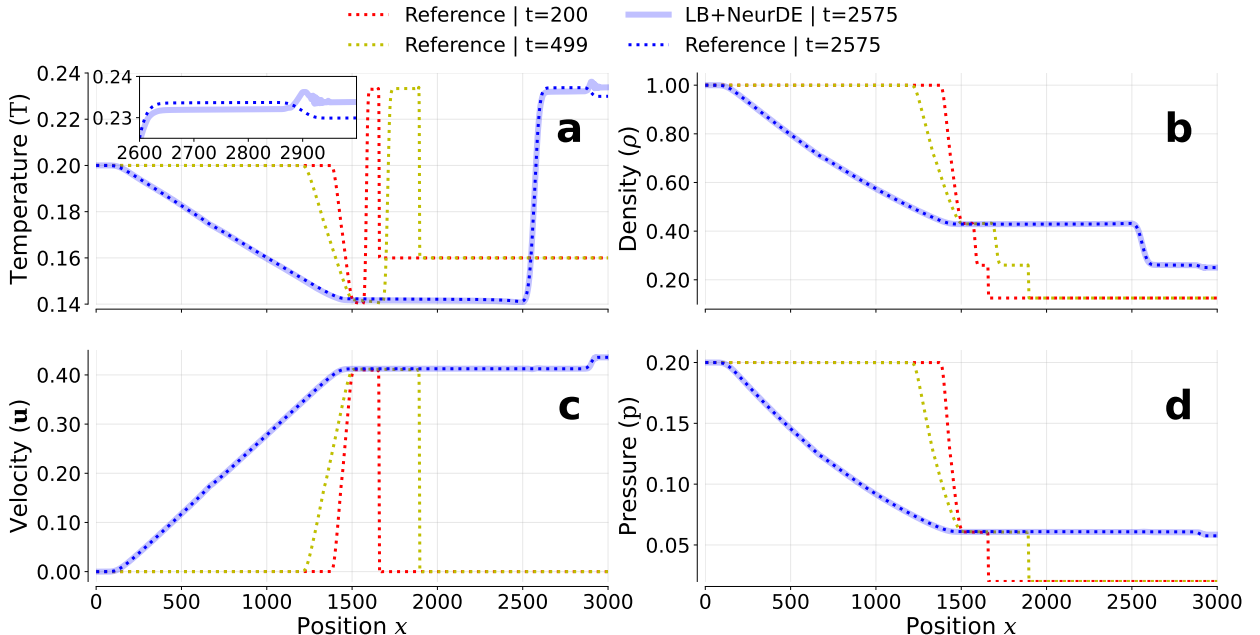


**Figure 18:** The onset of LB+NeurDE’s failure on the near-sonic Sod shock tube when predicting the  $t = 2575$  time-step after being initialized at  $t_0 = 2500$ . The solid blue line represents the LB+NeurDE prediction and the dotted lines represent simulated results at different times. We show the *temperature*, *density*, *velocity*, and *pressure* variables in panels a, b, c, and d, respectively.

## F Ablation Study: Surrogate Models for Collision and Streaming

In this appendix, we present *ablation studies* examining the role of ML surrogates within the *splitting operator formulation* described in Eqs. (33a) and (33b). Specifically, we assess the effect of replacing either the collision operator  $\Phi_C$  or the streaming operator  $\Phi_S$ —or both—with learned models, as motivated by the decomposition of the lattice Boltzmann (LB) scheme in Eq. (5) (cf. Eqs. (5a) and (5b)). Each experiment isolates a component of the LB update to quantify the impact of learned surrogates relative to the baseline physics-based formulation.

In the main study, LB+NeurDE replaces only the equilibrium mapping within the collision operator. By contrast, several recent works have explored broader uses of ML in kinetic theory by substituting the entire collision operator with neural approximations [61, 85, 86, 18]. Here, we systematically extend this idea by testing both operators. Our goal is to elucidate the individual contributions of each operator to overall stability, accuracy, and physical consistency.

We focus on the compressible, subsonic Sod shock tube configuration (see Eq. (10)), extending the parameter range beyond the optimal LB conditions explored in prior studies [18]. Section F.1 implements the surrogate-collision framework of [18], both with and without explicit enforcement of conservation laws and symmetry constraints. Section F.2 then investigates a neural surrogate for the streaming operator  $\Phi_S$ , following the approach of [45]. Together, these experiments provide a comparative perspective on how learned operators can augment—or destabilize—classical kinetic solvers for compressible flows.

### F.1 Surrogate Model for Collision ( $\Phi_C$ )

Among the approaches that fully replace the collision operator with ML models, the work of Corbetta et al. [18] is particularly noteworthy. They substituted the BGK collision operator with a surrogate neural architecture for weakly compressible isothermal flows—regimes well aligned with standard LB formulations. By explicitly incorporating physical constraints such as conservation laws and lattice symmetries into the neural architecture, they achieved notable accuracy improvements. However, their results were primarily obtained under conditions optimized for the LB method, potentially limiting their applicability to broader or higher-speed regimes.

Here, we compare our formulation of the equilibrium state (Eq. (6)) with the surrogate collision approach of [18]. In Subsec. F.1.1, we summarize their symmetry and conservation strategy. In Subsec. F.1.2 and Subsec. F.1.3, we provide the corresponding training details and simulation results for the subsonic shock tube case. Finally, Subsec. F.1.4 presents the results obtained after removing the symmetry and conservation constraints imposed in [18].

#### F.1.1 Enforcing Symmetry and Conservation as in Corbetta et al. [18]

Corbetta et al. [18] parameterized the entire collision operator using a symmetry- and conservation-preserving multi-layer perceptron (MLP), hereafter denoted as  $\text{MLP}_{\text{cons}}^{\text{sym}^+}(\cdot; \theta)$ . As discussed in Subsec. B.1 (cf. [51]), the collision operator  $\mathcal{C}(\cdot)$  satisfies three key physical principles: (i) local conservation of mass, momentum, and energy (Eq. (13)); (ii) the local dissipation law implied by Boltzmann’s H-theorem (Eq. (15)); and (iii) symmetry, including rotational and translational equivariance (Eq. (16)).

To ensure that  $\text{MLP}_{\text{cons}}^{\text{sym}^+}(\cdot; \theta)$  inherits the correct symmetries, Corbetta et al. [18] employed group averaging over the dihedral group  $D_8$ , which captures rotations and reflections of the D2Q9 lattice. This yields a modified collision surrogate  $\overline{\Phi_C}$  that satisfies the symmetry properties by construction. That is (cf., [18, eq. 21]),

$$\overline{\Phi_C^{\text{NN}}}(\mathbf{f}_i) = \frac{1}{|D_8|} \sum_{\sigma \in D_8} \sigma^{-1} \Phi_C^{\text{NN}}(\sigma \mathbf{f}_i).$$

They further introduced linear transformations  $\mathbf{A}$  and  $\mathbf{B}$  to ensure mass and momentum conservation (energy was not explicitly enforced). The resulting post-collision distribution is then given by

$$\mathbf{h}_i^{\text{coll}} = \Phi_C^{\text{NN}}(\mathbf{h}_i) = \mathbf{A} \mathbf{h}_i + \mathbf{B} \overline{\Phi_C^{\text{NN}}}(\mathbf{h}_i), \quad (58)$$

where  $\mathbf{h}_i \in \{\mathbf{f}_i, \mathbf{g}_i\}$ , and

$$\mathbf{A} = \begin{pmatrix} 0 & 0 & 0 & 0 & 0 & 0 & 0 & 0 & 0 \\ 0 & 0 & 0 & 0 & 0 & 0 & 0 & 0 & 0 \\ 1 & 0 & 1 & 2 & 1 & 0 & 2 & 2 & 0 \\ 0 & 0 & 0 & 0 & 0 & 0 & 0 & 0 & 0 \\ 0 & 0 & 0 & 0 & 0 & 0 & 0 & 0 & 0 \\ -\frac{1}{2} & \frac{1}{2} & 0 & -\frac{3}{2} & -1 & 1 & -1 & -2 & 0 \\ 0 & 0 & 0 & 0 & 0 & 0 & 0 & 0 & 0 \\ 0 & 0 & 0 & 0 & 0 & 0 & 0 & 0 & 0 \\ \frac{1}{2} & \frac{1}{2} & 0 & \frac{1}{2} & 1 & 0 & 0 & 1 & 1 \end{pmatrix}, \quad \mathbf{B} = \begin{pmatrix} 1 & 0 & 0 & 0 & 0 & 0 & 0 & 0 & 0 \\ 0 & 1 & 0 & 0 & 0 & 0 & 0 & 0 & 0 \\ -1 & 0 & 0 & -2 & -1 & 0 & -2 & -2 & 0 \\ 0 & 0 & 0 & 1 & 0 & 0 & 0 & 0 & 0 \\ 0 & 0 & 0 & 0 & 1 & 0 & 0 & 0 & 0 \\ \frac{1}{2} & -\frac{1}{2} & 0 & \frac{3}{2} & 1 & 0 & 1 & 2 & 0 \\ 0 & 0 & 0 & 0 & 0 & 0 & 1 & 0 & 0 \\ 0 & 0 & 0 & 0 & 0 & 0 & 0 & 1 & 0 \\ -\frac{1}{2} & -\frac{1}{2} & 0 & -\frac{1}{2} & -1 & 0 & 0 & -1 & 0 \end{pmatrix}.$$

Although these transformations are not unique, they guarantee that the surrogate operator satisfies the required conservation constraints without additional loss terms.

### F.1.2 Training Details

Both LB+NeurDE and the  $\text{MLP}_{\text{cons}}^{\text{sym}+}$  surrogate were trained on the same dataset consisting of the first 500 time steps, using the two-stage training procedure described in Subsecs. 2.2 and C.5 with  $N_r = 25$ . Optimization details follow those in Subsec. D.4. A direct comparison of architectures and hyperparameters is provided in Table 5.

To ensure a fair comparison, both LB+NeurDE and the hybrid surrogate from [18] are trained on the same dataset, comprising the first 500 time-steps. They both use the same two-stage training procedure described in Subsec. C.5, with  $N_r = 25$ , and optimization algorithm, as described in Subsec. D.4. A side-by-side comparison of the training configurations and key hyperparameters for both models is shown in Table 5.

	Input	Output	Activation	Loss	Layer Size	Model Size
Ours	$(\rho, \mathbf{u}, T)^\top$ $\{\mathbf{c}_i\}_{i=1}^9$	$\mathbf{h}_i^{\text{eq}}$	relu	MSE	4x32, 32x32, 32x32, 32x32 9x32, 32x32, 32x32, 32x32	6784
Model in [18]	$\mathbf{h}_i$	$\mathbf{h}_i^{\text{coll}}$	relu	MSE	9x50, 50x50, 50x50, 50x9	6059

**Table 5:** Comparison of model hyperparameters and sizes for LB+NeurDE and the surrogate from [18].

Our model takes as input the macroscopic observables  $(\rho, \mathbf{u}, T)^\top$  and lattice velocities  $\{\mathbf{c}_i\}_{i=1}^9$ , while the surrogate of [18] uses the pre-collision populations  $\mathbf{h}_i$ . Both models predict the post-collision distribution  $\mathbf{h}_i^{\text{coll}}$  using relu activations and a mean-squared error (MSE) loss.

### F.1.3 Comparison of Results between LB+NeurDE and the $\text{MLP}_{\text{cons}}^{\text{sym}+}$ Surrogate

The  $\text{MLP}_{\text{cons}}^{\text{sym}+}$  model exhibits numerical instability arising from error accumulation, leading to unphysical temperature values ( $T < 0$ ) around time-step 550 (Fig. 19a). The relative  $L^2$ -norm error (Fig. 19b) increases by several orders of magnitude within just 25 iterations. This instability can be traced to the algebraic correction defined in [18, Eq. 27] (cf. Eq. (58)), which—while ensuring mass and momentum conservation—introduces negative post-collision populations  $\mathbf{g}_i^{\text{coll}}$ , particularly in high-Mach regimes where temperature fluctuations are strong.<sup>6</sup>

<sup>6</sup>When the temperature exceeds the range supported by the lattice, negative populations can emerge, leading to numerical instability.

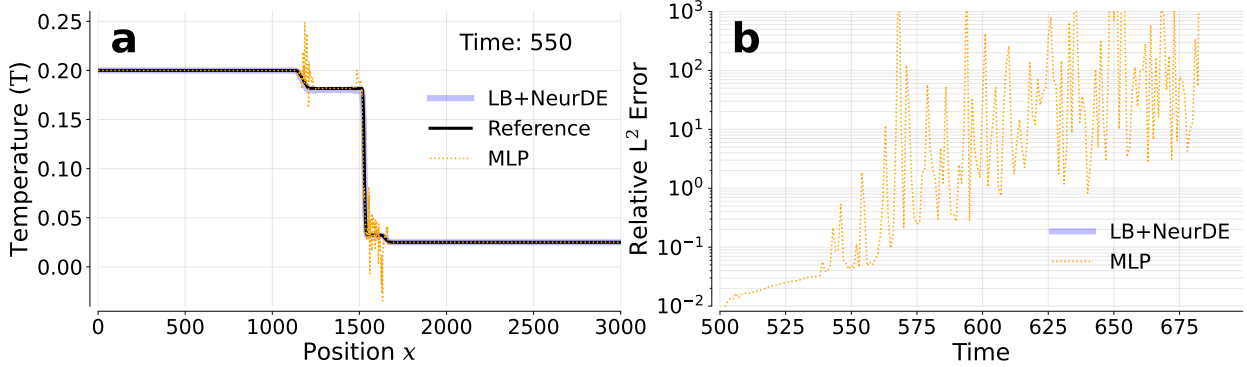


**Figure 19:** Comparison of the *temperature* predictions for Sod case 1 between LB+NeurDE,  $\text{MLP}_{\text{cons}}^{\text{sym}+}$ , and the numerical simulation for time-step 550. Here, both LB+NeurDE and  $\text{MLP}_{\text{cons}}^{\text{sym}+}$  are initialized at  $t_0 = 500$ . Panel a shows the predicted temperature; and panel b shows its relative  $L^2$ -norm error with respect to the numerical simulation at different time-steps. The blue line represents LB+NeurDE, the black line represents the numerical reference, and the dotted orange line represents  $\text{MLP}_{\text{cons}}^{\text{sym}+}$ .

#### F.1.4 Without Algebraic Correction

To improve the  $\text{MLP}_{\text{cons}}^{\text{sym}+}$  surrogate, we removed the algebraic correction layer, see Eq. (58), from the model in [18]. This modification compromised energy conservation (requiring a soft constraint), but it guaranteed a non-negative post-collision distribution,  $\mathbf{g}_i^{\text{coll}}$ . As shown in [18, fig.5], omitting this algebraic correction results in suboptimal simulation outcomes for the Taylor-Green vortex. However, in the specific regime studied here, we observed initial improvement in short-time predictions, compared with Subsec. F.1.3, but the simulation still diverged into an unphysical result.

Compared to the result obtained with the algebraic correction (Eq. (58) and shown in Fig. 19), this approach initially improved stability during 50 time-steps, as illustrated in Fig. 20a. However, at longer time-steps (up to the time-step 675 time steps), a negative temperature value emerges, as shown in Fig. 20c. In Fig. 20b, we can see some numerical artifacts that start appearing in the simulation. This led to a significant increase in relative error, as depicted in Fig. 20d.

Upon inspection, the negative temperature result arises from an unphysical condition where the total energy density of the system,  $\rho E = \langle \mathbf{g}_i/2 \rangle$ , is smaller than the kinetic energy,  $\rho \mathbf{u} \cdot \mathbf{u}/2$ . This leads to instabilities, as:

$$0 > T = \frac{1}{C_v} \left( E - \frac{\mathbf{u} \cdot \mathbf{u}}{2} \right), \quad \text{given that} \quad \rho E < \rho \frac{\mathbf{u} \cdot \mathbf{u}}{2}.$$

The authors of [18] acknowledged this problem and proposed an alternative approach by employing soft constraints. However, we believe that a more robust approach for compressible flows could be achieved by directly enforcing the positivity of the post-collision population, as demonstrated in [78]. This approach, using exponential distributional functions, offers a direct and effective means of ensuring positivity. However, it would necessitate formulating and solving a constrained optimization problem for the post-collision distribution, similar to Levermore's moment system closure.

## F.2 Surrogate Model for $\Phi_s$

Here, we investigate the effectiveness of our translation based  $\Phi_s$  operator Eq. (35) by replacing it with a surrogate neural network. There are many potential models that propagate, or forecast, dynamical systems, including Transformers [62, 84, 88, 54] and ResNets. The latter have been generally shown to have interesting connections with dynamical systems [14, 87] and ODE solvers [15, 45]. Such models can become fairly large and difficult to interpret, which are misaligned with our physics-based approach that leverages much of the mathematical structure of the kinetic formulation. Consequently, we use the so-called “*ContinuousNet*” model [45], which incorporates numerical integration techniques within the training and evaluation, as our streaming surrogate.

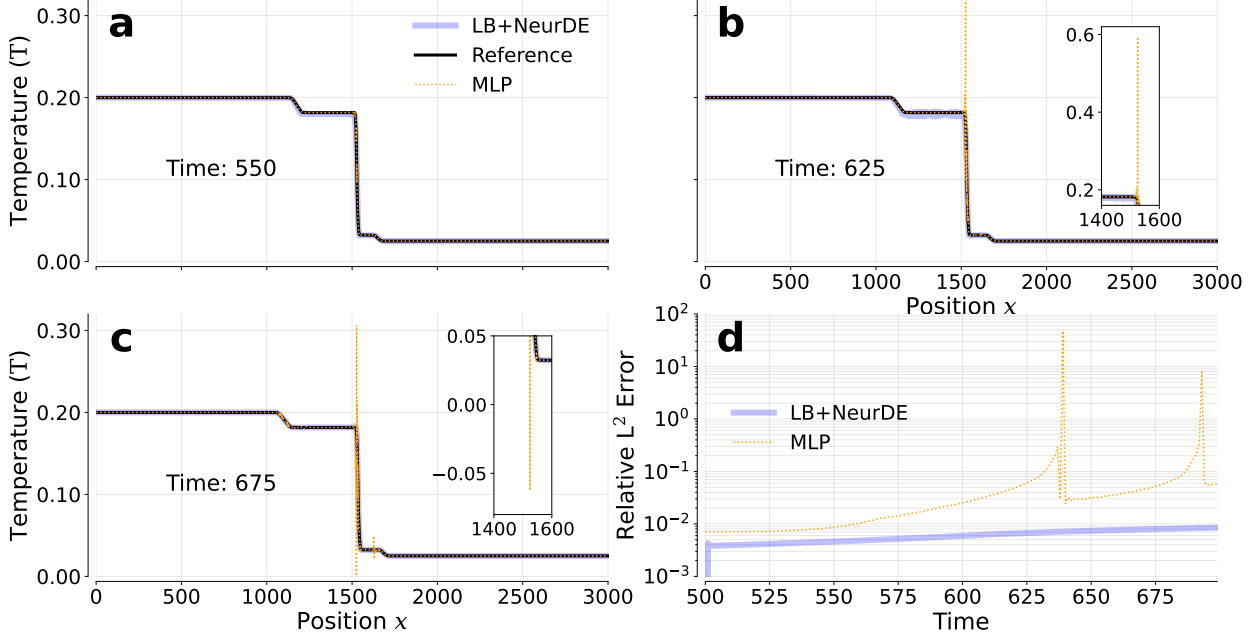


**Figure 20:** Comparison of the evolving *temperature* predictions for Sod case 1 between LB+NeurDE,  $\text{MLP}_{\text{cons}}^{\text{sym}+}$ , without the algebraic correction, and the numerical simulation for time-step 550, 625, and 675, in panels a, b, and c, respectively. Here, both LB+NeurDE and  $\text{MLP}_{\text{cons}}^{\text{sym}+}$  are initialized at  $t_0 = 500$ . Panel d shows the relative  $L^2$ -norm error with respect to the numerical simulation as a function of prediction time. The blue line represents LB+NeurDE, the black line represents the numerical reference, and the dotted orange line represents  $\text{MLP}_{\text{cons}}^{\text{sym}+}$  without the algebraic correction.

In Subsec. F.2.1, we provide an overview of *ContinuousNet* and how we incorporate this approach into the streaming. In Subsec. F.2.2, we describe our training procedure and setup for our experiment. In Subsec. F.2.3, we present the numerical results.

### F.2.1 Temporal Streaming through *ContinuousNet*

*ContinuousNet* [45] is a model that predicts continuous-in-time solutions to ODEs by incorporating numerical integration schemes within the model. Specifically, *ContinuousNet* uses a neural network to calculate the time derivative of the solution to the ODE ( $\partial_t \mathbf{h}_i$ ). *ContinuousNet* then evolves the function  $\mathbf{h}_i(t, \mathbf{x})$  to  $\mathbf{h}_i(t + \Delta t, \mathbf{x})$  using (explicit) numerical integration schemes, like Euler or Runge Kutta, which use the predicted  $\partial_t \mathbf{h}$ . In this experiment, we use the forward Euler method as the ODE solver (although we note the point of *ContinuousNet* is that higher-order schemes in the ODE solver typically perform better). This *ContinuousNet*-surrogate approach leverages the strengths of numerical integration schemes, making it methodologically well-aligned with our physics-based LB approach.

Ultimately, *ContinuousNet* learns the mapping from the distribution of current post-collision state,  $\mathbf{h}_i^{\text{coll}}$ , to future pre-collision  $N$  states. That is,

$$\{\mathbf{h}_i(t_{n+1}, \mathbf{x}), \mathbf{h}_i(t_{n+2}, \mathbf{x}), \dots, \mathbf{h}_i(t_{n+N}, \mathbf{x})\} = \text{ContinuousNet}(\mathbf{h}_i^{\text{coll}}(t_n, \mathbf{x}); \theta).$$

The equilibrium distribution for the collision  $\Phi_C$  in Eq. (8) uses the  $\mathbf{f}_i^{\text{eq}}$ , and  $\mathbf{g}_i^{\text{eq}}$ , as described previously in Eqs. (52) and (54).

This *ContinuousNet* surrogate model is evaluated by first applying collision operation to the model's prediction at  $t_{n+N}$ , and then using this result as an input to the *ContinuousNet* model. This process is repeated autoregressively to extend the predictions over longer time steps; see Algorithm 3. The collision operator used during testing is identical to the one employed for data generation (Eqs. (52) and (54)).

---

**Algorithm 3:** Replacing the entire streaming operator.

---

```

{1}  $N \leftarrow 25$ ;  $s \leftarrow t$ ;
{2} while  $0 \leq r < N_{end}$  do
{3}    $\mathbf{h}_i^{\text{eq}}(s, \mathbf{x}) \leftarrow \phi_i(M\mathbf{h}_i(s, \mathbf{x}); \theta)$ ; // equilibrium Eqs. (52) and (54));
{4}    $\mathbf{h}_i^{\text{coll}} \leftarrow \Phi_C(\mathbf{h}_i, \mathbf{h}_i^{\text{eq}})$ ; //Collision;
{5}    $\left\{ \mathbf{h}_i^{\text{pred}}(s + \Delta t, \mathbf{x}), \mathbf{h}_i^{\text{pred}}(s + 2\Delta t, \mathbf{x}), \dots, \mathbf{h}_i^{\text{pred}}(s + N\Delta t, \mathbf{x}) \right\} \leftarrow \text{ContinuousNet}(\mathbf{h}_i^{\text{coll}}(s, \mathbf{x}); \theta)$ ; ;
{6}    $s \leftarrow s + N\Delta t$  ;
{7}    $r \leftarrow r + 1$ ; //Increment  $r$ ;
{8}    $\mathbf{h}_i \leftarrow \mathbf{h}_i^{\text{pred}}$ ; //Getting  $\mathbf{h}_i$  prediction;
Output:  $\{\mathbf{h}_i(t, \mathbf{x}), \dots, \mathbf{h}_i(t_n, \mathbf{x}), \dots, \mathbf{h}_i(t_{N_{end}+N}, \mathbf{x})\}$ 

```

---

### F.2.2 Training Details

The model is trained on the same dataset as previously discussed in Subsec. F.1.2. However, we opted not to employ a two-stage training strategy for this streaming operator due to the recursive nature of the *ContinuousNet* model. This design allows for efficient training without compromising performance. For a fair comparison with our model, which is trained using a two-stage strategy, we set the predictive sequence length to  $N = 25$ , consistent with  $N_r = 25$  (Algorithm 1). Once the model is trained, we evaluate the model performance on longer sequence.

### F.2.3 Numerical Results

As illustrated in Fig. 21, the overall model (the Euler variant) exhibits significant inaccuracies in the temperature prediction, while the density prediction is relatively well-behaved, with the exception of the boundary values. Specifically, the model fails to accurately represent both the rarefaction wave and the shock wave in the temperature simulation. Notably, in the temperature field, the shock wave is entirely absent from the model’s output. These findings are not unexpected when we consider the fundamental linearity of the streaming operation in the kinetic framework (cf., Fig. 21). The streaming operator is essentially a linear operation. It shifts discrete distributions  $\mathbf{h}_i(t, \mathbf{x})$  along fixed, pre-defined lattice velocities without requiring iterative solvers or nonlinear processing. By replacing this exact mechanism with a learned neural surrogate, we introduce unnecessary complexity and parameterization.

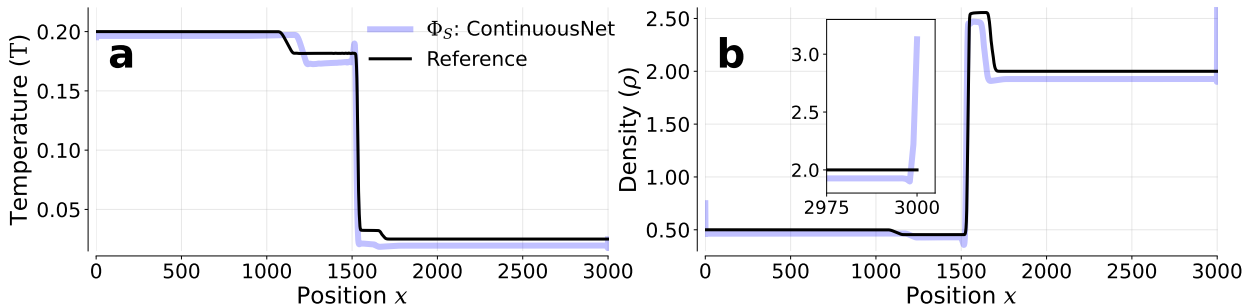


**Figure 21:** The *temperature* comparison between the *ContinuousNet* surrogate model and numerical simulation for the subsonic Sod shock tube (case 1 Eq. (10)). The results are presented at time-step 650 which is 150 time-steps beyond training data. The blue line represents the *ContinuousNet* surrogate model and the black line represents the simulation.

## G 2D Supersonic Flow

This appendix provides supplementary information for the simulation of supersonic flow around a circular cylinder, as introduced in Subsec. 2.3.2. The computational domain is a rectangular region of size  $(15r, 25r)$ , with the cylinder of radius  $r = 20$  centered at  $(166, 149)$ .

Here, we present the remaining macroscopic observables—temperature, density, speed, and pressure—that were omitted from the main text for brevity. Subsec. G.1 shows these fields for the case where LB+NeurDE is trained on the first 500 time steps. In this configuration, the model is initialized at  $t_0 = 500$  and evaluated autoregressively over the subsequent 200 time steps. Subsec. G.2 presents analogous results for the long-horizon experiment presented in Subsec. 2.4, in which LB+NeurDE is trained on only the first 150 time steps (as described in Subsec. 2.4.2) and tested from the initial condition at  $t_0 = 900$  to predict the following 100 time steps.

### G.1 Prediction Results for Training on the First 500 Time-Steps

We present further macroscopic results for the 2D cylinder under the same experimental constraints as Subsec. 2.3.2). LB+NeurDE is trained on the first 500 time-steps and then predicts 200 time-steps into the future after being initialized at  $t_0 = 500$ . When comparing the predictions at  $t = 700$ , depicted in Figs. 22 to 27, we see LB+NeurDE and the reference model exhibit strong agreement in their representations. We observe slight deviations near the right boundary of the outlet as highlighted in the insets.

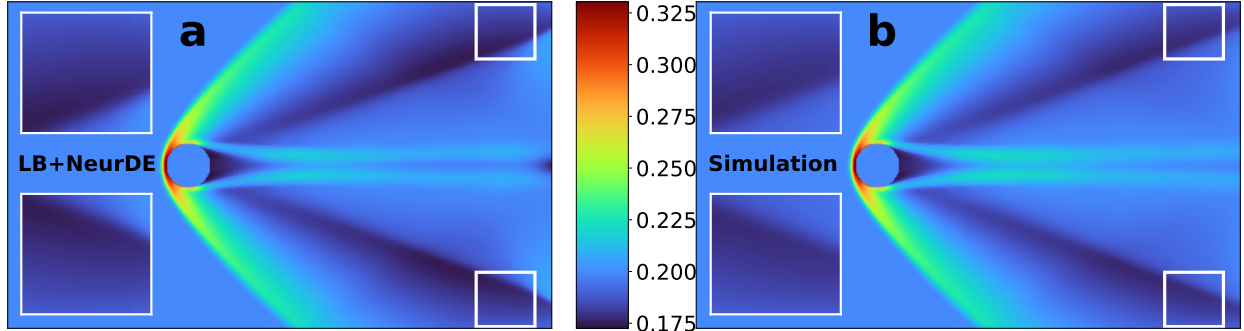


**Figure 22:** The LB+NeurDE *temperature* prediction at  $t = 700$  for the 2D supersonic flow experiment when trained on the first 500 time-steps and initialized at  $t_0 = 500$ .

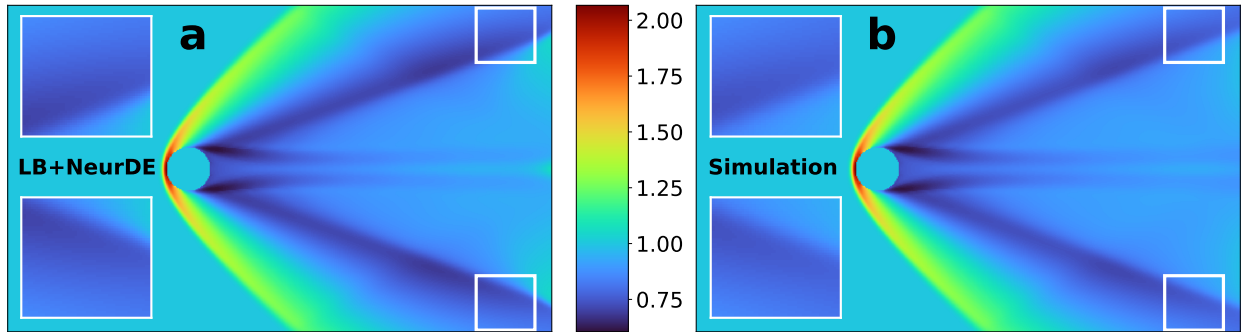


**Figure 23:** The LB+NeurDE *density* prediction at  $t = 700$  for the 2D supersonic flow experiment when trained on the first 500 time-steps and initialized at  $t_0 = 500$ .

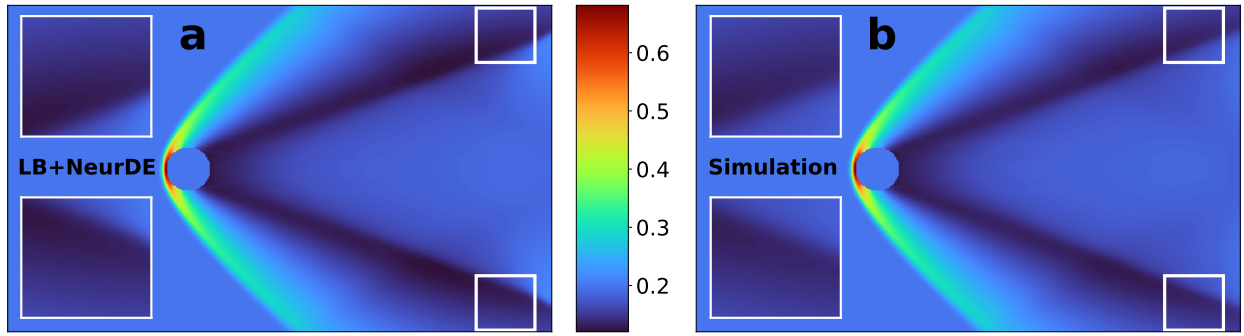


**Figure 24:** The LB+NeurDE *pressure* prediction at  $t = 700$  for the 2D supersonic flow experiment when trained on the first 500 time-steps and initialized at  $t_0 = 500$ .

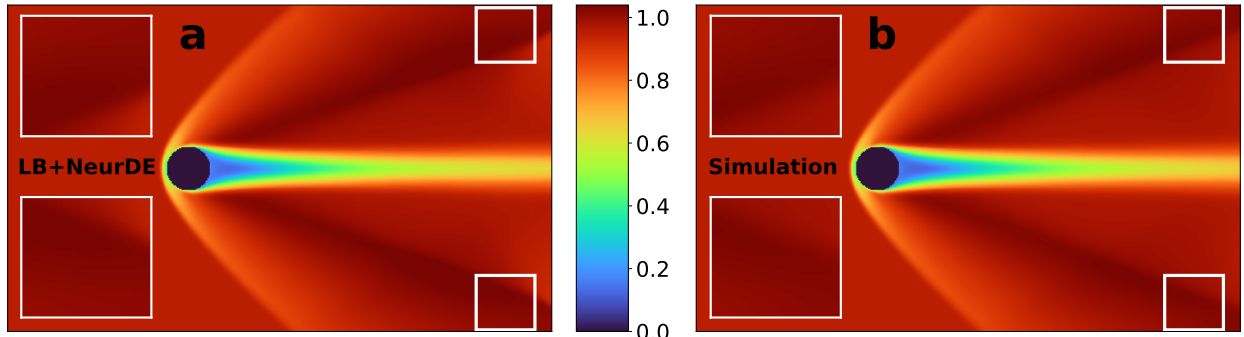


**Figure 25:** The LB+NeurDE *speed* ( $\sqrt{\mathbf{u} \cdot \mathbf{u}}$ ) prediction at  $t = 700$  for the 2D supersonic flow experiment when trained on the first 500 time-steps and initialized at  $t_0 = 500$ .

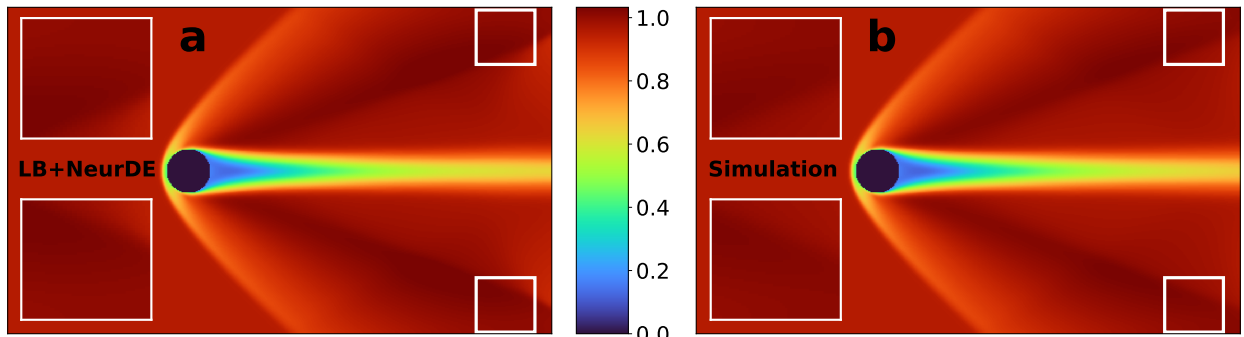


**Figure 26:** The LB+NeurDE *x velocity* ( $\mathbf{u}_x$ ) prediction at  $t = 700$  for the 2D supersonic flow experiment when trained on the first 500 time-steps and initialized at  $t_0 = 500$ .

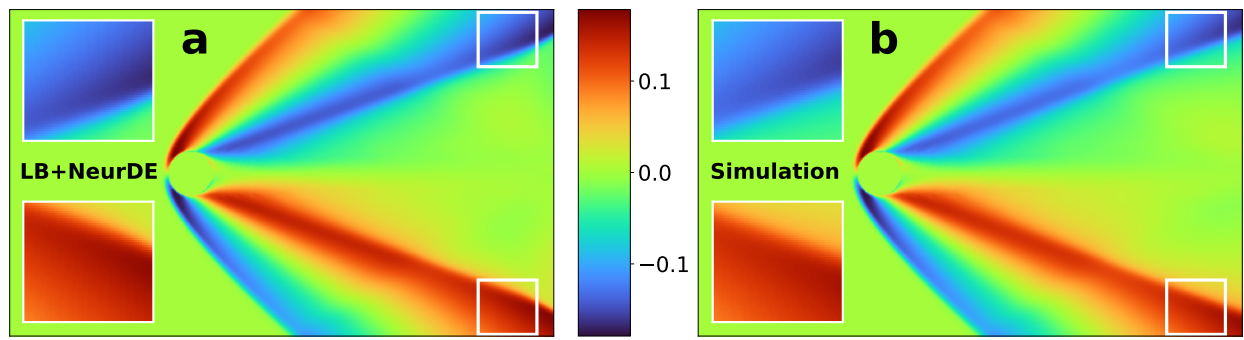


**Figure 27:** The LB+NeurDE  $y$  velocity ( $\mathbf{u}_y$ ) prediction at  $t = 700$  for the 2D supersonic flow experiment when trained on the first 500 time-steps and initialized at  $t_0 = 500$ .

## G.2 Results for Long-Term Predictions

We present further macroscopic results for the 2D cylinder under the same experimental constraints as Subsec. 2.4.2). LB+NeurDE is trained on the first 150 time-steps and then predicts 100 time-steps into the future after being initialized at  $t_0 = 900$ . When comparing the predictions at  $t = 999$ , depicted in Figs. 28 to 33, LB+NeurDE and the reference model exhibit strong agreement in their representations. We observe slight deviations near the right boundary of the outlet as highlighted in the insets.

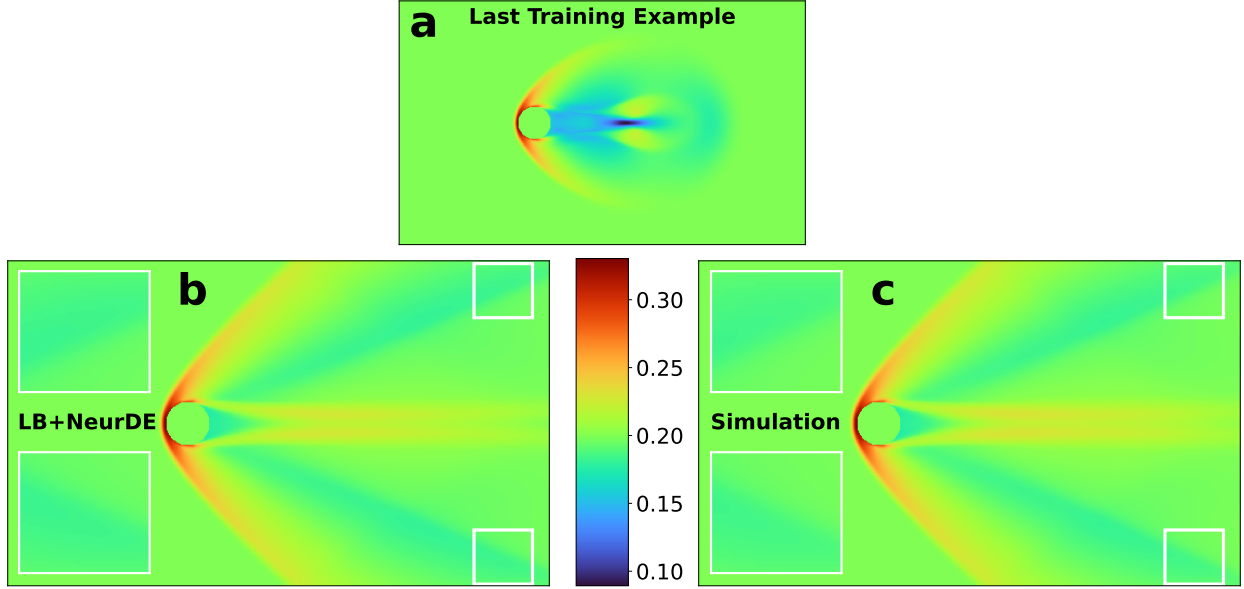


**Figure 28:** We show the LB+NeurDE *temperature* prediction at  $t = 999$  for the 2D supersonic flow experiment when trained on the first 150 time-steps and initialized at  $t_0 = 900$ .

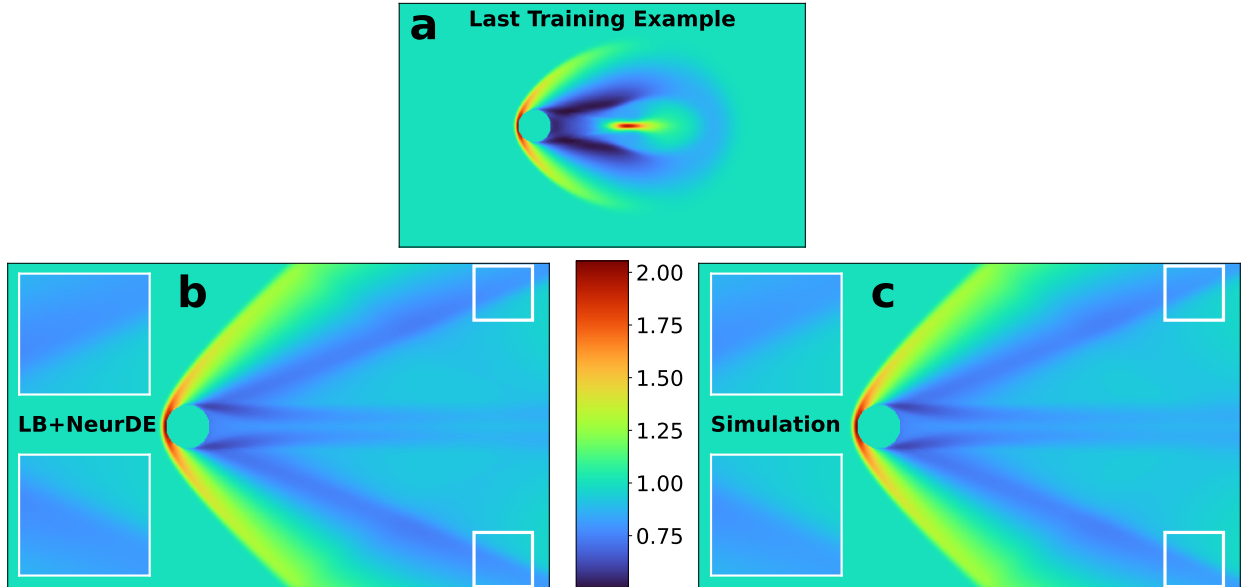


**Figure 29:** We show the LB+NeurDE *density* prediction at  $t = 999$  for the 2D supersonic flow experiment when trained on the first 150 time-steps and initialized at  $t_0 = 900$ .

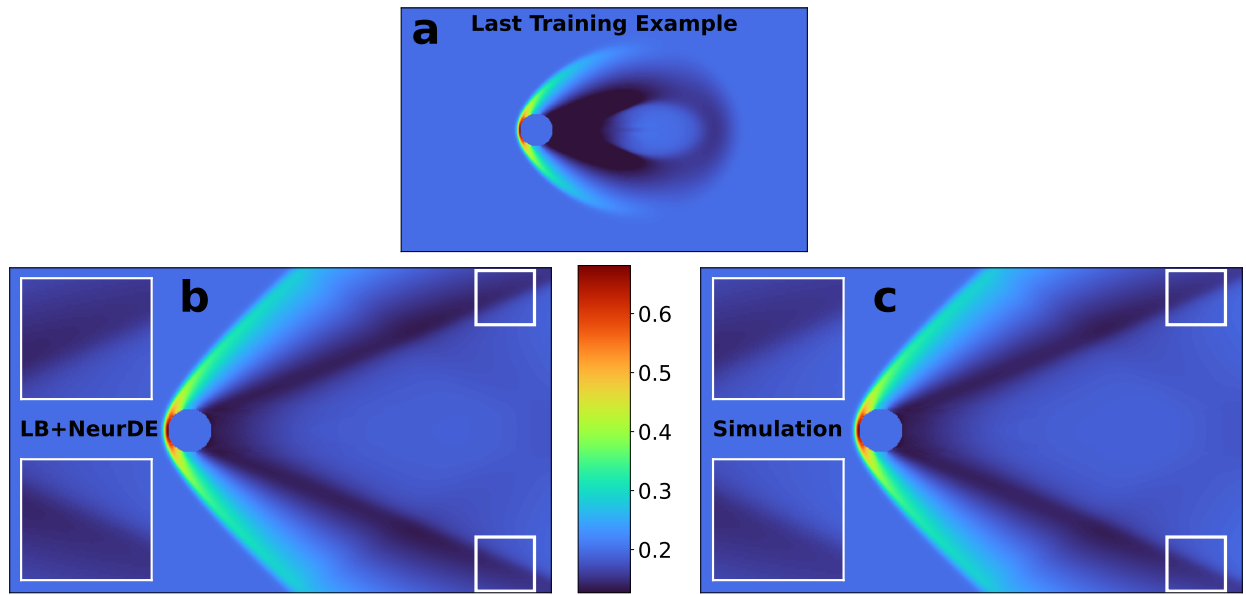


**Figure 30:** We show the LB+NeurDE *pressure* prediction at  $t = 999$  for the 2D supersonic flow experiment when trained on the first 150 time-steps and initialized at  $t_0 = 900$ .

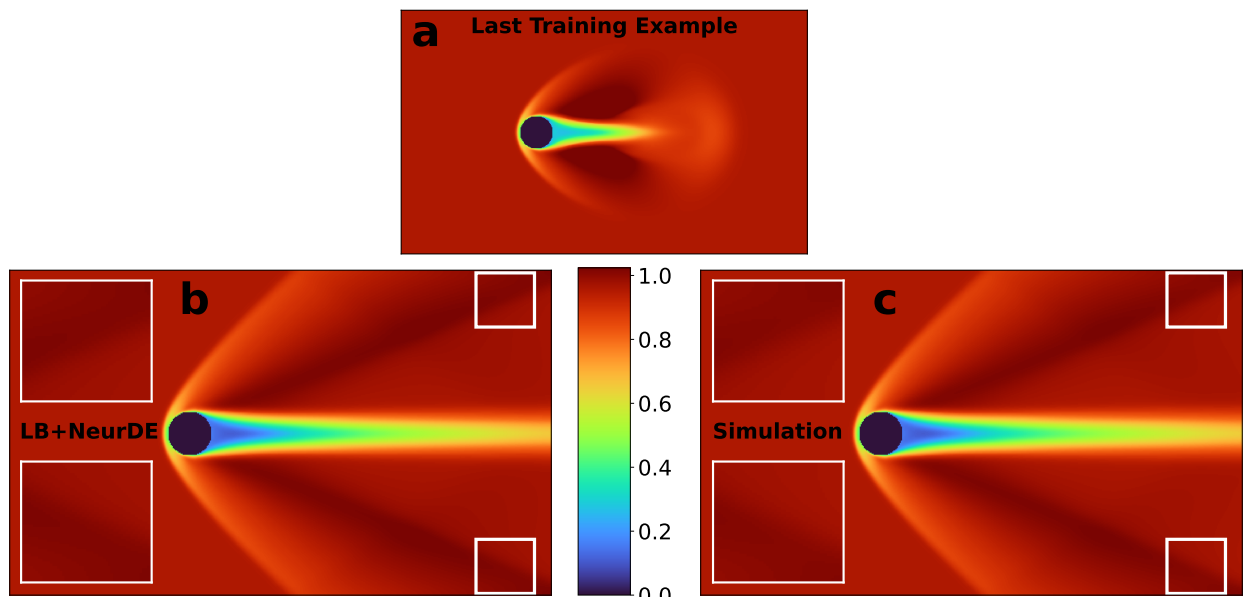


**Figure 31:** We show the LB+NeurDE *speed* prediction at  $t = 999$  for the 2D supersonic flow experiment when trained on the first 150 time-steps and initialized at  $t_0 = 900$ .

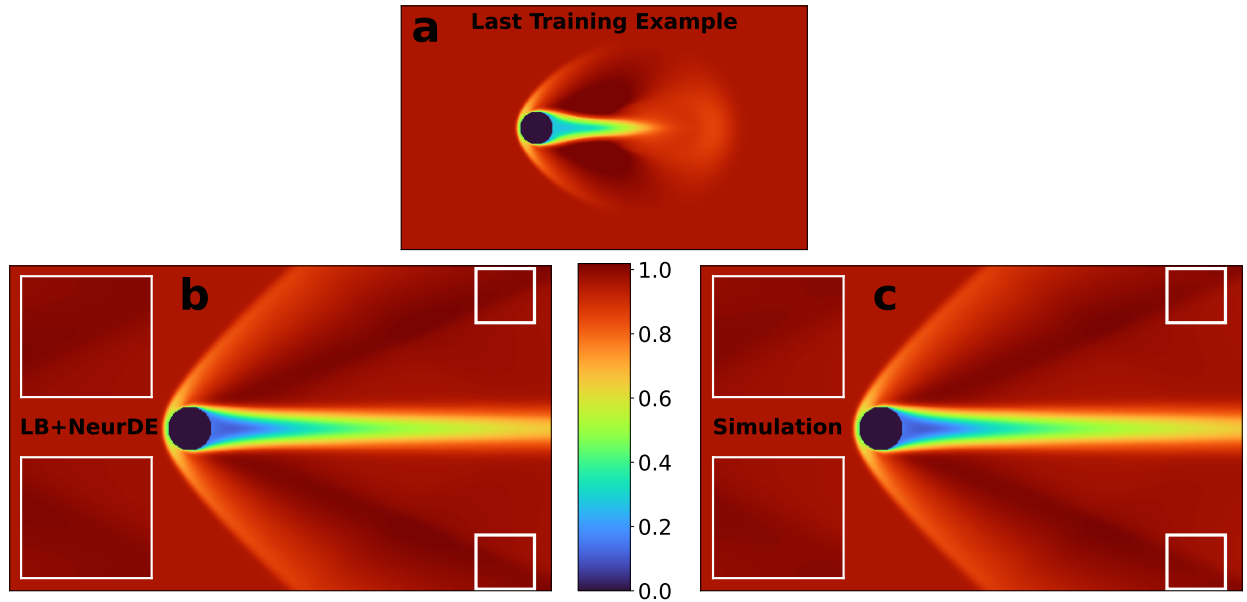


**Figure 32:** We show the LB+NeurDE  $x$  velocity prediction at  $t = 999$  for the 2D supersonic flow experiment when trained on the first 150 time-steps and initialized at  $t_0 = 900$ .

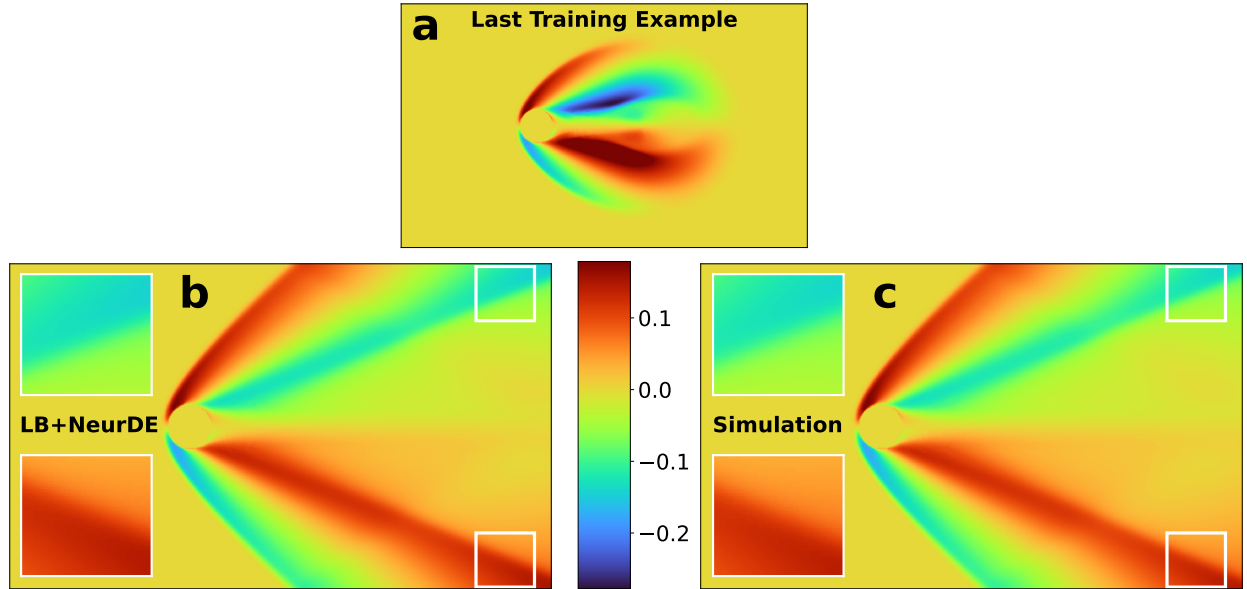


**Figure 33:** We show the LB+NeurDE  $y$  velocity prediction at  $t = 999$  for the 2D supersonic flow experiment when trained on the first 150 time-steps and initialized at  $t_0 = 900$ .